UNIVERSITÀ
DEGLI STUDI
FIRENZE

Dottorato di ricerca in
Fisica e Astronomia

Ciclo XXXIII

Coordinatore: Prof. Raffaello D'Alessandro

Tunneling transport in strongly-interacting atomic Fermi gases

Settore scientifico-disciplinare: Fis/03

Anni Accademici 2017-2020

Dottoranda:
Dott. Giulia Del Pace
Giulia Del Pace

Tutori:
Dr. Giacomo Roati

Prof. Leonardo Fallani
Leonardo Fallani

Coordinatore:
Prof. Raffaello D'Alessandro

Contents

Introduction

Understanding the behavior of strongly-interacting Fermi systems is a central problem in modern physics, that spans from nuclear to astrophysics interest. Whenever interactions are extremely strong, the detailed character of a system's constituents loses relevance and its properties become universal [1]. For this reason, neutron matter in the crust of neutron stars shares important similarities with quarks and gluons in the Early Universe plasma. A theoretical description of strongly-interacting Fermi systems is made difficult by the presence of large correlations, that prevent the standard representation of many-body systems in terms of collective excitations, coined quasiparticles. Given the strong interactions, those systems behaves as nearly perfect quantum fluids, and their hydrodynamic behavior determines both the equilibrium and the transport properties [2]. Moreover, the absence of small parameters in the Hamiltonian, because of the interaction energy being comparable with the Fermi one, prevents perturbative methods to be applied, whereas numerical approaches like Monte Carlo simulations are often frustrated by the fermion sign problem [3], originating from the antisymmetric character of fermionic many-body wavefunctions.

The fundamental quest for the comprehension of those systems can be addressed from a quantum simulation point of view. As originally proposed by Feynman [4], a quantum system under experimental control can be employed to mimic the behavior of another quantum system, surpassing the performances of classical computer simulations [5]. In the last two decades, ultracold atoms and quantum gases have proven to represent versatile and powerful quantum simulators of condensed matter [6–8], high energy physics [9] and even astrophysical phenomena [10, 11]. Atomic systems are indeed clean and controllable: the dimensionality, the potential landscape and the presence of disorder can be adjusted by means of optical potentials, which can be arbitrarily designed with a spatial resolution of the order of the coherence length of the ultracold gas. Moreover, atomic Feshbach resonances allow for tuning the interparticles interactions [12], adding an exceptional degree of control that enables to explore both the weakly and the strongly interacting regimes within the same physical system. Quantum simulation with cold atoms provides a great support to the theoretical and numerical study of many systems, since experiments access regimes intractable for even the most advanced supercomputers and enable to validate theoretical models. Paradigmatic examples are atoms in optical lattices experimentally implementing the microscopic models of Bose- [13] or Fermi-Hubbard [14, 15], or ultracold fermions with tunable interactions realizing the celebrated crossover from a Bose-Einstein condensate

(BEC) to a Bardeen-Cooper-Schrieffer (BCS) state [16]. Furthermore, the high degree of control over quantum gases opens for the exploration of novel states of matter, like quantum droplets in attractive bosonic mixtures [17–19], the supersolid state of dipolar gases [20–22] or of atoms in optical cavities [23], as well as the topological quantum phases of atoms in optical lattices [24].

Ultracold Fermi gases close to a Feshbach resonance are an ideal quantum simulator of strongly-interacting Fermi systems. On top of the resonance indeed, as strong interactions as permitted by quantum mechanics confer to the atomic system thermodynamics the universal behavior shared by neutrons stars and quark-gluon plasma. Moreover, the tunability of the interactions in ultracold fermions offers the possibility to smoothly interpolate from the strongly- to the weakly-interacting regime, so that experimental observations can be validated by comparison with BEC or BCS theory. An emblematic example is given by the precise measurement of the equation of state of the unitary gas performed with ultracold fermions [25], that is now employed to discriminate between theories on interacting Fermi systems. From the first observation of the BEC-BCS crossover, a lot of experimental effort has been dedicated to the characterization of strongly-interacting Fermi gases [16, 26]. Superfluidity and macroscopic phase coherence were demonstrated by the observation of lattices of quantized vortices under rotation [27], whereas radio-frequency spectroscopy provided a direct measurement of the single particle excitation spectrum [28–30]. The field has now become mature to turn to the exploration of quantum transport phenomena in fermionic quantum gases [31]. Transport measurements are indeed a powerful probe, since the way a system reacts to an external perturbation hinges on both its ground state and on the allowed excitations on top of it.

In this thesis, we experimentally investigate the tunneling transport of ultracold Fermi gases of lithium-6 close to a Feshbach resonance. The importance of exploring tunneling transport is twofold. On the one hand, it unveils the coherence properties of the many-body system [32], through the celebrated Josephson effect arising when two condensed reservoirs are connected by a thin repulsive barrier [33]. On the other hand, tunneling transport provides also fundamental information on the role of excitations, via the measurement of the tunneling conductance [34–36], that allows for a direct comparison with ordinary solid state systems. In particular, we implement a current-biased Josephson junction of strongly-interacting Fermi gases by exploiting the high spatial resolution of our apparatus and the dynamic control over repulsive optical potentials provided by a spatial light modulator. Our characterization of the junction throughout the BEC-BCS crossover and across the superfluid transition provides an unambiguous method for quantitatively probing condensed states.

This thesis is organized as it follows:

- In Chapter 1 we provide an introduction to the theoretical framework regarding strongly-interacting Fermi gases and their transport features. After a short overview of low energy scattering and Feshabach resonances, we discuss the BEC-BCS crossover and the variuos superfluid regimes. We focus on both the ground state properties, namely the existence of an order parameter, and the excitations admitted on top of it, fundamental to address transport in strongly-interacting Fermi gases. In the second part of the chapter, we briefly review the state-of-the-art techniques to inquire dynamical properties of atomic samples, paying particular attention to two-terminal transport measurements, which provide a simple device approach to extract the conduction properties of atomic systems. Finally, we discuss the Josephson effect both from a superconducting and an atomic point of view, underlining similarities and differences between the two systems, and providing a microscopic description of the tunneling process.

- Chapter 2 describes our experimental setup, focusing on the technical upgrades performed during this thesis work. Aside from the realization of a novel radio-frequency (RF) source, a new high-resolution microscope objective and a Digital Micromirror Device (DMD) have been implemented in the existing setup, fundamental to image the atomic cloud and imprint dynamical repulsive optical potentials with a sub-micron spatial resolution. We report on the characterization of the two, together with their implementation in the experimental apparatus, that allows for the creation of a current-biased Josephson junction.

- Chapter 3 is devoted to the discussion on one of the main results of this thesis work: the measurement of dc supercurrents in a tunnel junction between strongly-interacting Fermi gases, that led to the extraction of the superfluid order parameter. We produce a current-biased Josephson junction by shining a DMD-generated thin optical barrier on the cloud and we successively inject an external current by translating the repulsive barrier with constant and tunable velocity. We acquire the complete current-voltage characteristic of the junction, and observe clear evidence of the dc Josephson effect up to a critical current. We measure for the first time in fermionic systems a sinusoidal current-phase relarion, unambiguously demonstrating fermionic superfluids to access the dc Josephson regime. We then characterize the critical current versus the barrier properties and map its behavior throughout the BEC-BCS crossover. From the comparison of our results with an analytic model, we extract the condensed fraction of strongly-interacting Fermi gases, providing the first direct measurement of the order parameter in the BEC-BCS crossover.

- In Chapter 4 we report on the experimental investigation of tunneling transport of strongly-interacting Fermi gases across the superfluid transition. By increasing the temperature of the current-biased Josephson junction, we observe the current-voltage characteristic to turn from highly non-linear to Ohmic, which we ascribe to the critical breakdown of dc Josephson supercurrents induced by the pair condensate depletion. Moreover, we reveal a large anomalous contribution to resistive currents, fostered by the coupling between the condensate and phononic Bogoliubov-Anderson excitations. Such anomalous conductance is dominant at low temperature and progressively decreases for increasing temperature, but the measured conductance remains always much larger than the that of an ideal Fermi gas even above critical. Finally, we investigate the nature of transport mediators across the superfluid transition by characterizing the conductance scaling with the barrier properties, observing it to be compatible with the presence of single particle carriers around the critical temperature.

- In Chapter 5 we present the realization of quasi-homogeneous oblate Fermi gases and our recent work on vortex shedding in such systems. We employ the dynamical control over optical potentials offered by the DMD to implement a shedding protocol and exploit the high resolution of our imaging system to detect vortices, both in the BEC regime and in the strongly-interacting one. Our work offers a preliminary step towards the investigation of superfluid turbulence in the BEC-BCS crossover.

Chapter 1

Transport measurements with strongly-interacting Fermi gases

In this chapter we provide an overview of the theoretical concepts related to strongly-interacting Fermi gases and of the strategies employed so far to investigate their nature. When cooled down to degeneracy, strongly-interacting Fermi gases show a superfluid behavior. As well as for their bosonic counterpart, superfluidity manifests in fermionic system thanks to interactions, that in ultracold atoms can be tuned at will thanks to Feshbach resonance. In particular, fermionic gases explores the celebrated BEC-BCS crossover, spanning from a Bose-Einstein condensate (BEC) of tightly bound molecules, when interactions are low and repulsive, to a Bardeen-Cooper-Schrieffer (BCS) gas of Cooper pairs for weakly attractive interactions. These systems are particularly challenging to model theoretically, because of the strong interactions that characterize them, and the experimental investigation supplies thus a valuable support on their understanding. In the last decade, transport measurements have proven to be a powerful tool to disclose the inner nature of a material and their application on strongly-interacting Fermi gases provide a complete characterization of their properties. In fact, by monitoring the response of the system under an external perturbation, both its ground state and the relevant excitations on top of it can be addressed.

This chapter is organized as follows. In Sec. 1.1 we discuss the main properties of a non-interacting ideal Fermi gas, that sets a reference for comparison with the interacting regime presented in Sec. 1.2. In particular, we introduce the low energy scattering process that characterize interactions among ultracold atoms, to then present the Feshbach resonance that allow for the exploration of the BEC-BCS crossover. The various regimes at different interaction strength are discussed, with particular attention to the unitary one in correspondence of the resonance. Crossover gases are successively characterized by discussing the coherence properties of their ground state, namely their order parameter, and the admitted excitations on top of it in the different regimes. In Sec. 1.3, an overview of transport measurements with cold atoms is presented, to then focus our attention on the tunnelling properties of strongly-interacting Fermi gases in Sec. 1.4. Here, we discuss the Josephson effect both from a superconducting and an atomic point of view, highlighting similarities and differences of the two cases.

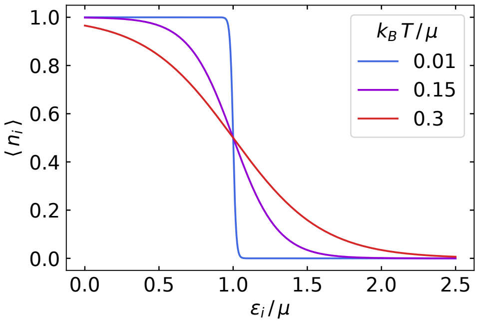

Figure 1.1: Average occupancy of states of energy ϵ_i for different temperature of the ensamble.

Finally, the microscopic description of the Josephson effect is addressed, providing the fundamental connection between the phenomenon and condensation.

1.1 Ideal Fermi gas

The distinctive properties of fermions, namely half-integer spin particles, is Pauli exclusion principle, which prevents a quantum state to be occupied by two identical particles. Such rule does not apply to bosons with integer spin, that on the other hand can condense into the same quantum state, in the celebrated phenomenon of Bose-Einstein condensation [37]. Considering a grand-canonical ensambles of fermions in contact with a reservoir, with which it can exchange particles and energy, the average occupation of state i of energy ϵ_i is given by:

$$\langle n_i \rangle = \frac{1}{e^{(\epsilon_i - \mu)/k_B T} + 1} \tag{1.1}$$

where μ is the chemical potential of the ensamble and T its temperature. As shown in Fig. 1.1, at zero temperature all energy levels are occupied up to μ, which defines the Fermi energy ϵ_F of the system. By increasing the temperature, higher energy levels start to be thermally occupied, and $\langle n_i \rangle$ shows a smoother trend around μ.

The grand-canonical description is not strictly valid for atomic gases, that are trapped to keep them isolated from the surrounding and are characterized by a fixed number of particles N and total energy E_{tot}. For the grand canonical description to hold, the chemical potential of the sample has to be chosen to give $N = \sum_i \langle n_i \rangle$. In particular, let's consider a non-interacting fermionic sample of particles of mass m confined in the harmonic potential:

$$V_h(\mathbf{r}) = \frac{1}{2} m \left(\omega_x^2 x^2 + \omega_y^2 y^2 + \omega_z^2 z^2 \right) , \tag{1.2}$$

where $\omega_{x,y,z}$ are the trap frequencies in the three spatial directions. Under the Thomas-Fermi approximation of $\beta = 1/k_B T \gg \hbar\omega_{x,y,z}$, i.e. the thermal energy is much larger than the harmonic oscillator level spacing, the occupation of the phase space cell $\{\mathbf{r}, \mathbf{p}\}$ is given by:

$$f(\mathbf{r}, \mathbf{p}) = \frac{1}{e^{\beta\left(\frac{\mathbf{p}^2}{2m}+V_h(\mathbf{r})-\mu\right)}+1}. \tag{1.3}$$

The density distribution of the ideal Fermi gas can be calculated by integrating the previous relation over the momentum space:

$$n(\mathbf{r}) = \int \frac{d^3\mathbf{p}}{(2\pi)^3}\, f(\mathbf{r}, \mathbf{p}) = -\frac{1}{\lambda_{dB}^3}\,\mathrm{Li}_{3/2}\left(e^{\beta(\mu - V_h(\mathbf{r}))}\right), \tag{1.4}$$

where $\lambda_{dB} = \sqrt{\frac{2\pi\hbar^2}{mk_BT}}$ is the thermal de Broglie wavelength and $\mathrm{Li}_n(z)$ is the polylogarithm function of order n [16].

At zero temperature, the density distribution has a polynomial expression proportional to $(1 - x_i^2/R_i^2)^{3/2}$, that vanishes at a distance $R_i = \sqrt{\frac{2E_F}{m\omega_i^2}}$, called the Thomas-Fermi radius along the i-th direction. Here, E_F is the trap-averaged Fermi energy, defined as the highest occupied state of the non-interacting trapped Fermi gas. The value of E_F is fixed by the total number of atoms N populating the lowest energy levels of the trap [16]:

$$N = \int d^3\mathbf{r}\; n(\mathbf{r}, T = 0) = \frac{1}{6}\left(\frac{E_F}{\hbar\overline{\omega}}\right)^3, \tag{1.5}$$

where $\overline{\omega} = (\omega_x\, \omega_y\, \omega_z)^{1/3}$ is the average trap frequency. The trap-average Fermi energy is thus given by:

$$E_F = \hbar\overline{\omega}(6N)^{1/3}. \tag{1.6}$$

Under local density approximation (LDA), we can define a local Fermi energy $\epsilon_F(\mathbf{r})$ as well. In fact, if the trapping potential slowly varies, we can individuate inside the trap a set of volumes small enough for $V_h(\mathbf{r})$ to be constant, but big enough for all thermodynamic quantities to be well-defined inside each of them. Under such assumption, the inhomogeneous system is approximated as the sum of locally homogeneous systems, where a local chemical potential can be defined as $\mu(\mathbf{r}) = \mu - V_h(\mathbf{r})$. In each local volume, the Fermi energy is defined as [16]:

$$\epsilon_F(\mathbf{r}) = \mu(\mathbf{r}, T = 0) = \frac{\hbar^2}{2m}(6\pi^2 n(\mathbf{r}))^{2/3}, \tag{1.7}$$

which is related to the trap averaged one by the relation $\epsilon_F(\mathbf{r}) = E_F - V_h(\mathbf{r})$.

At high temperature, the classical limit of Gaussian Maxwell-Boltzman distribution is recovered:

$$n_{cl}(\mathbf{r}) = \frac{N}{\pi^{3/2}\sigma_x\sigma_y\sigma_z} e^{-\sum_i x_i^2/\sigma_i^2}, \tag{1.8}$$

where $\sigma_i^2 = \frac{2k_BT}{m\omega_i^2}$. In particular, the quantum regime is accessed when the de Broglie wavelength approaches the interparticle spacing, namely $\lambda_{dB} \approx n^{1/3}$, that for a non-interacting Fermi gas happens for $T \approx T_F$, where $T_F = E_F/k_B$ is the Fermi temperature.

For finite $T < T_F$, the density distribution of the gas depends on the local level of degeneracy, given by the ratio between $k_B T$ and the local Fermi energy $\epsilon_F(\mathbf{r})$. On the wings of the cloud where the density is low, $k_B T \gg \epsilon_F(\mathbf{r})$ and the gas shows a classical density distribution. On the trap center instead, $k_B T \ll \epsilon_F(\mathbf{r})$ so that the density distribution is the zero temperature one, smoothly interpolated to the classical one by the polylogarithm function in Eq. (1.4). Therefore, the thermometry of a very cold cloud is a hard task, as temperature only affects the wings of the cloud and has to be extracted from their shape.

1.2 Interacting Fermi gases

Introducing interactions in a fermionic atomic system enhances its complexity, but at the same time opens to the study of the rich physics of fermionic superfluidity, that, similarly to Bose case, manifests only in interacting systems. One of the most powerful feature of atomic gases is the possibility to tune the interactions thanks to the so-called phenomenon of Feshbach resonance. By acting on an external magnetic field, both the strength and the sign of interactions can be varied, opening the way for the exploration of the celebrated BEC-BCS crossover with ultracold fermions. In particular, across a Feshbach resonance, different kinds of fermionic superfluid can be accessed, spanning from a Bardeen-Cooper-Schrieffer gas of Cooper pairs to a Bose-Einstein condensate of tightly bound molecules, passing the most strongly interacting, universal unitary limit. In the following we present the basics of scattering theory, focusing on the specific case of low energy collisions that characterize interactions among cold atoms. Successively, the Feshabach resonances are introduced, and its major application on cold atoms fermionic system, the BEC-BCS crossover, is discussed. The different superfluidity regimes in the crossover are illustrated, focusing the attention on the unitary Fermi gas, where interactions are the strongest in nature. Finally, we discuss the properties of fermionic superfluids ground state, characterized by a macroscopic order parameter, and their elementary excitations, both fundamental to understand the transport properties of such quantum materials.

1.2.1 Low energy scattering

Since cold atoms are dilute and neutral systems, they interacts only via the attractive van der Waals potential $V(\mathbf{r}) \propto -\frac{1}{r^6}$, originating from dipole-dipole interactions. Typically, atomic interactions are represented by the Lennard-Jones potential, which adds to the van der Waals term a short-range one to include the Coulomb repulsion of electronic clouds:

$$V(r) = -\frac{C_6}{r^6} + \frac{C_{12}}{r^{12}}, \tag{1.9}$$

where C_6 and C_{12} are numerical coefficients. In highly dilute systems as cold atom clouds, the interparticle spacing $n^{-1/3}$ is much larger than the range r_0 of the above potential, and in particular for ^{6}Li, $r_0 \simeq 50\,a_0$ while $n^{-1/3} \simeq 20000\,a_0$. Interactions among cold atoms are thus dominated by two-body collisions in which the detailed character of the potential can be usually neglected.

The scattering problem of two particle interacting via a central potential $V(\mathbf{r})$ can be solved in the center of mass frame, where the incoming wavefunction is a plane wave of wave vector $\mathbf{k}$. Away from the collision region, the scattered wavefunction can be written as the superposition of the incoming and the scattered wave [38]:

$$\psi_{as} \propto e^{ikr} + f(\mathbf{k}, \mathbf{k}') \frac{e^{ikr}}{r}, \tag{1.10}$$

where the scattered one is given by a spherical wave multiplied by the scattering amplitude $f(\mathbf{k}, \mathbf{k}')$. The latter gives the probability amplitude that the wave is scattered in the direction $\mathbf{r} = \mathbf{k}'/k$, where $k' = k$ because of energy conservation, and it is related to the cross-section by the relation $\frac{d\sigma}{d\Omega} = |f(\mathbf{k}, \mathbf{k}')|^2$, where Ω is the solid angle. The central Lennard-Jones scattering potential allows for a partial wave expansion of the asymptotic solution:

$$\psi_{as} = \sum_l Y_l^0(\theta) \frac{u_l(r)}{r}, \tag{1.11}$$

where Y_l^0 are the spherical harmonics with $m = 0$ and $u_l(r)$ is the radial wavefunction. By employing such expansion in the Schrodinger equation, we get:

$$\frac{\hbar^2}{2m} \left(\partial_r + k^2 \right) u_l(r) = V_e(r) u_l(r) \tag{1.12}$$

where $V_e(r) = V(r) + \frac{\hbar^2 l(l+1)}{2mr^2}$ is the effective potential. At low temperature, the centrifugal barrier $\frac{\hbar^2 l(l+1)}{2mr^2}$ inhibits collisions with $l > 0$, and only the s-wave scattering at $l = 0$ is permitted. However, when the collision involves two identical fermions, the wavefunction to describe them should be antisymmetric, which limits the partial wave expansion to only odd values of l. As a consequence, cold identical fermions do not interact with each other, as the s-wave scattering is suppressed for them. To evaporatively cool fermionic samples, two different hyperfine states have to be employed, so that collisions between fermions in opposite spin state can cause thermalization of the sample. Therefore, from now on, we will consider the scattering process to happen between fermions in different spin state, which is not suppressed by statistic.

By restricting our attention to s-wave scattering only, the asymptotic solution of Eq. (1.12) can be written as:

$$u_0(r) \simeq \sin(kr - \delta_0(k)), \tag{1.13}$$

where $\delta_0(k)$ is the phase shift imprinted on the scattered wavefunction by the collision. In the same low-energy limit the scattering amplitude assumes the form:

$$f(k) \simeq \frac{1}{\frac{1}{a} - r_e \frac{k^2}{2} + ik}, \tag{1.14}$$

where we have introduced the effective range $r_e \sim r_0$, that depends on the details of the potential, and the scattering length a defined as:

$$a = - \lim_{k \to 0} \frac{\tan \delta_0(k)}{k}. \tag{1.15}$$

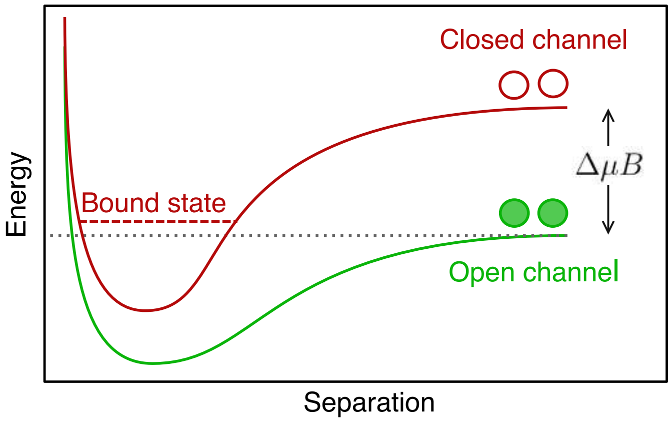

Figure 1.2: Sketch of open and closed channels in the scattering process near a Feshbach resonance. The scattering length between particles in the open (triplet) channel is affected by the presence of a bound state in the closed (singlet) one, because of hyperfine coupling between the two. The energy shift $\Delta\mu\, B$ between the two channels can be tuned by acting on the magnetic field.

In cold atom systems, the scattering length is typically orders of magnitude larger than the Lennard-Jones potential range r_0, allowing for the approximation of interatomic interactions with a contact potential of effective range $r_e = 0$. The scattering process is therefore fully described by the scattering length a and the interaction potential can be approximated with a delta-like pseudopotential:

$$V_p(r) = \frac{4\pi\hbar}{m}\, a\, \delta(r), \tag{1.16}$$

which is attractive for $a < 0$ and repulsive for $a > 0$. As it will be discussed in detail in the next paragraph, Feshbach resonances allow for tuning the scattering length both in sign and in strength up to the limit case of $a \to \infty$. For diverging scattering length, the interactions are the highest allowed in nature, but we remark that none of the scattering process observables actually diverges. In fact, the cross section for s-wave scattering with $r_e = 0$ takes the form $\sigma = \frac{4\pi a^2}{1+k^2a^2}$, which remains finite even for $a \to \infty$.

1.2.2 Feshbach resonances

The value and sign of the scattering length depends on the particular interaction potential, but for atomic systems it can be tuned by means of Feshbach resonances, that will be briefly described in the following. For a more comprehensive discussion of the phenomenon we refer to the review in Ref. [12].

The interaction potential of two alkali atoms depends on their electron spin configuration, identifying a triplet and a singlet potential, as illustrated in Fig. 1.2. The state of the incoming particles defines which one of the two is the open channel, that is populated before the scattering event. Because of hyperfine coupling between the two potentials, the presence of a bound state in the closed channel modifies the scattering properties of particles in the open one. In fact, a bound state in the interaction

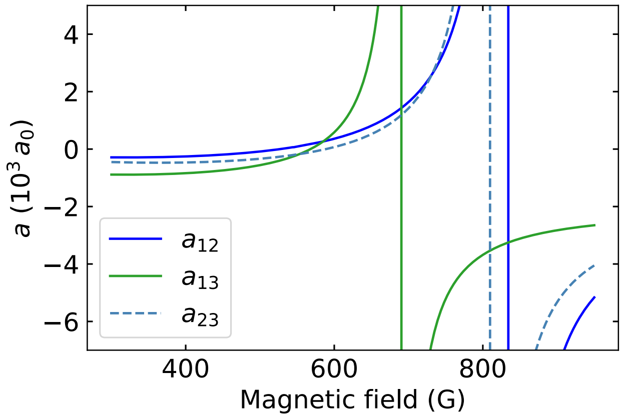

Figure 1.3: Feshbach resonances of the three lowest ^{6}Li hyperfine states: the scattering length for collision between two of them depends on the external magnetic field. Data are taken from Ref. [40].

potential causes a divergence in the scattering length when its energy is resonant with the one of the scattering particles, as it can be demonstrated for a simple square potential [39]. Furthermore, the energy of the closed channel can be shifted by acting on an external magnetic field: because of the magnetic moment difference $\Delta\mu$ between the triplet and singlet state, a change δB in magnetic field causes a relative energy shift $\Delta\mu\, B$ between the two potentials. When the energy shift is such that the bound state in the closed channel is resonant with the particles energy in the open one, the scattering length diverges, giving rise to a Feshabach resonance. On a phenomenological level, the scattering length close to a resonance can be expressed in terms of the external magnetic field B as:

$$a = a_{bg}\left(1 - \frac{\Delta B}{B - B_0}\right), \tag{1.17}$$

where a_{bg} is off-resonance background scattering length, ΔB is the resonance width and B_0 its center.

The Feshbach resonances of the three lowest hyperfine states of ^{6}Li, referred as $|1\rangle$, $|2\rangle$ and $|3\rangle$, are presented in Fig. 1.3. Both resonances between $|1\rangle - |2\rangle$ and $|1\rangle - |3\rangle$ states are about 250 G broad, enough to ensure a mild influence of magnetic field fluctuations on the scattering length. In particular, $|1\rangle - |2\rangle$ Feshabach resonance is centered around $B_0 = 832$ G and it is the one we employ for the production of strongly-interacting fermionic superfluids in the BEC-BCS crossover.

1.2.3 The BEC-BCS crossover

Thanks to Feshbach resonances, ultracold fermions provide a unique platform for the exploration of the BEC-BCS crossover. On the one hand, the Bardeen-Cooper-Schrieffer (BCS) theory provides the celebrated understanding of superconductivity as

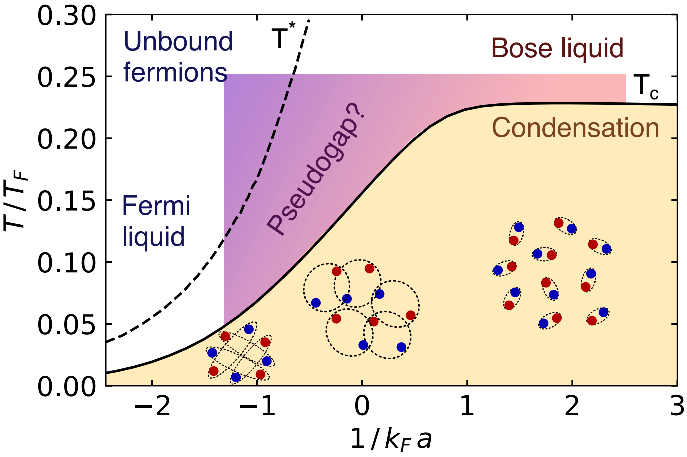

Figure 1.4: Phase diagram for the BEC-BCS crossover of an homogeneous fermionic gas. Below the pairing temperature T^* fermions in opposite spin states, represented as blue and red circles, form a couple, the size of which depends on interactions, parameterized as $1/k_F a$ where $k_F = \sqrt{2mE_F}/\hbar$ is the Fermi momentum. When moving from the BEC ($1/k_F a > 1$) to the BCS ($1/k_F a < -1$) side of the resonance, tightly bound molecules turns into large Cooper pairs, passing through the unitary regime of $1/k_F a = 0$ where the pair size is comparable to the interparticle distance. When the temperature is lowered below the critical one T_c, fermionic pairs undergo to condensation, giving rise to different fermionic superfluids for various interactions. The intermediate region of $T_c < T < T^*$, where pairs are already formed but not yet condensed, is called pseudogap in analogy with high-T_c superconductors, but is unclear whether this phase is accessible for strongly-interacting fermionic superfluids as well. The curves of T^*/T_F and T_c/T_F are extracted from Ref. [16] and Ref. [41], respectively.

the consequence of Cooper pairing in a Fermi gas, where weak attraction among electrons causes them to pair and condense in a macroscopic wave function. On the other hand, a Bose-Einstein condensate (BEC) is the macroscopic occupation of the lowest energy state by bosons, that exhibit a superfluid behaviour when weakly interacting between each other. Despite the differences in constituents, the BCS and BEC regimes have been theoretically proven to be smoothly connected between each other, since their ground state wavefunctions are formally equivalent [42–44]. Ultracold fermions allow for the experimental realization of the BEC-BCS crossover theory model, as interactions can be freely tuned from weakly repulsive to attractive thanks to Feshbach resonances. Furthermore, ultracold fermionic gases access the resonantly interacting regime as well, where interactions are the highest available in nature. In particular, they explore the phase diagram of Fig. 1.4, where the interaction strength is parametrized in terms of $1/k_F a$, where $k_F = \sqrt{2mE_F}/\hbar$. At sufficiently low temperature, namely for $T < T^*$, atoms in opposite spin states, represented as red and blue circles in the figure, couples together to form a pair, that has different size and nature across the resonance. In the BEC regime of weakly repulsive interactions, for $1/k_F a \gg 1$, tightly bound molecules proliferate below T^*, which turn into large Cooper pairs as the resonance is crosses towards the weakly attractive BCS regime of $1/k_F a \ll -1$. For even lower temperature, the critical temperature for condensation T_c is eventually crossed: the gas of paired fermions forms a BEC of tightly bound molecules for $1/k_F a \gg 1$ and a BCS gas of Cooper pairs for $1/k_F a \ll -1$. At the center of the resonance, for $1/k_F a = 0$, pairs have dimension comparable with the interparticle spacing, forming thus a strongly-correlated many-body system similar to that of electrons in high-T_c superconductors. In the region between T_c and T^*, paired fermions are already present in the gas, but not yet condensed. On the BEC side of the crossover, molecules remain bound even well above T_c, while in the BCS regime condensation occurs at the same time as pairing. It is under debate whether a phase of preformed pairs is present in the unitary regime [45], defining the pseudogap region of the phase diagram in analogy with high-T_c superconductors. In the following, we discuss the three limit cases of BEC, BCS and unitary gas, referring to gases below T_c as fermionic superfluids, since they show a superfluid behavior, as it will be discussed in Sec. 1.2.6.

BEC limit When interactions are weak and repulsive ($1/k_F a \gg 1$), tightly bound molecules form below T^*, the binding energy of which depends on the scattering length as $E_b = -\frac{\hbar^2}{ma^2}$. Molecules are stable as long as they are much larger than the range of the van der Waals potential, namely for $a \gg r_0$, when the pair wave functions have negligible overlap with the deeply bound states. However, when reducing the scattering length, we observe losses due to relaxation of molecules into the deeply bound state to become more and more relevant, progressively reducing the lifetime of the BEC as $1/k_F a$ is increased. Therefore, the produced molecular BECs in our experimental setup are never deeply in the weakly interacting regime.

The pair chemical potential in the BEC limit can be retrieved from the weakly interacting BEC theory, considering that a molecular BEC is formed by pairs of mass $m_B = 2\,m$ that interact with a scattering length $a_B = 0.6\,a$ [46]. Therefore, under the Thomas-Fermi approximation, the pair chemical potential is given by [16]:

$$\mu_B = \frac{\hbar\overline{\omega}}{2}\left(\frac{15\,N_B\,a_B}{a_h}\right)^{2/5} \tag{1.18}$$

where N_B the number of pairs and $a_h = \sqrt{\hbar/m_B\overline{\omega}}$ is the harmonic oscillator characteristic length.

BCS limit The BCS regime of $1/k_F a \ll -1$ is characterized by weak attractive interactions, that below T_c cause the formation of a BCS superfluid. In this regime, only a small fraction of particles around the Fermi sphere with momentum $k \sim k_F = \sqrt{2mE_F}/\hbar$ is involved in the pairing, so that the chemical potential of the gas is of the order of the Fermi energy [16]:

$$\mu \simeq E_F, \tag{1.19}$$

where μ indicates the single fermion chemical potential. When the gas undergoes to Cooper instability, i.e. proliferation of Cooper pairs, an energy gap Δ appears in the excitation spectrum of the Fermi sea, which scales exponentially with decreasing interactions:

$$\Delta = \frac{8}{e^2} E_F \exp\left(\frac{\pi}{2k_F a}\right). \tag{1.20}$$

A similar trend is exhibited by the critical temperature for condensation as well, that for an homogeneous gas is given by [2]:

$$T_c/T_F = 0.28 \exp\left(\frac{\pi}{2k_F a}\right). \tag{1.21}$$

We note that, being the lowest experimentally reachable temperatures of the order of $T/T_F \sim 0.1$, it is practically impossible to prepare a weakly interacting BCS superfluid of $1/k_F a \ll -1$. The BCS gases we refer to in this thesis are always in the strongly interacting regime, with $1/k_F a \sim -1$.

1.2.4 The Unitary Fermi gas

When the scattering length diverges at the center of a Feshbach resonance, the unitary limit is reached. Here, interactions are the highest possible and pairs formed below T^* have a size comparable with the interparticle distance, making the unitary Fermi gas (UFG) similar to high-T_c superconductors. This regime of large scattering length is reached in nature also in neutron stars and quark-gluon plasma [47], the densities of which are however much higher than those of ultracold atomic gases. The UFG realizes thus the unique condition of a strongly-interacting dilute system, being a powerful playground to study universal physics that span from nuclear to astrophysics interest. In fact, as far as $a \to \infty$, the only remaining length scale in a UFG is the interparticle distance $n^{-1/3} \propto 1/k_F$, and E_F the only relevant energy scale. Therefore, the UFG properties do not depend on the nature of its constituents, and the unitary atomic gas shares a universal behavior with those composed by neutrons or quarks. As a result, the UFG is a scale-invariant system described by a universal equation of state depending only on the dimensionless parameter $q = \beta\mu = \mu/k_B T$ [48]. All the UFG thermodynamic properties can be thus derived from those of a non-interacting Fermi gas, once rescaled by a dimensionless quantity ξ, the so-called Bertsch parameter. In general, ξ is a function of temperature and spin polarization, and for a spin-balanced gas at zero-temperature has been measured to be $\xi = 0.37$ [25]. In particular, since the only relevant energy scale is E_F, the chemical potential of a homogeneous UFG is simply $\mu = \xi\, E_F$, while for the harmonically trapped samples used in this thesis $\mu = \sqrt{\xi}\, E_F$ [16].

The equation of state (EoS) of the unitary Fermi gas has been widely investigated both theoretically and experimentally, and in the last decade many parameter regimes have been measured [25, 49–51]. Here, we focus on the density EoS at finite temperature, that can be written as:

$$n = \frac{1}{\lambda_{dB}^3} f_n(q), \tag{1.22}$$

where $\lambda_{dB} = \sqrt{\frac{2\pi\hbar^2}{m k_B T}}$ is the the de Broglie wavelength and f_n is a universal function of

Table 1.1: Virial expansion coefficients b_s up to the 4-th order.

	Value	Source
b_1	1	Ref. [55] (theo.)
b_2	$\frac{3\sqrt{2}}{8}$	Ref. [55] (theo.)
b_3	-0.29095295	Ref. [55] (theo.)
b_4	$0.065(10)$	Ref. [25] (exp.)

$q = \beta\mu$. Considering the universality of the UFG, the latter can be decomposed as:

$$f_n(q) = F(q) \times \left(-\mathrm{Li}_{3/2}(-e^q)\right), \tag{1.23}$$

where the second term takes into account the non-interacting equation of state as in Eq. (1.4), while the first has been measured in Ref. [25] in the range $-1.5 < q < 3.9$ as the ratio between UFG and non interacting densities. Although the high degeneracy regime of $q > 3.9$ and the low one of $q < -1.5$ have not been measured, the density EoS can be extended outside of the measured range by employing the phonon model of Ref. [52,53] and the virial expansion of Ref. [54], respectively.

In the low degeneracy regime, where the temperature is high and the chemical potential is negative, the decreasing fugacity e^q for $q < -1.5$ allows for a virial expansion of the grand canonical potential Φ_G. In this limit the density EoS can be expressed as [54]:

$$f_n(q) = \sum_{s=1}^{\infty} b_s\, s\, e^{sq}. \tag{1.24}$$

The virial expansion coefficient b_s are known up to the 4-th order, as listed in Table 1.1.

On the other hand, in the high degeneracy regime of $q > 3.9$, the temperature is well below the superfluid transition and phonon excitations provide the dominant contribution to the excitation spectrum [53]. Here, the thermodynamic behaviour of the superfluid can be deduced by considering the phonon contribution in the free Helmoltz energy and expanding it for low temperatures. This procedure yields:

$$f_n(q) = \frac{4}{3\sqrt{\pi}}\left[\left(\frac{q}{\xi}\right)^{3/2} - \frac{\pi^4}{480}\left(\frac{3}{q}\right)^{5/2}\right], \tag{1.25}$$

where the first term corresponds to the zero temperature density contribution with $\xi = 0.37$, while the second one represents the leading order of thermal excitation of phonons.

To summarize, the full UFG density EoS can be written as the piece-wise function:

$$f_n(q) = \begin{cases} \sum_{s=1}^{4} s\, b_s\, e^{sq} & \text{for } q < -1.5, \\ -\mathrm{Li}_{3/2}(-e^q)\, F(q) & \text{for } -1.5 \le q \le 3.9, \\ \frac{4}{3\sqrt{\pi}}\left[\left(\frac{q}{\xi}\right)^{3/2} - \frac{\pi^4}{480}\left(\frac{3}{q}\right)^{5/2}\right] & \text{for } q > 3.9 \end{cases} \tag{1.26}$$

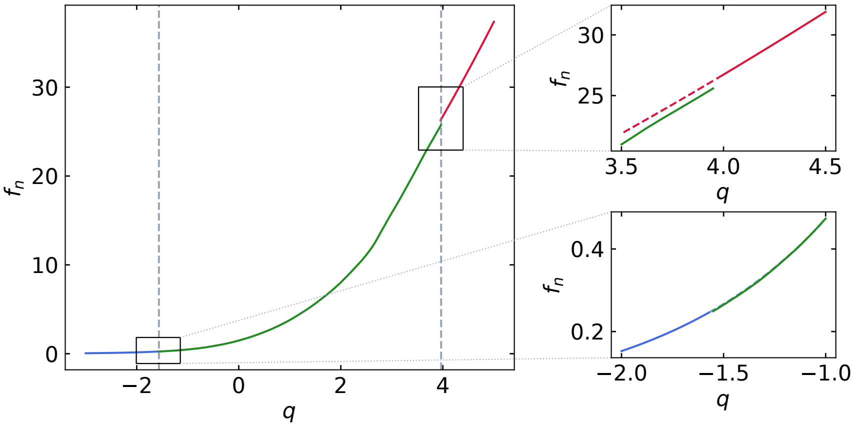

Figure 1.5: Unitary gas density equation of state as defined in Eq. (1.26). The intermediate region of $-1.5 < q < 3.9$ (green line) employes data measured in Ref. [25], the low degeneracy regime of $q < -1.5$ (blue line) is obtained from the virial expansion, whereas the high degeneracy regime of $q > 3.9$ (red line) employs the phonon model. On the right: zoom on the connections at $q = -1.5$ (bottom) and $q = 3.9$ (top) of the piece-wise function. The extension of the phonon model (top) and the virial expansion (bottom) inside the range of measured q is plotted as dashed red and blue line, respectively.

that is plotted in Fig. 1.5. As visible in the zoomed plots, the three regimes connects smoothly between each other.

1.2.5 Order parameter of crossover superfluids

When crossing the critical temperature T_c, fermionic pairs undergo to condensation, which is associated with the development of long-range order (LRO) among the constituents of the system. As first proposed by London [56] and successively formalized by Onsager and Penrose [57], condensation properties of a bosonic system can be extracted from the one-particle density matrix, defined as:

$$\rho_1(\mathbf{r}, \mathbf{r}') = \langle \Psi_B^\dagger(\mathbf{r}) \Psi_B(\mathbf{r}') \rangle, \tag{1.27}$$

where $\Psi_B^\dagger$ is the creation operator of a boson at coordinates $\mathbf{r}$. Condensation manifests as a macroscopic occupation of the ground state, signaled as off-diagonal LRO in the one-particle density matrix, namely as a non-vanishing behavior for large distances $|\mathbf{r} - \mathbf{r}'|$:

$$\lim_{|\mathbf{r}-\mathbf{r}'|\to\infty} \rho_1(\mathbf{r}, \mathbf{r}') = \psi_B(\mathbf{r}) \psi_B^*(\mathbf{r}'), \tag{1.28}$$

where $\psi_B(\mathbf{r})$ is the macroscopic wavefunction of the bosonic condensate or its order parameter. This is intimately connected with the condensed fraction N_0/N, which is of order of 1 when the system is condensed. In particular, the condensate density is given by $n_0(\mathbf{r}) = |\psi_B(\mathbf{r})|^2$, so that an absorption imaging of a BEC directly reveals the order parameter of the condensate, since n_0 can be extracted right from a bimodal fit of the density profile.

On the other hand, the occupation number of a quantum state by fermions can never exceed unity because of Pauli principle, and the one-particle density matrix never shows a macroscopic occupation of one of its elements. LRO appears instead in the two-particle density matrix ρ_2, defined as [58]:

$$\rho_2(\mathbf{r}_1, \mathbf{r}_2, \mathbf{r}'_1, \mathbf{r}'_2) = \langle \Psi^\dagger_\uparrow(\mathbf{r}_1)\Psi^\dagger_\downarrow(\mathbf{r}_2)\Psi_\downarrow(\mathbf{r}'_2)\Psi_\uparrow(\mathbf{r}'_1)\rangle, \tag{1.29}$$

where $\Psi^\dagger_\uparrow(\mathbf{r})$ $(\Psi^\dagger_\downarrow(\mathbf{r}))$ is the creation operator of a fermion with spin up (down) at coordinates $\mathbf{r}$. The presence of a pair condensate is signaled as LRO in the long distance limit of ρ_2:

$$\lim_{|\mathbf{R}-\mathbf{R}'|\to\infty} \rho_2(\mathbf{r}_1, \mathbf{r}_2, \mathbf{r}'_1, \mathbf{r}'_2) = \psi(\mathbf{r}_1, \mathbf{r}_2)\psi^*(\mathbf{r}'_1, \mathbf{r}'_2), \tag{1.30}$$

where we introduced the center of mass notation of $\mathbf{R} = (\mathbf{r}_1 + \mathbf{r}_2)/2$ and $\mathbf{R}' = (\mathbf{r}'_1 + \mathbf{r}'_2)/2$. The function $\psi(\mathbf{r}_1, \mathbf{r}_2) = \langle \Psi^\dagger_\uparrow(\mathbf{r}_1)\Psi^\dagger_\downarrow(\mathbf{r}_2)\rangle$ is the order parameter of the fermionic condensate, associated with the Cooper pair wavefunction in BCS theory. In a condensate, the order parameter is a macroscopic quantity, from which we can calculate the density of condensed fermions $n_0(\mathbf{R})$ as:

$$n_0(\mathbf{R}) = \int d^3r |\psi(\mathbf{R} - \mathbf{r}/2, \mathbf{R} + \mathbf{r}/2)|^2, \tag{1.31}$$

where we used the relative coordinate $\mathbf{r} = \mathbf{r}_1 - \mathbf{r}_2$. The previous integral can be computed for a homogeneous system of density n to give [16, 59]:

$$n_0 = \frac{3\pi\sqrt{2}}{32} n \frac{\Delta}{E_F} \sqrt{\frac{\mu + \sqrt{\mu^2 + \Delta^2}}{E_F}}, \tag{1.32}$$

where Δ is the superfluid gap. In the BEC limit, the condensate density reduces to $n/2$, as expected for a molecular condensate of atomic density n. On the BCS side instead, n_0 is proportional to the gap, becoming exponentially small as the interactions are reduced. The condensed fraction n_0/n for a homogeneous gas in the crossover can be calculated by employing different theoretical methods, as reported in Fig. 1.6. All the theory curves reported show a decreasing trend starting from $n_0/n \simeq 1$ in the weakly interacting BEC regime to an exponential reduction as the BCS limit is reached. In fact, as interaction increases from the BEC limit, $1/k_F a \to 0^+$, higher momentum states are populated and the condensate is depleted as predicted by Bogoliubov theory of interacting BECs. On the BCS side instead, for $1/k_F a < 0$, condensed particles are concentrated only around the Fermi surface over a region of amplitude Δ, causing a depletion of the condensate as $1/k_F a \to -\infty$ because of the exponential suppression of the gap. The theoretical methods reported in Fig. 1.6 differ for the expected condensed fraction in the strongly-interacting regime, predicting at unitarity $n_0/n \simeq 0.7$ with mean field, $n_0/n = 0.57$ with Monte Carlo simulations and $n_0/n = 0.51$ with Luttinger-Ward formalism. We report also the value of $n_0/n = 0.43(2)$, recently calculated in Ref. [61] with auxiliary-field lattice Monte Carlo simulations.

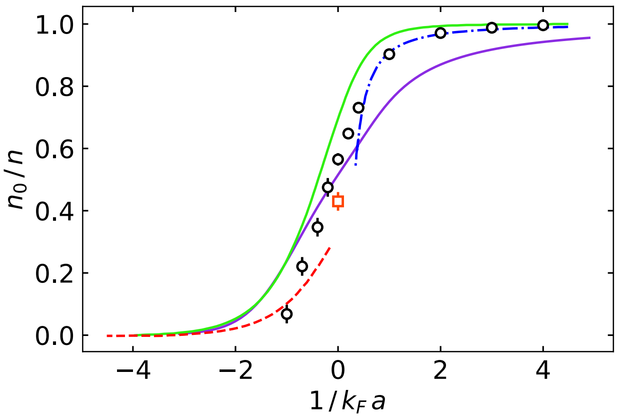

Figure 1.6: Theoretically predicted values of the pair condensed fraction across the BEC-BCS crossover. Black circles are obtained with Monte Carlo simulations, blue dot-dashed line represents Bogoliubov model for a molecular BEC with $a_B = 0.6\,a$, red dashed one the BCS theory, and green solid one a self-consistent mean-field theory, all taken from Ref. [60]. Purple solid line is obtained from Luttinger-Ward formalism of Ref. [41], whereas the orange square point is the value recently reported in Ref. [61], for the condensed fraction at unitarity, calculated with auxiliary-field lattice Monte Carlo simulations.

Measuring the condensed fraction of a fermionic condensate in not as simple as for a bosonic one. In fact, the condensate density is not directly accessible from the density profile of crossover gases, which we measure with absorption imaging, since they lose their bimodality as the Feshbach resonance is aproached from the BEC side. So far, condensed fraction measurements have employed the rapid ramp technique: crossover gases are projected into molecular BECs by rapidly sweeping the magnetic field towards the weakly interactly BEC regime. If the ramp is fast enough to transfer each fermion pairs into a tightly bound molecule, the bimodal density profile observed in the BEC regime provides a measurement of the condensate fraction of the crossover gas before the sweep. Such method has been used in both ^{40}K [62] and ^{6}Li [63] systems to extract the condensed fraction in the BEC-BCS crossover. Both experiments observed large condensate fractions throughout the entire crossover, with a measured value of $n_0/n \approx 0.7$ at unitarity. However, in both cases the sweeping time was comparable to the Fermi time $t_F = h/E_F$, so that the dynamics during the sweep could not be completely neglected. Furthermore, the conversion efficiency into molecules is expected to be higher for condensates [64], resulting in a higher measured condensed fraction after the sweep. Therefore, it is not clear how accurately the molecular condensate fraction observed with the rapid ramp technique reflects the pair condensate fraction of crossover gases. An alternative, direct method to measure the condensed fraction of a system is provided by the Josephson effect, which will be discussed in Sec. 1.4. As reported in Chapter 3, by realizing an atomic current-biased Josephson junction, we measure the condensed fraction of strongly-interacting fermionic superfluids throughout the BEC-BCS crossover.

1.2.6 Elementary excitations and superfluidity

Superfluidity, namely the capability of a system to flow without dissipation, is directly connected to its excitation spectrum. In fact, following the Landau criterion for superfluidity, a system cannot dissipate energy as long as its velocity with respect to a container at rest is smaller than the Landau's critical velocity, defined by [65]:

$$v_c = \min_k \frac{E_k}{\hbar k}, \tag{1.33}$$

where E_k is the system excitation spectrum at momentum k. Namely, for $v < v_c$ there are no excitations available in the spectrum and dissipation is inhibited. Crossover gases exhibit a superfluid behavior, as revealed from their excitation spectrum, that consists of two separate contributions: single fermions excitations, due to pair breaking, and collective Bose-like ones, connected with density fluctuations.

The required energy to break a pair can be calculated from the energy needed to add, or remove, a single fermion to the condensate. On a BCS gas, particles can be added only on top of the Fermi sphere because of Pauli exclusion principle, and the energy required for such purpose is Δ, which gives to the quantity the name of superfluid gap. In the BEC limit instead, the minimum energy to remove a particle becomes $\sqrt{\mu^2 + \Delta^2}$ [16]. When breaking a pair, two single fermions are created and the process costs thus 2Δ on the BCS limit and $2\sqrt{\mu^2 + \Delta^2}$ in the BEC one. As Δ is exponentially suppressed in the BCS limit of $1/k_F a \to -\infty$, pair breaking excitations are the lowest energy excitations here. On the other hand, the energy to break a tightly bound molecule in the BEC regime is much higher, and other kinds of excitations, as collective ones, occurs at lower energy.

As well as bosonic condensates, fermionic ones exhibit collective excitations, such as density fluctuations or sound waves [2]. Goldstone sound modes are associated with gauge symmetry breaking occurring with condensation and in BCS gases they are usually referred as Bogoliubov-Anderson (BA) modes. Those are gapless excitations characterized by the linear dispersion of phonons, that propagates with the sound velocity fixed by the compressibility of the gas: $mc_s^2 = n\partial\mu/\partial n$. In the BEC limit, the speed of sound is given by Bogoliubov theory as $c_s = \sqrt{\mu_B/m_B} = \sqrt{4\pi\hbar^2 a_B n_B/m_B}$, where n_B is the pair density, whereas in the BCS limit $c_s = v_F/\sqrt{3}$ and at unitarity $c_s = \sqrt{\xi/3}\, v_F$ [66], where $v_F = \sqrt{2E_F}/m$ is the Fermi velocity. In particular, the macroscopic dynamic of a crossover gas is governed by the hydrodynamic equations, that have the same form both for superfluid and classical collisional hydrodynamics [2]. In trapped clouds of finite size, the solutions of the those equations are collective modes with frequencies of the order of the trapping frequencies, that are independent on the density of states and do not change across the BEC-BCS crossover, as long as the system is hydrodynamic [2]. We note that hydrodynamic equations are valid only in the long-wavelength excitations regime, namely when the wavelength is larger than the so-called healing length ξ_h. In the BEC limit, $\xi_h \approx (na_B)^{-1/2}$, while in the BCS one $\xi_h \approx \hbar v_F/\Delta$, as the BA mode energy is of the order of the superfluid gap. In both cases, the healing length decreases approaching unitarity, where the only characteristic

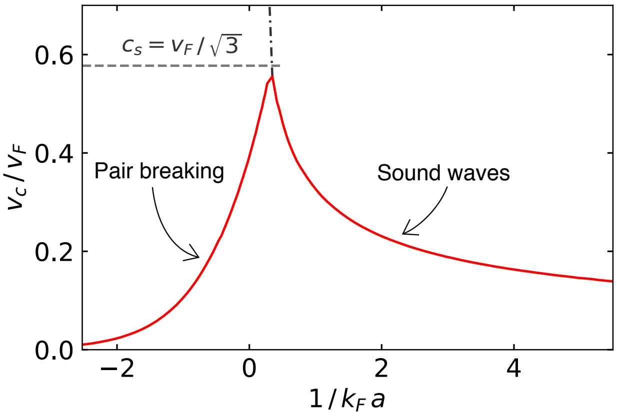

Figure 1.7: Critical velocity of fermionic superfluids in the BEC-BCS crossover in units of the Fermi velocity $v_F = \sqrt{2E_F}/m$. On the BEC side, for $1/k_F\,a > 0$, the lowest energy excitations are Bogoliubov sound modes, propagating at the speed of sound $c_s = \sqrt{\mu_B/m_B}$. On the BCS side, for $1/k_F\,a < 0$, sound modes propagate with $c_s = v_F/\sqrt{3}$ and are usually referred as Bogoliubov-Anderson (BA) modes. Here, pair breaking provides the lowest energy excitations that set the critical velocity to $v_c \approx \frac{\Delta}{\hbar k_F}$. Figure adapted from Ref. [16].

length is fixed by the interparticle distance and $\xi_h \approx k_F^{-1}$.

In general, the excitation spectrum of fermionic condensates includes both pair breaking and collective excitations: at low frequency, gapless phonons with linear dispersion prevail, while at high frequency a continuum of excitations emerges starting from a given threshold, above which pairs can be broken. In the BCS regime, the continuum of single-particles excitations starts at relatively low momenta, whereas in the BEC limit the phonon branch extends up to high frequencies, where the linear dispersion turns into the parabolic one of free particles. At unitarity, an intermediate behavior is expected, characterized by a phononic branch up to momenta of the order of k_F. Such an excitation spectrum allows for the calculation of the superfluid critical velocity as defined by Eq. (1.33), the predicted value of which is reported in Fig. 1.7. On the BEC side of the resonance, the critical velocity is given by the speed of sound c_s that monotonically increases as interactions are raised up to its maximum of $c_s = v_F/\sqrt{3}$ for BA modes in BCS gases. On the BCS side instead, pair breaking excitations prevail and the critical velocity $v_c \approx \Delta/\hbar k_F$ monotonically increases approaching unitarity. The two trend smoothly connect to each other near resonance, the critical velocity reaching its maximum value in the strongly-interacting regime, where the superfluid is the most stable. In particular, v_c is expected to be peaked slightly on the BEC side [67], as it was confirmed experimentally in Ref. [68], where the critical velocity was probed by subjecting the cloud to a moving optical lattice, and more recently in Ref. [69], where an obstacle of size comparable with the healing length was dragged on the atomic cloud. In both experiments, the measured v_c is found to be lower than the theoretically expected value, and in particular lower than the measured speed of sound in the BEC regime. In fact, in finite temperature systems, vortex-antivortex excitations can nucleate at points of minimal density due to density fluctuations, providing an additional way of dissipation for the system.

Quantized vortices

One of the most striking signature of superfluidity is the appearance of quantized vortices under rotation. In fact, long-range order in a condensate causes its motion to be irrotational, so that its behavior under rotation is strikingly different from the one of a collisional hydrodynamic gas, that admits rotational components in the velocity. In particular, irrotationality means that the velocity of the condensate is proportional to the gradient of its order parameter phase ϕ, namely [2]:

$$\mathbf{v} = \frac{\hbar}{2m}\nabla\phi. \tag{1.34}$$

When set into rotation, irrotationality prevents the superfluid to rotate like a rigid body, but the imparted angular momentum is carried via the formation of vortices with quantized circulation. In fact, the circulation of an irrotational system is given by:

$$\Gamma = \oint \mathbf{v} \cdot d\mathbf{l} = \frac{\hbar}{m}\oint \nabla\phi \cdot d\mathbf{l} = \frac{\hbar}{m}\Delta\phi, \tag{1.35}$$

where $\Delta\phi$ is the phase variation along the closed line. For the order parameter to be single-valued, $\Delta\phi = l \times 2\pi$ with l a natural number, leading to a quantized circulation of $\Gamma = l\,\frac{2\pi\hbar}{m}$. A quantized vortex is therefore associated with the appearence of a singulatity, with a wrap of a multiple of 2π of the phase around the vortex core, where the order parameter vanishes. In particular, the vortex core radius is of the order of the healing length, that for fermionic superfluids of ^{6}Li is of the order of one micron, which makes particularly challenging to observe them *in situ*, as it will be discussed in details in Chapter 5. Furthermore, crossover gases present a reduced contrast with respect to the case of BECs, since their density does not actually vanish despite the order parameter does. In the BCS limit, the order parameter is indeed exponentially small and the density is almost unaffected by the presence of a vortex. To observe vortices, a rapid ramp technique is usually employed: after switching off the trap, the magnetic field is quickly swept towards the BEC limit to project the gas into a molecular BEC where vortices are bigger and more visible. This technique allowed for the observation of vortex lattices in BEC-BCS crossover gases under rotation, providing a definitive evidence of their superfluid behavior [27]. With a similar protocol, we observe vortex nucleation in the wake of a moving obstacle through an oblate quasi-homogeneous unitary Fermi gas, as it will be presented in Chapter 5.

Condensed and superfluid fraction

The superfluid fraction n_s/n accounts for the portion of the system that shows a superfluid behavior, namely that doesn't respond to external rotation or shear motion. This is an independent quantity from the condensed fraction, as a system can show superfluidity even without being condensed, like for example a two-dimensional Bose gas, or viceversa a fully condensed system can be not superfluid, such as a non-interacting BEC. As already discussed, zero temperature crossover gases are entirely superfluid, i.e. their superfluid fraction is constantly equal to 1 throughout the BEC-BCS crossover at $T = 0$. As temperature is increased instead, thermally populated excitations in the system cause a part of it to be non-superfluid and n_s/n is expected to monotonically decrease approaching the critical temperature T_c, above which $n_s = 0$.

The first experimental measurement of the superfluid fraction of a unitary Fermi gas has been performed in Ref. [70] by exciting the second sound mode, namely an entropy wave in which the superfluid and the non-superfluid components oscillate with opposite phases. By measuring the speed of second sound, the extracted superfluid fraction was observed to be almost constant over a large range of temperature, quickly dropping only close to the critical one. The behavior of crossover superfluids in the strongly interacting regime of $-1 < 1\,/\,k_F\,a < 1$ is expected to be similar, which is however still to be confirmed experimentally.

1.3 Transport measurements with cold atoms

The dynamic behavior of a system relies on both its equilibrium properties, namely on its ground state, and on the excitations on top of it. In solid state physics, transport measurements are routinely employed to identify the character of a material, defining whether it is an insulator, a conductor or a superconductor. Similarly, the dynamical behavior of an atomic system reveils the inner properties of its quantum state, identifying superfluidity and condensation. Moreover, cold atoms have proven to be the perfect playground for investigating theoretical models and problems related to condensed matter physics, such as the Hubbard model [6,7], topological quantum matter [24] or the already mentioned BEC-BCS crossover. In fact, ultracold gases are fully controllable system, in which the interactions, the geometry and the amount of disorder can be tuned at will. The interest in transport properties of ultracold atoms originates thus from both the fundamental quest about many-body physics and the prospect of realizing a quantum simulator of solid state devices. In particular, for the purpose of having a direct comparison between measurements carried out in the real and simulated device, it is essential to reproduce the solid state physics phenomenology and extract from the cold atom system the same observables. As ultracold gases are charge-neutral, transport is here intended as mass, heat or spin transport and the conductivity of an atomic system is defined in terms of these quantities.

A variety of different approaches has been employed to test transport properties of quantum gases, all constrained by the isolated nature of those systems, which prevents the connection to a generator of current or bias to induce transport. Contrarily to the solid state counterpart, cold gases thus do not allow the existence of a steady dc current and their dynamic response is intrinsically transient. Different methods have been applied to investigate quantum gases transport, such as the response to an external force, that led to the observation of Bloch oscillations in a periodic systems [71], or the free expansion of the cloud, that demonstrated Anderson localization in disordered

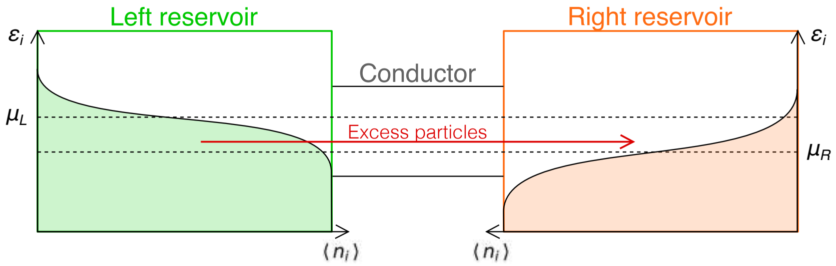

Figure 1.8: Sketch of the scheme for realizing a two-terminal transport measurement with ultracold fermionic gases. Two reservoirs are connected by a conductor, than can be a channel, a quantum point contact or a barrier, and a chemical potential bias $\Delta\mu = \mu_L - \mu_R$ is introduced between them, yielding a different energy distribution in the two. The excess of particles in the left reservoir above the Fermi energy of the right one drives a net current towards the latter, that can be monitored by measuring the number of particles in the two versus time.

gases [72, 73], or the already mentioned rotation of the cloud excited by a periodic circular motion of a repulsive obstacle, which allowed for the observation of quantized vortices in bosonic and fermionic condensates [27,74,75]. Despite providing valuable informations about the state of the system and mirroring solid state phenomenology, the mentioned strategies do not allow for a direct connection with the concepts of conductivity or conductance, typical of condensed matter physics. To adress such quantites, the Landauer two-terminal approach [31], sketched in Fig. 1.8 for an ultracold fermionic gas, can be employed. The system of interest is composed of two particles reservoirs connected by a conductor, which can be a channel, a quantum point contact or a barrier. The reservoirs are intended as statistical mechanics reservoirs, which have large enough compressibility, heat capacity and spin susceptibility, that chemical potential, temperature or spin potential are not affected by exchange of particles through the conductor. When a small bias is introduced between the two reservoirs, in Fig. 1.8 represented as the chemical potential difference $\Delta\mu = \mu_L - \mu_R \ll \mu_{R,L}$, a resulting current through the system is observed, originating from the excess of particles in the left reservoir above the Fermi energy of the right one. The chemical potential bias acts thus as a thermodynamic force, driving a current of the extensive, thermodynamically conjugate quantity of particle number. Similarly, a temperature or spin bias could be introduced in one of the two reservoirs to provoke a heat or spin current through the conductor [31]. After having initialized the system in the depicted configuration, the current is let free to flow and monitored by measuring the evolution of number of atoms, temperature or spin imbalance between the two reservoirs versus time. We note that the current originates from an energy window, of width set by the bias, around the Fermi level, ensuring transport as a property of the Fermi surface, as typical of condensed matter physics. The two-terminal configuration provides thus a device approach in direct analogy with solid state to investigate the conduction properties of ultracold gases. Given the fermionic nature of electrons, ultracold fermionic gases are the perfect candidate to realize a quantum simulator of highly correlated electrons. The two-terminal transport scheme is a very versatile approach, that allowed for the investigation of ballistic and diffusive transport of particles through a channel [76], as well as for the thermoelectric effect in the same configuration [77], and the observation of the quantized conductance of a quantum point contact, namely a tightly confined one-dimensional conductor [78, 79].

1.4 Tunneling transport of fermionic superfluids

A peculiar example of a two-terminal scheme is the investigation of tunneling properties of an ultracold gas by connecting the two reservoirs with a thin barrier. When the reservoirs are condensed and show phase coherence, their wavefunctions can overlap in the barrier region and interfere with one another. Under such conditions, the Josephson effect takes place, linking the macroscopic particle current flowing through the barrier with the elusive phase of the order parameter. Since its theoretical discovery in 1962 [33], the Josephson effect has been demonstrated in a variety of both bosonic and fermionic systems, such as superconductors [80], liquid Helium-4 [81, 82] and Helium-3 [83], ultracold bosonic [84] and fermionic [85] atoms and photonic systems [86]. Despite differing in both constituents, nature and strength of the interactions, all the afore mentioned systems share the fundamental feature of being composed of a condensate. In fact, as it will be discussed further below, the Josephson effect relies on the presence of a macroscopic order parameter in the two reservoirs constituting the junction. The phase coherence between the two condensates drives a dissipationless current through the barrier, sustained up to a maximum value, called the critical current, that depends on the amplitude of the order parameter. Therefore, the Josephson effect is sensitive to both phase and amplitude of the order parameter, providing a powerful probe for any condensed state. In Sec. 1.4.1, we first discuss the phenomenon from a superconducting junction point of view, to successively demonstrate in Sec. 1.4.2 that an atomic one is described by exactly the same equations, called the Josephson equations, realizing a perfect quantum simulator of the solid state case. The same phenomenology emerges thus in both superconducting and atomic Josephson junctions, and we present a protocol for measuring the critical current of the latter in analogy with the solid state case. Finally, in Sec. 1.4.3 we provide a microscopic description of the tunneling process in atomic superfluids, in order to connect the macroscopic observables of Josephson effect, the critical current and the conductance, to the microscopic properties of the junction.

1.4.1 The Josephson effect

The Josephson effect was firstly discovered by B. D. Josephson in 1962 [33] in the context of a superconducting junction as the one depicted in Fig. 1.9: two superconductors are separated by an insulating barrier, thin enough to allow their order parameters to overlap below it. The resulting coupling between the superconductors drives a dissipationless current I_s, or supercurrent, to flow through the barrier, merely sustained by the relative phase difference between their order parameters. In particular, Josephson predicted a sinusoidal current-phase relation in the limit of weak coupling, namely for

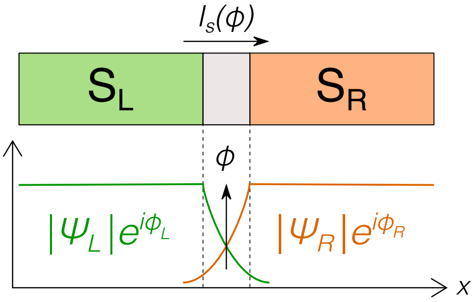

Figure 1.9: Sketch of a superconducting Josephson junction geometry. Two superconductors (S_L and S_R) are separated by a insulating barrier (gray region), thin enough to allow the order parameters of the two, $|\Psi_L|e^{i\phi_L}$ and $|\Psi_R|e^{i\phi_R}$, to overlap under the barrier. When this happen, a dissipationless current may arise across the junction, solely depending on the phase difference $\phi = \phi_L - \phi_R$ between the two wavefunctions.

low transmission probability through the barrier:

$$I_s(\phi) = I_c \sin\phi, \tag{1.36}$$

where I_c is the Josephson critical current, i.e. the maximum supercurrent sustained by the junction. Furthermore, the time-evolution of the relative phase can be obtained from the main principles of quantum mechanics as [87,88]:

$$\hbar\dot{\phi} = qV, \tag{1.37}$$

where $q = 2\,e$ is the charge of the carriers, that in superconductors are Cooper pairs, while V is the potential difference across the junction. Eqs. (1.36) and (1.37), called Josephson equations, fully describe the behavior of a superconducting Josephson junction (SJJ), identifying the two regimes of stationary (dc) and non-stationary (ac) effects, depending on whether the variables change with time or not. In the dc Josephson effect of constant ϕ, a current $I_s < I_c$ can flow through the junction without developing any drop of potential across it, namely keeping $V = 0$. On the other hand, an applied voltage V triggers an alternating current (ac Josephson effect), oscillating at frequency $qV/\hbar$, while the phase difference linearly increases. We note that there is an important difference between Eq. (1.36) and Eq. (1.37) that describe the Josephson effect: whereas the latter is rigorously derived from the main principles of quantum mechanics, the first is only an approximation, and deviations from a sinusoidal current-phase relation may be observed. A more general expression of the current-phase relation will be derived in Sec. 1.4.3.

The critical current of an SJJ depends on the microscopic properties of the tunneling particles, and its exact temperature dependency is given by the Ambegaokar-Baratoff relation [89]:

$$I_cR_n = \frac{\pi\Delta}{2e}\tanh\left(\frac{\Delta}{2k_BT}\right), \tag{1.38}$$

where R_n is the junction resistance in the normal (non superconducting) state and Δ is the superconducting gap. At $T = 0$, the previous relation reduces to $I_cR_n =$

$\pi\Delta(0)/2e$, meaning that the zero temperature critical current is directly proportional to the superconductors order parameter. Therefore, Josephson effect provides a powerful probe of the order parameter, as long as a measurement of the critical current can be performed. In SJJs, the critical current is routinely extracted from the current-voltage characteristic [90], obtained by measuring the developed potential across the junction after having injected a controlled current into it. As it will be discussed in the following, a similar method can be employed to access the critical current of atomic Josephson junctions as well.

1.4.2 Atomic Josephson junctions

The Josephson junction geometry of Fig. 1.9 can be easily implemented in an atomic sample by bisecting the cloud with a repulsive optical barrier. When the two reservoirs are condensates, the same phenomenology of SJJs emerges, enriched by novel regimes introduced by interactions, such as the macroscopic quantum self-trapping (MQST). The Josephson effect for an atomic junction was first retrieved for weakly interacting BECs, the Gross-Pitaevskii equation (GPE) leading to small periodic oscillations as solutions [91,92]. In particular, the oscillation frequency is determined by the interplay of two characteristic energies: the charging energy E_C and the tunnelling energy E_J. The first introduces a nonlinearity that, when exceeding the critical value of $E_C > E_J$, drives the system into self-trapped solutions with the relative population oscillating around a nonzero value, namely a MQST regime. Successively, the same phenomenology of periodic oscillations and MQST has been predicted for fermionic superfluids as well, by numerically solving the time-dependent Bogoliubov-de Gennes equations (BdG) [93].

To describe the behavior of an atomic Josephson junction, whether composed by a bosonic or a fermionic condensate, we can employ the two-state model, that associates an independent wavefunction $\psi_{L,R}$ to each of the two reservoirs, characterized by a number of carriers $N_{L,R}$ and a phase $\phi_{L,R}$. According to this model, the condensates dynamics is described in terms of an effective Hamiltonian, where the population imbalance $k = \frac{N_L - N_R}{2}$ and the relative phase $\phi = \phi_L - \phi_R$ are seen as conjugate variables [91,93,94]. Focusing on the intermediate Josephson regime of $N^{-2} \ll E_C/E_J \sim 1$, the effective Hamiltonian can be written as:

$$H = \frac{E_C}{2}k^2 - E_J \cos\phi, \tag{1.39}$$

from which we can steadily derive the equations of motion for k and ϕ as:

$$\dot{k} = -\frac{1}{\hbar}\frac{\partial H}{\partial \phi} = \frac{E_J}{\hbar}\sin\phi, \tag{1.40}$$

$$\dot{\phi} = \frac{1}{\hbar}\frac{\partial H}{\partial k} = \frac{E_C}{\hbar}k. \tag{1.41}$$

For $|\phi| \ll 1$, the solution of the previous equations is given by periodic oscillations of both ϕ and k, out of phase of $\pi/2$ one with respect to the other and characterized by a frequency $\omega_p = \frac{1}{\hbar}\sqrt{E_C E_J}$, called plasma frequency in analogy with solid state physics. We now show that the two previous equations have the same form of Eqs. (1.36) and (1.37), once the energies E_J and E_C are expressed in terms of current and chemical potential difference, respectively. In fact, in an atomic junction the current is given by the number of carriers tunneling through the barrier per unit time, which is related to the population imbalance by $I = -\dot{k}$. Therefore, Eq. (1.40) can be expressed in term of particle current as:

$$I = I_c \sin\phi, \tag{1.42}$$

where we have defined the critical current of an atomic Josephson junction as $I_c = E_J/\hbar$. Moreover, the charging energy is usually calculated as $E_C = \frac{\partial\mu_L}{\partial N_L} + \frac{\partial\mu_R}{\partial N_R} = 2\frac{\partial\mu_L}{\partial N_L}$, where μ_L (μ_R) is the chemical potential of the left (right) reservoir [92]. When a finite chemical potential difference $\Delta\mu = \mu_L - \mu_R$ is introduced into the junction, the charging energy can be written as $E_C = 2\Delta\mu/\Delta N = \Delta\mu/k$, leading to the following expression for the phase time-evolution of Eq. (1.41):

$$\hbar\dot{\phi} = \Delta\mu. \tag{1.43}$$

Eqs. (1.42) and (1.43), describing the behavior of an atomic Josephson junction, are completely equivalent to Eqs. (1.36) and (1.43) for SJJs, the chemical potential difference playing the role of the voltage drop for neutral atoms. Therefore, both superconducting and atomic Josephson junctions manifest the same Josephson effect phenomenology. We note that the previous equations can be formally derived from GPE for weakly interacting BECs, but are expected to be valid also for molecular BECs of fermionic atoms. Moreover, they can be extended throughout the BEC-BCS crossover of fermionic superfluids as long as pair-breaking excitations are irrelevant with respect to the phononic ones that characterize bosonic superfluids [93]. In the fermionic case, transport is mediated by bosonic pairs that compose the fermionic condensate below the critical temperature. Therefore, the current described by Eq. (1.42) is a pair current, simply connected to the total atomic one by a factor of 2 accounting for the number of atoms in a pair, namely $I_B = I/2$, where the subscript $_B$ identifies the pair quantities. Similarly, the chemical potential to plug in Eq. (1.43) is the pair chemical potential $\mu_B = 2\mu$. Therefore, the Josephson equations describing the behavior of a fermionic atomic junction are the same as for the bosonic case, once pair quantities are considered to account for the different nature of the carriers.

The Josephson effect in atomic junctions has been widely demonstrated both with bosonic and fermionic superfluids. On the one hand, the study of bosonic condensates has unveiled all the predicted interactions regimes from Rabi ($E_C/E_J \ll N^{-2}$) to MQST ($E_C/E_J \gg 1$) [84, 95, 96]. On the other hand, the Josephson regime of plasma oscillation has been observed also with fermionic superfluids, both with three- [85] and two- [32] dimensional clouds. In particular, in the previous work performed by our group reported in Ref. [85], plasma oscillations in both population imbalance and relative phase were observed through the BEC-BCS crossover, phase-shifted by $\pi/2$ one respect to the other. By initializing a small population imbalance across the junction, the Josephson dynamics was triggered and successively characterized by monitoring the time evolution of both imbalance and phase. From the out-of-phase oscillations of these conjugates variables, the plasma frequency has been measured across the BEC-BCS crossover, allowing for the extraction of the tunneling energy E_J. The obtained trend of E_J was observed to exhibit a maximum slightly on the BCS side of the resonance, mirroring the expected behavior of I_c in the crossover, which will be discussed in detail in Sec. 1.4.3. However, the plasma oscillation regime explored in Ref. [85] could not give access to a direct and precise measure of the critical current, that could only be extrapolated from the plasma frequency.

As for SJJs, the critical current of an atomic Josephson junction can be directly measured from the current-voltage, or more properly current-chemical potential, characteristic of the junction. As first proposed in Ref. [97] for a weakly interacting BEC, the complete characteristic of an atomic junction can be obtained by realizing a current-biased Josephson junction. To do that, the repulsive barrier has to be set into motion inside the cloud, to induce a current of tunneling particles moving in the opposite direction. For small enough injected current, namely below the critical one, the junction does not develop any chemical potential difference, the relative phase adjusting its value to support the current according to Eq. (1.42). On the other hand, when the injected current exceeds I_c, the dc Josephson regime is not supported anymore, and the junction exhibits a resistive behavior. The transition happening at the critical current is signaled by a kink in the measured chemical potential difference, allowing thus for a direct measurement of I_c. Such protocol has been experimentally demonstrated for a bosonic Josephson junction in Ref. [98], where the dc Josephson effect was observed for the first time in an atomic junction. As it will be discussed in detail in Chapter 3, we implemented the same method to directly measure the critical current on fermionic superfluid across the BEC-BEC crossover, and to observe for the first time the sinusoidal current-phase relation characteristic of the dc Josephson effect.

1.4.3 Microscopic description of tunneling

As already mentioned, the sinusoidal current-phase relation predicted by Josephson is an approximation, holding only in the tunneling regime of strong barriers [87, 88]. A more general current-phase relation can be obtained by considering the simmetry properties of the supercurrent. As a first constraint, for the current to be single-valued, $I_s(\phi)$ must be a periodic function of period 2π, so that we can expand it in a Fourier series of sinusoidal functions. However, we should also require the superfluid to be time-reversal invariant in the case of s-wave pairing, so that only the odd terms of the series should be non-zero. In fact, if we reverse time, the Josephson current should flow in the opposite direction, namely $I_s(\phi) \to -I_s(\phi)$ for $t \to -t$. As the phase is an odd function, the Fourier expansion of the current reduces to [88]:

$$I_s(\phi) = \sum_{n=1}^{\infty} I_n \sin(n\phi), \tag{1.44}$$

where the coefficients I_n account for the coherent tunneling of n pairs through the barrier, and they are proportional to the tunneling probability amplitude $|t|$. In the limit of strong barrier, characterized by $|t| \ll 1$, only the first term describing the tunneling of a single pair remains non-negligible, and Josephson's sinusoidal current-phase relation is retrieved.

An expression for the various orders of the current I_n can be obtained by treating the tunneling problem in a perturbative way, as proposed in Ref. [34] for weakly interacting BECs. In particular, the atomic Josephson junction Hamiltonian can be approximated as:

$$\hat{H} = \hat{H}_L + \hat{H}_R + \hat{H}_T, \tag{1.45}$$

where $\hat{H}_L$ ($\hat{H}_R$) is the Hamiltonian of the left (right) reservoir, while $\hat{H}_T$ describes the transfer of particles from one reservoir to the other. A rigorous derivation of the tunneling Hamiltonian is not obvious, but it is expected to take the form [34]:

$$\hat{H}_T = -\sum_{l,r} t_{l,r}\, \hat{a}_l^\dagger\, \hat{a}_r + \, h.c., \tag{1.46}$$

where $\hat{a}_l^\dagger$ ($\hat{a}_r^\dagger$) is the creation operator of a boson in the left (right) reservoir, $t_{l,r}$ are the tunneling amplitudes and the sum runs over all the eigenstates $|l\rangle$ and $|r\rangle$ of the left and right reservoir respectively. When the tunneling energy E_J is small compared to the ground state energies of $\hat{H}_{L,R}$, the tunneling Hamiltonian can be treated perturbatively. In the first order in the tunneling amplitude, only a dissipationless current arises, accounting for the exchange of bosons from condensate to condensate. Here, by dissipationless we mean that the flow of particles does not cause any chemical potential difference across the junction. In the second order instead, contributions describing condensate-to-noncondensate and noncondensate-to-noncondensate tunneling appear, and also dissipative currents develop. In particular, up to the second order, the dissipationless current takes the form [34]:

$$I_s(\phi) = I_c \sin\phi + I_2 \sin(2\phi), \tag{1.47}$$

where the critical current is proportional to the tunneling energy $I_c = E_J/\hbar$. The detailed expressions of the critical and second order currents depend on the tunneling amplitudes $|t_{r,l}|$, as the two currents are proportional to their first and second power respectively. On the other hand, the dissipative current can be written in terms of a normal conductance G_n as:

$$I_{diss} = G_n \Delta\mu_B, \tag{1.48}$$

where $\Delta\mu_B$ is the bosonic chemical potential difference developed across the junction. Arising only at second order, the normal conductance shows a quadratic dependence on the tunneling amplitudes $|t_{l,r}|$. In the following, a microscopic description of the dissipationless currents I_c and I_2 and the normal conductance G_n is presented, both for weakly interacting BECs and for fermionic condensates.

Dissipationless currents

A unified microscopic description of the Josephson effect throughout the BEC-BCS crossover is a challenging problem, as the strongly correlated many-body system is hard to address theoretically. Different approximate methods are able to calculate the critical current, but they apply only either in the BEC or in the BCS limit. Of particular interest are the microscopic calculations of the Josephson currents based on the solution of Bogoliubov-de Gennes equations (BdG) [93, 99, 100], which provide a characterization of the critical current throughout the crossover. In particular, the calculated I_c for a given barrier height shows a non-monotonic trend with a maximum around unitarity, slightly shifted on the BCS side of the resonance. Such a behavior is interpreted in Ref. [99, 100] as due to the interplay between Landau critical velocity of Fig. 1.7 and pair breaking, that pose a natural limit for the dissipationless superflow through the barrier. Despite providing a qualitatively correct description of the critical current in the entire crossover region, as verified by the observed behavior of E_J in Ref. [85], this approach is expected to be quantitatively reliable only deep in the BCS limit.

On the other hand, for homogeneous weakly interacting BECs, an exact expression of the critical current can be analytically computed, based on the tunneling Hamiltonian description. In fact, considering two condensed reservoirs occupying a cubic volume L^3 each, separated by a square potential barrier of height V_0 and width d, the tunneling amplitudes $|t_{l,r}|$ can be analytically computed from the knowledge of the wavefunctions of the condensed reservoirs. For this specific case, the critical current density $j_c = I_c/L^2$ takes the form [34, 101]:

$$\hbar j_c = \frac{\mu_B \, n_0}{2k(\mu_B)} |t(\mu_B)|, \tag{1.49}$$

where $k(\mu_B) = \sqrt{2m_B\mu_B}/\hbar$ is the wave vector of a boson of mass m_B and chemical potential μ_B, $|t(\mu_B)|$ is the single-particle transmission amplitude and n_0 is the density of condensed bosons in the reservoirs. We note that the previous expression is strictly valid only in the limit of strong barrier, when $V_0 \gg \mu_B$. The critical current density therefore can be separated in two contributions, accounting respectively for the bulk properties of the condensate and the single-particle tunneling amplitude. Such separation between many-body and single-particle properties is kept also in the second order current density $j_2 = I_2/L^2$ which, under the same approximations, is related to the first order contribution via:

$$|j_2| = j_c \frac{|t(\mu_B)|}{4}. \tag{1.50}$$

The previous equations are strictly valid only in the weakly interacting BEC limit, but it has been proven in Ref. [101] that an extension of them to fermionic superfluids is able to quantitatively reproduce both numerical simulation results and experimental data over a wide range of parameters. In particular, in the fermionic case, the current is given by a flux of pairs, so that the pair chemical potential $\mu_B = 2\mu$ and the pair condensed fraction should be taken into account. A hint of why such an extension is well-founded is provided by the fact that Eq. (1.49) essentially coincides with the current density expected for a BCS gas by the Ambegaokar-Baratoff formula of Eq. (1.38), once variables are properly recast. In particular, the bosonic transmission amplitude $|t(\mu_B)|$ of a pair should be replaced by the transmission probability $|t(2\mu)|^2$ of a single fermion.

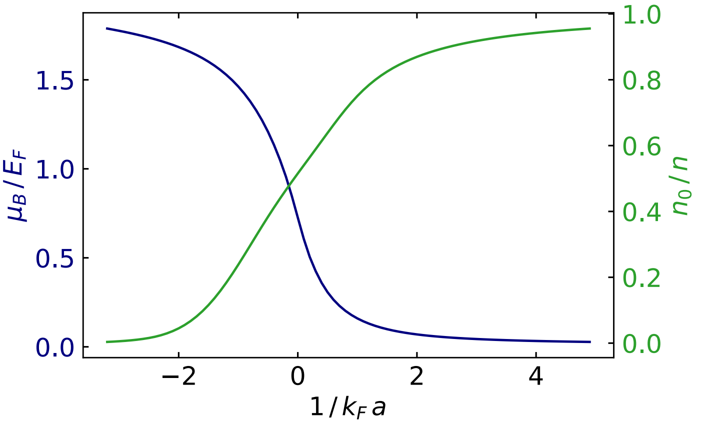

Figure 1.10: Pair chemical potential and condensed fraction of an homogeneous gas across the BEC-BCS crossover. The first (blue line) monotonically decreases when going from the BCS side, where it takes the value of $2\,E_F$ in the limit of $1/k_F\,a \to -\infty$, to the BEC one. Conversely, the condensed fraction (green line) is exponentially suppressed in the BCS regime and monotonically increases towards the BEC one, where the whole gas is condensed. According to Eq. (1.49), the critical current is expected to show a non-monotonic trend peaked around unitarity, given by the competition of condensed fraction and pair chemical potential. Both curves are obtained with the Luttinger-Ward formalism of Ref. [41].

Remarkably, the validity of Eq. (1.49) for fermionic superfluids is able to explain the theoretically predicted and experimentally observed maximum of I_c in the BCS side of the resonance. In fact, the critical current density of Eq. (1.49) depends on both the chemical potential and the condensed fraction, that have a competing behavior in the crossover, as depicted in Fig. 1.10. While the condensed fraction monotonically decreases moving from the BEC to the BCS limit, the chemical potential has an opposite trend, reaching its maximum value on the BCS side of the resonance while monotonically decreasing towards the BEC one. As a result, the critical current is expected to show a non monotonic behavior, peaked around unitarity.

Normal conductance

Under the assumption of a homogeneous Josephson junction with weakly interacting BECs of Ref. [34], the normal conductance can be calculated as well. In particular, two different contributions originate from the condensate-to-noncondensate and the noncondensate-to-noncondensate tunneling, so that the normal conductance can be written as:

$$G_n = G_{an} + G_{nc}, \tag{1.51}$$

where the subscript $_{an}$ indicates an *anomalous* contribution to G_n. G_{an} accounts for the tunneling of a condensed particle coherently converted into a phononic excitation, an effect that is completely absent in BCS superconductors. In fact, whereas the excitation spectrum of a BEC admits gapless phonons (Bogoliubov modes), in superconductors such modes are turned into gapped plasma ones by the Coulomb interaction [102]. In particular, G_{an} of a weakly interacting BEC is found to be proportional to the condensed density n_0 [34]. On the other hand, the non-condensate contribution G_{nc} originates from the incoherent tunneling of Bogoliubov quasiparticles across the barrier, that shows a dependence on the temperature of the reservoirs, and in particular $G_{nc} \sim T^4$ [34]. Therefore, at $T = 0$ only the anomalous contribution survives, fostered by the condensate, with dissipative conduction in a bosonic Josephson junction remaining finite even at zero temperature. Then, for increasing temperature, G_{an} decreases as the condensate is depleted, while the non-condensate contribution increases until it becomes the dominant term at high T.

A theoretical study of the normal conductance of a fermionic Josephson junction is not available, yet the presence of an anomalous term analogous to the bosonic case is expected. In fact, an anomalous contribution in the conductance has been predicted for interacting BECs in a quantum point contact [36], where G_{an} is found to be inversely proportional to the interaction strength, suggesting that it should become less relevant when approaching the Feshbach resonance. On the other hand, BCS superfluids admit an anomalous contribution as well, as it has been demonstrated for a quantum point contact [35]. Here, G_{an} originates from the conversion of condensed pairs into the gapless Bogoliubov-Anderson modes, that are equivalent to Bogoliubov modes in BCS theory. Therefore, an anomalous contribution to the normal conductance might be present even in crossover superfluids, giving rise to a non-zero conductance even at zero temperature.

Chapter 2

Experimental setup

Ultracold atoms and quantum gases offer the perfect playground for quantum simulation. They are highly controllable systems, in which, in addiction to the already mentioned control over the inter-atomic interactions provided by Feshbach resonances, both the dimensionality and the geometry can be freely decided as well, by means of optical dipole potentials. Off-resonant laser light can be indeed employed to squeeze the atomic cloud in one or two directions, implementing thus two- or one-dimensional systems, as well as to sculpt the potential landscape in which the sample has to evolve, by tailoring the laser light intensity with spatial light modulators. Furthermore, the recent advance in the production of high-resolution optical systems adds a further level of controllability of the sample, which can be monitored with unprecedented spatial resolution. This chapter discusses the recent upgrade on both the manipulation of the cloud with arbitrary optical potentials and its detection with a high-resolution imaging system.

The chapter is organized as it follows. In Sec. 2.1, an overview of the vacuum and the laser systems for the production and manipulation of an ultracold ^{6}Li sample is presented, together with the procedure we employ to reach the degenerate state and a description of the newly developed radio-frequency source. Sec. 2.2 reports on the characterization and successive implementation of a high-resolution microscope objective, employed for both imaging the atomic cloud and imprinting repulsive potentials on it with a sub-micron resolution. The optical setup for the creation of arbitrary optical potentials with a Digital Micromirror Device (DMD) is presented in Sec. 2.3, which discusses the developed control program for the device as well.

2.1 Preparation of the atomic sample

Cold atoms experiments need to be performed under vacuum, to isolate the sample from hot thermal background particles, that would limit its lifetime. Our apparatus is composed of the Ultra-High-Vacuum (UHV) system sketched in Fig. 2.1 (a), a detailed description of which can be found in Ref. [103]. The atomic sample is initially produced inside the oven, where an artificially enriched ^{6}Li sample is heated up to 420° to create an atomic beam, successively collimated by a copper cold finger. The hot

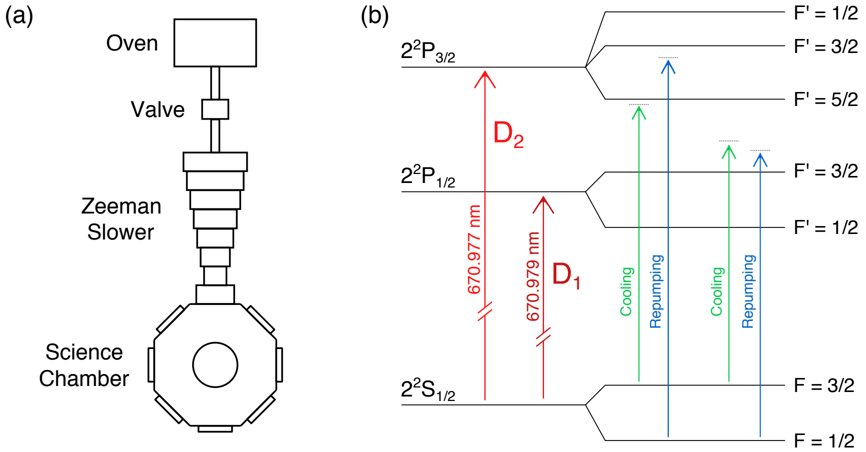

Figure 2.1: Experimental apparatus for the production of fermionic superfluids with ^{6}Li. (a) Vacuum system for the creation of the atomic sample. A fast collimated atomic beam exits the oven, it is slowed down by the Zeeman slower and finally reaches the science chamber. Here, it is first laser cooled and then brought to degeneracy by means of evaporative cooling in an all-optical dipole trap. (b) Energy levels of ^{6}Li at zero magnetic field. The fine level structure identifies the D_1 and D_2 lines at 670.979 nm and 670.977 nm respectively, used for laser cooling the atomic sample. Cooling and rempumping lights are produced by two dedicated AOMs to address the proper transition in the hyperfine splitting of the two lines.

atomic beam is decelerated by the Zeeman slower down to a velocity of about 60 m/s before entering the science chamber, a custom-made octagonal stainless-steel cell from Kimball Physics, kept under a pressure below 10^{11} mBar. Here, atoms are cooled down by means of the standard laser cooling techniques of a Magneto-Optical Trap (MOT) and a gray molasses, and successively transferred into an optical dipole trap where they are evaporatively cooled down to degeneracy, as it will be discussed in detail in Sec. 2.1.2. The production of the atomic sample, as well as its detection, employ different laser sources and a radio-frequency source, which are presented further below.

2.1.1 Laser sources for ^{6}Li manipulation

To manipulate ^{6}Li atoms we employ both resonant light for slowing, cooling and imaging the sample, and off-resonant light to confine it into optical dipole traps.

The level structure of ^{6}Li atoms at zero magnetic field is sketched in Fig. 2.1 (b): the two fine structure lines of D_1 and D_2, addressing respectively the $^2S_{1/2} \rightarrow ^2 P_{1/2}$ and the $^2S_{1/2} \rightarrow ^2 P_{3/2}$ transitions, present a wavelength of almost 671 nm. We use two Toptica TA-Pro lasers, both set to work around such wavelength and amplified by a MOPA amplifier, to address the two transitions. A saturation spectroscopy setup is implemented to lock the laser frequencies to the D_1 and D_2 transitions respectively. Being the hyperfine splitting of the ground state manifold 228 MHz large, cooling and repumping lights for both the MOT and the gray molasses are produced from the same laser source of D_2 and D_1 respectively, by fine tuning their wavelength with a chain of Acousto-Optical Modulators (AOMs) [103]. D_2 laser light is employed for imaging the cloud as well, by means of the absorption imaging technique that will be discussed in detail in Sec. 2.2.2. In particular, we finely tune the laser frequency via a dedicated setup to make it resonant with the atomic transition at the high magnetic field we use to produce fermionic superfluids. We employ two different paths for the imaging, one on the horizontal and one on the vertical direction (see Fig. 2.2). The horizontal imaging setup is composed by a simple telescope of two $f_{H1} = 150$ mm and $f_{H2} = 1000$ mm lenses, providing a magnification of 6.72. The atom image is focused on an Andor Ultra camera, set on the Fast Kinetic Series (FKS) acquisition mode, which allows for taking a sequence of a few images with a short delay time on the order of $200\,\mu$s, at the price of using a smaller portion of the CCD chip [104]. In between the horizontal imaging path, we can add a movable imaging setup with a low magnification of 0.5, well suited for checking the MOT cloud and the efficiency of the IPG loading. For this secondary horizontal imaging, the light is focused on a Stingray camera by a movable $f_{H3} = 75$ mm lens. The vertical imaging light is instead propagating from top to bottom, as visible from the sketch in Fig. 2.2 (b), and features a high resolution microscope objective, the properties and characterization of which will be presented in Sec. 2.2.2.

Optical dipole traps

To trap the atomic sample, we use far off resonance laser light, that exerts a conservative force on atoms originating from the interaction between the electric field of the laser light and the induced atomic dipole moment. In particular, the electric field $\mathbf{E}$ induces a dipole moment $\mathbf{p} = \alpha\mathbf{E}$ that oscillates at the same frequency ω of the laser light. Here α is the complex polarizability of the atomic medium. The induced dipole moment in turn interacts with the driving electric field, giving rise to the dipole interacting potential:

$$U_{dip} = -\frac{1}{2}\langle \mathbf{p} \cdot \mathbf{E} \rangle = -\frac{1}{2}\,\mathrm{Re}(\alpha)|E|^2, \tag{2.1}$$

where the brackets denotes a time average and the factor $\frac{1}{2}$ takes into account that the dipole moment is induced and not a permanent one [105]. By considering that the field intensity can be written as $I = 2\epsilon_0 c|E|^2$, where E is the electric field amplitude, it is clear that the dipole potential is directly proportional to the intensity of the laser light. To get an explicit expression for it, the complex polarizability can be calculated in a semiclassical approach by considering the interaction between a two-level atom with the classical radiation field to give [105]:

$$U_{dip}(\mathbf{r}) = \frac{3\pi c^2}{2\omega_0^3}\frac{\Gamma}{\Delta}I(\mathbf{r}), \tag{2.2}$$

where ω_0 is the resonance frequency of the atomic transition, Γ its linewidth and $\Delta = \omega - \omega_0$ is the detuning of the laser light from the transition. The dipole potential therefore reflects the spatial profile of the light intensity and it is whether attractive or repulsive according to the frequency of the laser light. In particular, when the light

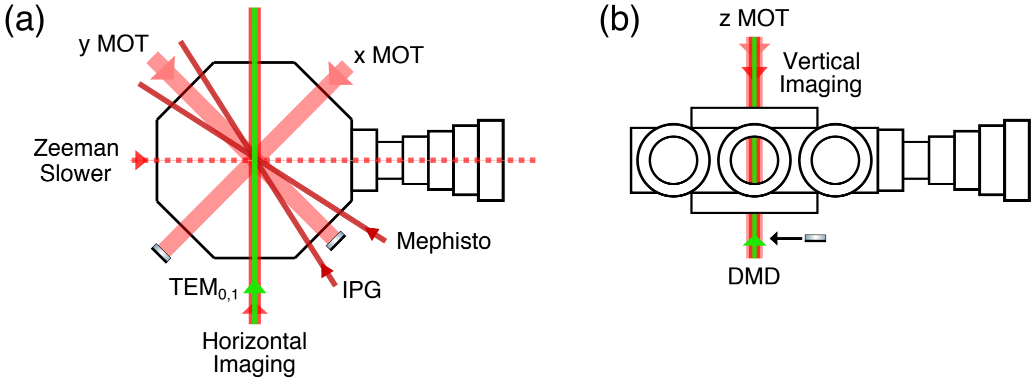

Figure 2.2: Sketch of the laser beams employed to manipulate the atomic cloud in the science chamber in a top view (a) and in a side one (b). The Zeeman slower beam is depicted as red dashed line. x and y MOT beams are retroreflected by static mirrors, while the z one has a movable mirror that retroreflects the beam during the MOT stage. The mirror is successively removed to free the way for imaging and DMD beam, impinging on the atom cloud from top and bottom, respectively (see Sec. 2.2 for details). The angle between IPG and Mephisto beam is 14°, while the TEM$_{(0,1)}$ beam is collinear to the horizontal imaging one.

is red-detuned, $\Delta < 0$, U_{dip} is negative and atoms are attracted into the maxima of the light field intensity. On the other hand, for blue-detuned light with $\Delta > 0$, U_{dip} is positive and atoms are repelled by the laser light, so that potential and intensity minima coincides. Despite being non resonant, the laser light of the optical dipole trap can anyway be absorbed by atoms and subsequently re-emitted as dipole radiation. The scattering rate of such process is related to the immaginary part of the complex polarizability and, in the semiclassical approach already adopted, it is given by [105]:

$$\Gamma_{sc}(\mathbf{r}) = \frac{1}{\hbar\epsilon_0 c}\,\mathrm{Im}(\alpha) I(\mathbf{r}) = \frac{3\pi c^2}{2\hbar\omega_0^3}\left(\frac{\Gamma}{\Delta}\right)^2 I(\mathbf{r}). \tag{2.3}$$

The scattering rate scales thus as I/Δ^2 whereas the dipole potential like I/Δ, so that it is convenient to employ optical dipole traps with large detuning and high intensity to keep the scattering rate as low as possible and thereby avoid atom losses.

In our experiment, we use both red-detuned infrared lasers, to perform an all-optical evaporation of the atomic sample, and a blue-detuned green one, to shape the dimensionality and the geometry of the sample, arranged as depicted in Fig. 2.2. The evaporation process employs two high power infrared beams: the IPG and the Mephisto. The former is a 1073 nm multi-mode ytterbium fiber laser with a maximum power of 200 W, that is used to trap the atoms after the MOT phase. The intensity of such beam is stabilized by an AOM controlled via a PID feedback loop. In addition, the central frequency and the amplitude of the AOM driving signal are modulated out of phase to increase the beam waist up to about 80 μm, while keeping Gaussian the profile of the beam [103]. To create the final optical dipole trap, the IPG beam is crossed with the 1064 nm Mephisto one, obtained from a Nd-YAG crystal with a maximum output power of 50 W. Such beam has a circular waist of about 40 μm and it is focused onto the atomic cloud with an angle of 14° with respect to the IPG. As for the latter, its power is stabilized by an AOM controlled via a PID feedback loop [103].

To manipulate the geometry and the dimensionality of our atomic cloud we employ two different beams, the DMD and the TEM$_{(0,1)}$ one, both produced from a blue-detuned Coherent Verdi V-8 laser at 532 nm. The DMD light is sent onto the atomic cloud from bottom to top, and its detailed setup for arbitrary patterns projection will be presented in Sec. 2.3. The TEM$_{(0,1)}$ light propagates instead on the horizontal direction, collinear with the horizontal imaging beam, and its node in the vertical intensity profile allows for squeezing the cloud along such direction, as it will be discussed in detail in Sec. 5.1. The power of both the green beams is stabilized by dedicated AOMs controlled via a PID feedback loop.

2.1.2 Cooling procedure to the degenerate regime

Our experimental apparatus can produce both strongly-interacting fermionic superfluids and a non interacting Fermi gas, starting from the same laser cooled sample. In the following we present a short overview of the cooling protocol employed in our experiment, referring to Ref. [103] for a detailed description of each step of it.

As already mentioned, the hot atomic beam exiting the oven first passes though a Zeeman slower [106–108]. Such tool decelerates the atomic beam from a velocity of the order of 800 m/s down to 60 m/s, thanks to the combined action of a laser beam, resonant with the D_2 transition and counter propagating respect to the atomic beam, and an inhomogeneous magnetic field, that keeps the light resonant with the atomic transition. The slowed atomic beam is successively captured in a Magneto-Optical Trap (MOT) [106–108] composed by retroreflected resonant laser beams in the 3 spatial directions (see Fig. 2.2) and a quadrupolar magnetic field, produced by a pair of coils in anti-Helmotz configuration, called the MOT coils. The MOT loads about 10^9 atoms with a temperature around 500 μK in 5 seconds. When the loading is completed, the MOT lights and field are switched off and the gas is cooled down to about 50 μK with an efficient sub-Doppler scheme based on gray molasses, that exploits the D_1 transition [109]. The D_1 light for the molasses is sent to the atomic sample via the same path of x, y and z MOT beams. After this second stage of laser cooling the sample is transferred into the IPG optical dipole trap (ODT) where evaporative cooling technique is performed to reach quantum degeneracy. In particular, after the ODT is loaded and a second stage of gray molasses is performed inside the trap, we ramp the Feshbach magnetic field up to 832 G, on top of the $|1\rangle - |2\rangle$ scattering resonance, where we perform the evaporation to create fermionic superfluids. The IPG beam is successively crossed with the Mephisto one, where the atomic sample completes the evaporative process to give generally 10^5 atoms per spin state at a temperature of the order of 30 nK. The final crossed trap is cigar shaped, the axial trap frequency being $\sim$ 15 times smaller than the radial one. When the evaporation is over, we sweep the Feshbach magnetic field to vary the scattering length a_{12} between states $|1\rangle$ and $|2\rangle$ to explore fermionic superfluids in the BEC-BCS crossover.

We employ a different evaporative protocol to create an ideal Fermi gas, that is by definition composed of non-interacting particles. However, to effectively cool the sample we need interactions, so that thermalization can occur. Therefore, we start anyway the evaporation of an ideal Fermi gas on top of the $|1\rangle - |2\rangle$ scattering resonance, but before reaching the pairing temperature we sweep the magnetic field to about 300 G where interactions are not strong enough to enter the superfluid regime. As visible in Fig. 1.3, the $|1\rangle - |3\rangle$ resonance is much more favorable for the evaporation at such field, presenting a scattering length a_{13} at 300 G that is almost 3 times a_{12}. Therefore, immediately after the beginning of the evaporation, we sweep the magnetic field down to 585 G, where $a_{12} \simeq a_{13}$ and here we transfer the population from $|2\rangle$ to $|3\rangle$ by means of radio-frequency (RF) pulses generated by the source presented in the next section. In particular, we employ the rapid adiabatic passage technique to transfer the whole population of $|2\rangle$ in the $|3\rangle$ state [104, 107], and then sweep down the field to 300 G where the rest of the evaporative process takes place. As the scattering length a_{13} is much lower than on top of the resonance, the evaporation ramps for the ideal Fermi gas production have to be slower than the ones employed for fermionic superfluids, lasting about 3 s more than those. At the end of the evaporation, the Feshbach field is swept to 572 G where $a_{13} \simeq 0$ and the $|1\rangle - |3\rangle$ mixture is non-interacting. Typically, 10^5 atoms per spin state at $T/T_F \simeq 0.1$ compose the produced ideal Fermi gas, which can be turned into a spin-polarized gas by shining a spin-selective resonant pulse of light on the cloud to remove one of the spins out of the trap.

2.1.3 Radio-frequency source

In addition to the presented laser sources, a fundamental tool to prepare, manipulate and probe fermionic superfluids of ^{6}Li is radio-frequency (RF) spectroscopy. At the high fields used to produce fermionic superfluids or the ideal Fermi gas, the energy shifts between the three lowest hyperfine states $|1\rangle$, $|2\rangle$ and $|3\rangle$ of ^{6}Li are of the order of $h \times 80$ MHz, and can be thereby addressed by employing a single RF source. The control over the internal state of the atomic sample provided by RF allows not only to create a balanced $|1\rangle - |2\rangle$ or $|1\rangle - |3\rangle$ mixture to efficiently evaporate the gas, but also to probe the properties of degenerate Fermi gases [16]. In fact, the RF coupling can be employed to measure the excitation spectrum of fermionic superfluids [28–30], as well as for quenching the system out of equilibrium [110–112] or to create impurities and subsequently probe their evolution in the gas [113, 114].

The RF field is typically produced by a few cm-large antenna, placed close to the atomic sample to produce a constant electro-magnetic field over the size of the cloud. As the wavelength of RF field is very long (~ 3 m), the momentum transferred to atoms during an RF transition is negligible, so that it couples only internal states of each individual atom, providing a fundamental control over the spin degree of freedom. Ideally, for experiments with ultracold fermions, an RF source should be able to rapidly and efficiently probe the system or quench it out of equilibrium over a time-scale compara-

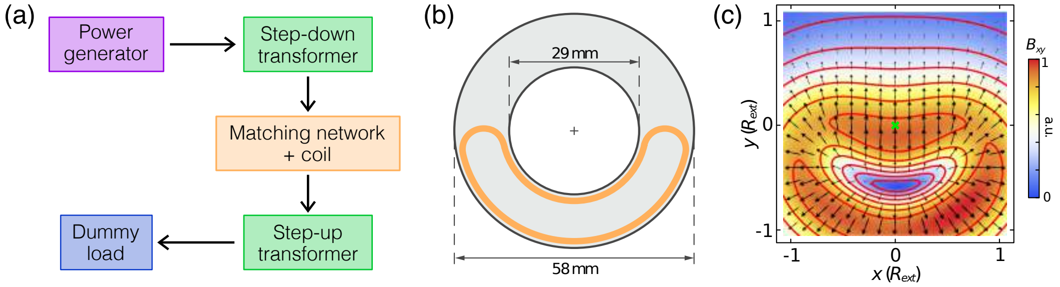

Figure 2.3: Newly developed RF source for coupling the three lowest hyperfine states of ^{6}Li. (a) Block diagram of the RF source circuit. The working principle of the system is based on two impedence transformers, that serve to maximize the current flowing through the RF coil. (b) Sketch of the coil geometry (orange wire) folded inside a 3D printed holder, custom made to fit on top of the top re-entrant viewport of the science chamber. The holder has an annular shape in the $x - y$ plane so to let the imaging and z-MOT light to freely enter the chamber. In particular, it is characterized by an outer radius of $R_{\text{ext}} = 58$ mm and an inner one of $R_{\text{int}} = 28$ mm. (c) Field lines of the RF component $|B_{xy}|$ on the atomic $x - y$ plane, the distances of which are expressed in terms of the outer coil radius R_{ext}. The position of the atomic sample is marked by the green cross.

ble with the Fermi time $t_F = \hbar/E_F$ [16], which is the minimum collective response time in interacting fermionic systems and of the order of $\sim 25\,\mu$s in our experimental conditions. Such requirement is not easy to be accomplished for ^{6}Li atoms, since their low magnetic moment determines a weak coupling with external magnetic fields. In particular, at the high fields used in our experiment, the ^{6}Li differential magnetic moment $\Delta\mu \simeq h \times 10$ kHz/G is weak compared to other alkali atomic species, requiring a strong RF field to achieve a high Rabi frequency, i.e. a large transfer rate [115]. Moreover, the RF system should be properly designed to disturb as least as possible the other laboratory electronic instrumentation and to not introduce noise or electro-magnetic field fluctuations in the rest of the experimental apparatus.

During this thesis work, we develop a new RF source that satisfies all the mentioned requirements. Here, we only give a brief overview of the upgraded RF system, which will the subject of a forthcoming publication. As sketched in the block diagram of Fig. 2.3 (a), the circuit includes a variable capacitance, that we employ to finely tune the matching frequency of the source to be resonant with the $|2\rangle - |3\rangle$ transition frequency of ~ 82 MHz at high field. The circuit is designed to provide a wide enough resonance to efficiently address the $|1\rangle - |2\rangle$ transition as well, which we use to produce a balanced mixture before the beginning of the evaporation. In our experiment, the Feshbach field employed to produce degenerate Fermi gases sets the quantization axis to be aligned with the vertical direction, so that only the RF field component orthogonal to it contributes to the coupling between the hyperfine states. For this purpose, we design the novel coil geometry sketched in Fig. 2.3 (b), that produces a strong magnetic field component on the $x - y$ plane, $|B_{xy}|$, which is homogeneous all over the cloud volume, as visible in (c), and makes the RF source both efficient and fast, as the Rabi frequency

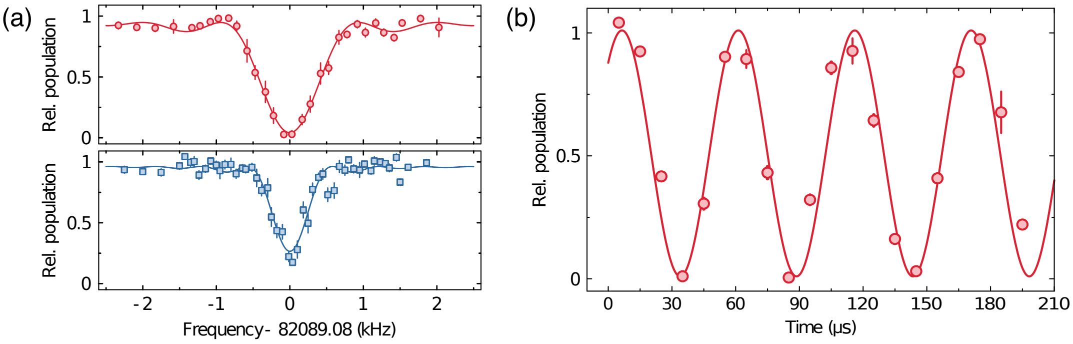

Figure 2.4: Characterization of the new RF source. (a) RF spectroscopy of the $|3\rangle \rightarrow |2\rangle$ transition performed on a spin polarized non-interacting Fermi gas of atoms in $|3\rangle$ at 770 G. The relative population is measured after an RF pulse of 1 ms at 55 mW power (top) and one of 2.5 ms at 5.5 mW (bottom). The two datatsets are fitted with a Sinc function to extract the resonance frequency of 82.08908 MHz. (b) Rabi oscillation between the $|3\rangle$ and $|2\rangle$ states after a pulse at $\sim$ 100 W of variable duration. The measured Rabi frequency of 18.25 kHz guarantees a π-pulse of 27.4 μs.

of the transition scales linearly with $|B_{xy}|$ [115]. We implement the new RF source in the experimental setup by placing the coil on the top re-entrant viewport of the science chamber, as close to the atomic cloud as possible, whereas the variable capacitance of the circuit is left reachable to freely tune the RF central frequency.

In Fig. 2.4 we report the characterization of the new RF source, performed on a spin-polarized Fermi gas of atoms in $|3\rangle$ produced with the procedure presented above. In (a) we report two spectroscopies of the $|3\rangle \rightarrow |2\rangle$ transition at 770 G, performed by measuring the atom population in $|3\rangle$ after applying an RF pulse of 1 ms at 55 mW power and one of 2.5 ms at 5.5 mW for the red circle and blue square data, respectively. By fitting the profile with a Sinc function [115], we extract the resonance frequency of 82.08908 MHz and a half width of 250 Hz for the lowest power spectroscopy. We note that the different width of the two spectroscopy lines in Fig. 2.4 (a) is due to Fourier broadening. We then estimate the highest Rabi frequency reachable in our experimental setup by measuring Rabi oscillations between $|2\rangle$ and $|3\rangle$ states when the antenna is operated at resonance with the maximum power of $\sim$ 100 W. As reported in Fig. 2.4 (b), by varying the pulse duration, we observe the relative population in the two states to perform undamped oscillations, as expected for a coherent and spatially homogeneous coupling between the two states [115]. The Rabi frequency characterizing such oscillations is measured to be 18.25 kHz, which guarantees a π-pulse to transfer all the population from one state to the other of 27.4 μs duration, of the order of our typical Fermi time. The new RF source will be therefore a valuable tool for future spectroscopic investigations, as its high Rabi frequency can be employed to study the fast dynamic of relaxation after a quench or of impurities in strongly-correlated systems.

2.2 High resolution optical system for imaging and DMD projection

Information on the atomic sample, such as number of atoms, temperature and density distribution, is obtained in our experiment via absorption imaging: an image of the atomic cloud is acquired by shining on it a resonant pulse of light and then recording the shadow cast by the atoms on a camera, focused by an optical imaging system. We already presented in Sec. 2.1 our horizontal imaging setup, that features a simple telescope of lenses to image the atom cloud. On the other hand, on the vertical direction we employ a more sophisticated imaging system based on a high-resolution microscope objective, custom made by Special Optics, the optical properties of which are listed in Table 2.1. The re-entrant viewport on the bottom of the science chamber allows for exploiting a short working distance of 25.1 mm, which includes the optical path through the 6 mm silica window as well and guarantees the high numerical aperture of 0.45. The microscope objective features the same focal point for both resonant light at 671 nm and blue-detuned light at 532 nm, so that it can be employed not only for imaging the atomic cloud with a high resolution, but also for projecting DMD-made optical potentials defined over a micrometer length scale. Furthermore, the objective is designed to focus the collimated z MOT beam arriving from the top of the cell at a distance of about 7 cm from its first lens, so that it can be properly retro-reflected during the MOT stage. In the following we present the characterization of the microscope objective optical properties, and the subsequent implementation of it in the experimental setup.

2.2.1 Characterization of the microscope objective

A composite imaging system can be fully characterized from a measurement of its Point Spread Function (PSF), that provides information about its resolution and the aberrations that might affect it. Neglecting the effect of polarization, the process of image formation can be described by considering the relation between the electric field amplitude of an object U_o and that of its image U_i created by the system at a distance z_i from it. In particular, the image U_i can be obtained as the convolution between the PSF of the imaging system h and the geometric optics image prediction

NA	0.45
Effective focal length	47 mm
Field of view	0.33 mm
Working distance	25.1 mm
AR coating	670 nm, 532 nm, 1064 nm

Table 2.1: High-resolution microscope objective optical properties. We note that the working distance takes into account the path through the 6 mm thick silica viewport.

$U_g(x, y) = U_o(\frac{x}{M}, \frac{y}{M})/M$, where M is the magnification of the imaging system [116]:

$$U_i(x, y) = h(x, y) \otimes U_g(x, y). \tag{2.4}$$

Therefore, the PSF acts as the transfer function of the imaging system, and contains all the information about it. For a diffraction limited optical system, the PSF is given by the Airy profile [116]:

$$h(x, y) = \frac{A}{\lambda z_i} \frac{J_1(u)}{u}, \tag{2.5}$$

where A is a constant amplitude, λ the wavelength of the light illuminating the object, J_1 the Bessel function of the first kind of order 1 and $u = \frac{2\pi w r}{\lambda z_i}$, with $r = \sqrt{x^2 + y^2}$ and w being the radius of the most limiting aperture of the optical system. However, in the presence of aberrations the PSF gets distorted and the profile deviates from the Airy one.

The PSF can be used to quantify the spatial resolution of the optical system, defined as the minimum distance between two objects to still appear separated on the imaging plane. According to the Rayleigh criterion, two point sources are optically resolved if the maximum of the PSF of the first coincided with the first minimum of the PSF of the second. With this definition, the spatial resolution is quantified as the Airy radius of the PSF, that can be expressed in terms of the imaging system properties as [117]:

$$R_A = 0.61 \frac{\lambda}{\text{NA}}, \tag{2.6}$$

where NA is the numerical aperture of the imaging system. With the previous expression we can calculate the nominal spatial resolution of our microscope objective of NA = 0.45: at $\lambda = 671$ nm the Airy radius is expected to be 910 nm, while at $\lambda = 532$ nm is 721 nm, below one micron in both cases. The presented definition of resolution bases on the PSF being described by the Airy profile of Eq. (2.5) or more generally by Airy-like profiles that still present a zero. However, in the presence of aberrations this assumption may fail, and the Rayleigh criterion is not valid anymore. A practical criterion for the spatial resolution is to describe it as the full width at half maximum (FWHM) of the PSF, which can be more easily measured. With this second definition, the resolution is connected to the properties of the imaging system by the relation [117]:

$$\text{FWHM} = 0.51 \frac{\lambda}{\text{NA}}. \tag{2.7}$$

The expected FWHM for our microscope objective is 760 nm for $\lambda = 671$ nm and 603 nm for $\lambda = 532$ nm. The difference between the two definitions is small, since the spatial resolution of a diffraction limited optical system is of the order of half the ratio λ/NA.

To completely characterize an imaging system, its PSF should be thus measured. From Eq. (2.4) we note that, when the object is a point source, namely its geometric image U_g is a Dirac delta function, the image profile U_i coincides with the PSF. One way of characterizing an imaging system is therefore to use an object with dimensions

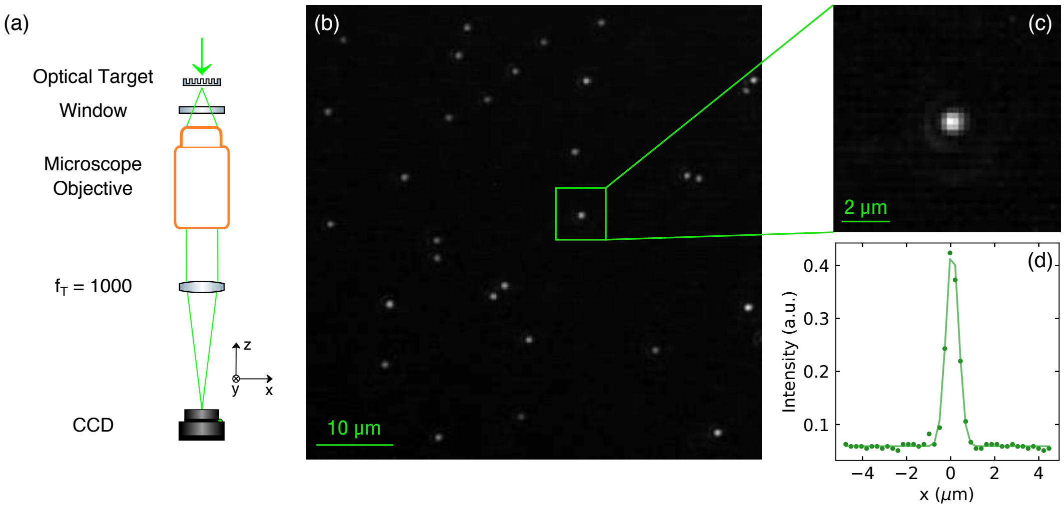

Figure 2.5: Measurement of the microscope objective PSF. (a) Sketch of the optical setup used for the characterization of the objective. (b) Image of the optical target seen through the objective and tube lens system. Each spot provides a direct measurement of the PSF. (c) Zoom of (b) in correspondence of one of the spots. The PSF shows an Airy profile, the first ring of which is feebly visible. We measure the resolution of the objective by performing a two-dimensional Gaussian fit of the PSF. (d) Comparison between a horizontal cut of (c) and its two dimensional Gaussian fit. The cut is operated in correspondence of the fitted center of the Gaussian.

well below the resolution, that effectively acts as a point source and allows for the direct measurement of the PSF on the imaging plane. To perform the characterization of the high resolution microscope objective, we use an optical target made of a reflecting material in which a random distribution of sub-micrometer sized holes was caved. The average dimension of such holes is 200 nm, well below the nominal resolution of the objective for both red and green lights, so that they can be reasonably approximated with point sources. To test the objective performances we implement the optical system sketched in Fig. 2.5 (a): the optical target is illuminated with a laser beam at the testing wavelength of 532 or 671 nm, the transmission of which is collected by the microscope objective and then focused on a Thorlabs CCD camera by an achromatic tube lens of focal length $f_T = 1000$ mm. To reproduce the working condition of the real experiment, in between the optical target and the objective we place a silica window of the same 6 mm thickness as the science chamber viewport. Objective and tube lens are mount on a three-dimensional translation stage, and can be moved together to find the position at which the optical target is on the focal plane of the objective. The composite optical system they form provides a magnification of $M = 21.8$, measured by focusing on the camera an object of well known dimensions.

A typical image of the optical target, acquired with the CCD when the imaging system is on focus, is presented in Fig. 2.5 (b): each sub-micrometer hole appears as a spot on the camera and the image provides many independent measurements of the

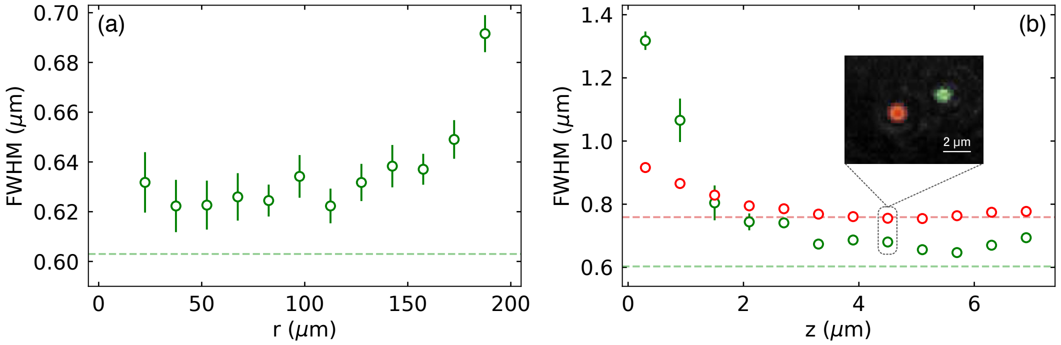

Figure 2.6: Characterization of the microscope objective imaging properties. (a) Measurement of the field of view at 532 nm: the FWHM extracted from the two-dimensional fit of the PSF is plotted versus the distance of the spot from the image center. Points are obtained by binning inside a 15 μm width annulus. Errorbars denote the standard deviation of mean. Dashed green line indicates the nominal resolution of the microscope objective of FWHM = 603 nm. (b) Characterization of the objective focal length at 532 and 671 nm, obtained by illuminating the optical target with the two wavelengths simultaneously. The FWHM of the PSF at $\lambda = 532$ nm (671 nm) is plotted as green (red) circles as a function of the z position of the objective. Dashed lines identify the nominal resolution of the system at the two wavelengths . Inset: image of a single hole in the optical target, illuminated with red and green light at the same time. Because of chromatic aberration, the PSFs at the two wavelengths are separated by 3.54(1) μm when the hole is on focus.

PSF. When zooming on one particular spot, as for Fig. 2.5 (c), it is possible to see the Airy profile of the PSF, with the first ring feebly visible. Each spot is fitted with a two-dimensional Gaussian function to provide a measurement of the waist σ of the PSF. To quantify the resolution of the objective we estimate the FWHM of the PSF by using the relation: $\text{FWHM} = 2\sqrt{2\ln 2}\,\sigma \simeq 2.355\,\sigma$.

To find the focal position of the objective, we restrict our attention on a smaller central region of the camera and move the translation stage to find the minimum FWHM. Once on focus, we acquire an image of the largest region of the optical target visible with the CCD, that, given the 1024 × 1280 pixel of the camera and 5.2 μm dimension of each pixel, corresponds to a 242 × 303 μm area. A region like that of the optical target typically contains several hundreds of holes, that allow for a measurement of the field of view of our imaging system. To do that, we extract the FWHM of each spot and plot it versus the radial distance from the center of the area r, as reported in Fig. 2.6 (a) for $\lambda = 532$ nm. The resolution of the objective is observed to be almost constant over a region of about 150 μm radius, compatible with the nominal field of view of 300 μm of the objective. By averaging all the independent measurements of the FWHM inside the field of view, we obtain that the resolution of the objective at $\lambda = 532$ nm is 630(10) nm. By repeating the same procedure with red light at $\lambda = 671$ nm, we obtain a resolution of 830(10) nm at such wavelength. Both for red and green lights, the measured resolution is in agreement with the nominal one within 10%.

As a last check of the optical properties of the objective, we verify that the focal plane for red and green light is the same. To do that, we illuminate the optical target with the two wavelengths simultaneously and characterize their PSF. As can be seen on the inset of Fig. 2.6 (b) the same hole in the optical target is imaged into two different spots for green and red light because of chromatic aberration. This effect allows to measure the PSF at 532 and 671 nm at the same time, and characterize their focal position. To do that, we restrict our attention to the single couple of spots reported in the inset, and measure the FWHM of the two PFSs varying the position of objective and tube lens along the z direction with the translation stage. As can be seen from the plot in Fig. 2.6 (b), there is a region of at least $3\,\mu$m in which both red and green spots FWHM is minimum, which verifies that the focal length of the objective is the same at 532 nm and 671 nm. In this region, the distance between the two spots is measured to be $3.54(1)\,\mu$m. We note that the value of FWHM for green (red) reported in Fig. 2.6 (b) is higher (lower) than the measured average resolution already reported. This is due to fluctuations on the measurement of the PSF, the FWHM of which is in fact averaged over hundreds of independent fit to get a reliable estimation of the resolution. On the other hand, data in Fig. 2.6 (b) are obtained from the PSF measurement of a single spot, binned over about 5 different acquisitions inside the sampling distance of 60 nm.

Implementation in the experimental setup

The high resolution microscope objective has been implemented into the experimental setup according to the sketch in Fig. 2.7. Objective and tube lens are connected by a rod system and mounted together on a motorized three-dimensional translation stage basing on a tilt-pitch platform. The motorized translation stage provides a minimal displacement step of the order of a few tens of nm, that allows for the daily fine tuning of the z position of the objective to put the atom cloud on focus. The rod system ends with a 45° tilted elliptical mirror that directs the vertical imaging beam incoming from the top of the cell to an Andor IXon3 EMCCD camera placed on the optical table (see Fig. 2.8). To optimize the position of the composite system of objective, tube lens and elliptical mirror, we first align the imaging beam to the vertical direction and center it on the atomic cloud. Then the position of the objective on the $x-y$ plane and its tilt are optimized by maximizing the transmission through an alignment target concentric to the tube lens and placed on top of it. Such procedure guarantee that the optical axis of the composite system is aligned with the vertical and that the atomic cloud is centered on the field of view of the objective. The magnification of objective and tube lens optical system is measured to be 21.82, obtained by displacing the cloud of a controlled amount and measuring the corresponding translation on the Andor camera. In particular, to do that we move the focus of the IPG beam by acting on its last lens translation stage.

The z MOT beam is incoming to the cell from top, as well as the imaging beam. To retroreflect such MOT beam we use a $0.5'$ mirror mounted on a Newport motorized translation stage and placed in the back focal plane of the objective at a distance of

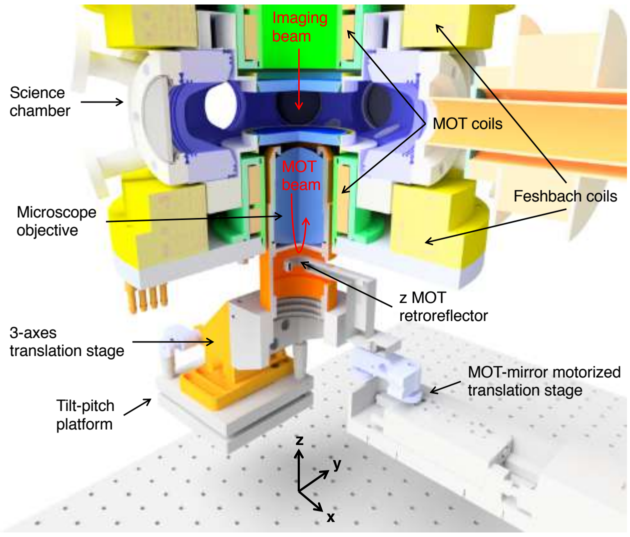

Figure 2.7: Sketch of the implementation of the microscope objective in the experimental setup. The objective is placed on the bottom of the science chamber, at a few millimeter distance from the re-entrant viewport. It is mount on a motorized three-dimensional translation stage basing on a tilt-pitch platform that allows for the daily tuning of its z position to have the atomic cloud on focus. The z-MOT retroreflecting mirror is mounted on a motorized translation stage that insert it in the objective during the MOT stage of the experimental sequence and remove it at the end of it.

about 7 cm from its first lens. The mirror is inserted in the objective optical path through a hole in its housing structure, caved for this purpose. A quarter waveplate has been glued on top of the retroreflecting mirror to adjust the polarization of the MOT beam. The Newport translation stage guarantees a high stability in the final position of the mirror, at the price of a long positioning time that takes the first 2 s of each experimental cycle. Then, at the end of the MOT stage the mirror is moved outside from the objective to clear the path for the other vertical beams of imaging and DMD.

2.2.2 High-intensity imaging system

To measure the cloud density distribution in the $x-y$ plane we employ the high-resolution microscope objective already presented and a high-intensity absorption imaging technique. We illuminate the cloud with a resonant high-power pulse impinging from top, and image the shadow of atoms that have absorbed the light on the Andor camera. In particular, the imaging setup implemented for the high resolution vertical imaging is sketched in Fig. 2.8. The shadow image of the atomic cloud is collected by the microscope objective and focused by the tube lens. A couple of elliptical mirrors direct first the light from vertical to horizontal direction and then to the Andor IXon3 EMCCD camera. The imaging light passes through a 2” polarizing beam splitter (PBS), implemented to combine the imaging path with the DMD one, that will

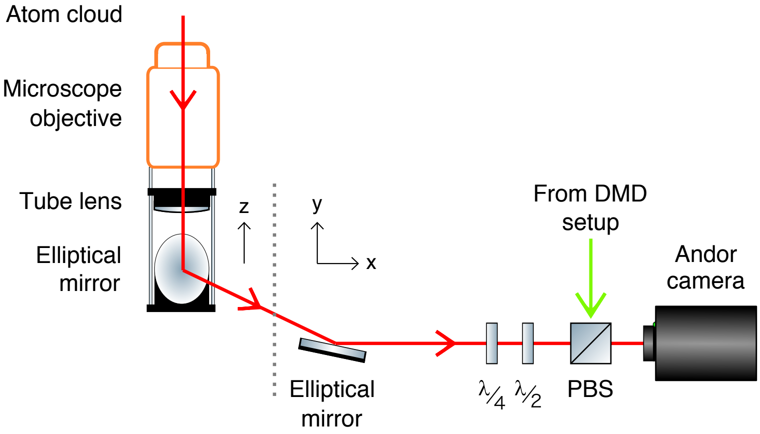

Figure 2.8: Sketch of the vertical imaging optical setup. The image of the shadow cast by the atom cloud is collected by the objective and then focused by the tube lens of $f_T = 1000$ mm into an Andor IXon3 EMCCD camera. The imaging beam is directed into the horizontal plane by an elliptical mirror tilted by 45° and mounted together with the objective and tube lens via a rod system. A second elliptical mirror directs the light towards the camera, after passing through a 2" PBS to combine imaging and DMD paths. The $\lambda/4$ and $\lambda/2$ waveplates set the polarization of the imaging beam so that it is completely transmitted by the PBS.

be discussed in detail in Sec 2.3. The polarization of the imaging beam is set by the $\lambda/4$ and $\lambda/2$ waveplates to be completely transmitted by the PBS. Before implementing the imaging setup, we tested that the resolution of the objective is not affected by introducing PBS and waveplates into the optical path, as long as the beam is not cut from these optics. To avoid this issue, we place the waveplates and PBS as close as possible to the Andor camera and employ 2" elliptical mirrors in the optical path. The Andor camera is operated on the Fast Kinetic Series (FKS) acquisition mode: we acquire the sequence of 3 images required for the absorption imaging with a short delay time of the order of $200\,\mu$s, by reducing the portion of the camera chip illuminated by the light [104].

As already mentioned, for the vertical imaging we employ high-intensity pulses of light. In fact, when dealing with optically dense clouds as in our experiment, the number of transmitted photons in the low-intensity regime becomes very low, reducing consequently the signal-to-noise ratio. Moreover, to reach the high spatial resolution of our vertical imaging system, it is essential to minimize the atomic motion caused by the recoil from scattered photons during the imaging pulse. To this end, we use short imaging pulses of $4\,\mu$s with an intensity of $I \simeq 3\,I_{sat}$, where $I_{sat} = \frac{\pi}{3}\frac{hc\Gamma}{\lambda^3}$ is the saturation intensity. When the saturation of the atomic transition cannot be neglected, the Lambert-Beer law modifies to [118]:

$$\frac{dI}{dz} = -n(x, y, x)\,\sigma_{eff}\,\frac{1}{1 + \frac{I}{I_{eff}}}\,I, \tag{2.8}$$

where I is the light intensity propagating along the z direction and illuminating the atomic cloud of density n, $\sigma_{eff} = \sigma_0/\alpha$ and $I_{eff} = \beta I_{sat}$ are the effective cross-section and effective saturation intensity, respectively. In fact, the complex multilevel structure of the atomic transition and imperfections in the alignment of the imaging beam polarization with the quantization axis might affect the ideal values of cross-section $\sigma_0 = \frac{3\lambda^2}{2\pi}$ and saturation intensity I_{sat} for a two-level system [119]. The shadow profile of the atomic cloud, that we acquire with absorption imaging, provides a measurement of the optical column density OD, that can be obtained by integrating the previous equation along the z imaging direction:

$$\begin{aligned} \mathrm{OD} = \sigma_{eff}\, n_{2D}(x,y) &= \sigma_{eff} \int_{-\infty}^{+\infty} n(x,y,z) \\ &= -\ln\left(\frac{I_{out}}{I_{in}}\right) + \frac{I_{in} - I_{out}}{I_{eff}}, \end{aligned} \tag{2.9}$$

where I_{in} and I_{out} are the incident and transmitted intensity, respectively. We note that when $I \ll I_{eff}$ the linear term can be neglected and the simple Lambert-Beer law with only the dependency on relative intensities is recovered. The integrated atomic density n_{2D} is thus given by:

$$n_{2D}(x,y) = -\frac{\alpha}{\sigma_0} \ln\left(\frac{I_{out}}{I_{in}}\right) + \frac{\alpha}{\beta}\frac{1}{\sigma_0}\frac{I_{in} - I_{out}}{I_{sat}}. \tag{2.10}$$

To have a reliable measurement of the atomic density, α and β parameters should be calibrated. To do that, we use the technique described in Refs. [104, 118]: we prepare an atomic cloud with a stable number of atoms and we measure its atom number with the reliable low-intensity horizontal imaging. We then image the same cloud with the vertical setup and calibrate the value of α so that the ODs acquired with different light intensities show the same profile. The value of β is instead obtained by constraining the number of atoms measured with the vertical imaging to be the same as measured with the horizontal one.

2.3 Arbitrary optical potentials with DMD

The control over the light intensity spatial profile opens the possibility to sculpt the potential felt by atoms. To this end, an entire class of devices, the Spatial Light Modulators (SLMs), has been developed in recent years. All different kinds of SLMs are composed by arrays of electrically controllable micrometer-sized elements, the optical reflectivity (or transmissivity) of which can be tuned at will. According to the nature of their building blocks we can distinguish between liquid crystal, deformable mirrors and acousto optic SLMs, all able to create both static and dynamical optical potentials. When dealing with static potentials, the refresh rate of the SLM should be considered: to avoid that the array elements get stuck in the displayed position, the device force them to refresh periodically, limiting the effective stillness of a static potential. For applications in atomic physics experiments, the refresh rate has to be greater than the time the optical potential has to be kept on the atomic cloud, to avoid heating of the sample. On the other hand, dynamical potentials can be created by displaying

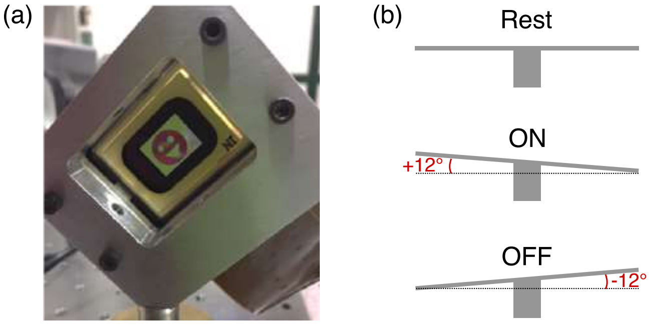

Figure 2.9: The Digital Micromirror Device (DMD). (a) Picture of the DMD mounted on its 45° tilted mount, when displaying a smile image. (b) Sketch of the tilt states of the DMD: when the DMD is off all micromirrors occupy the rest position tilted by 0°, while when a voltage is applied to a mirror it tilts either by +12° or −12°, labeled as ON and OFF state, according to the sign of the voltage.

a sequence of different images on the device. The frame rate of the SLM sets the dynamical potential timescale, that is limited by the switching time of the arrays elements. Deformable mirrors SLMs such as Digital Micromirror Devices (DMDs) are well suited for applications in atomic physics experiments, as they provide both truly static images with a high definition, thanks to the low refresh rate, and a dynamical control on a time scale comparable to the atomic response time, thanks to the high frame rate.

In our experiment we implemented a Vialux V-7000 High-Speed Module DMD, equipped with the Texas Instruments Discovery 4100 0.7" XGA 2xLVDS (DLP7000) chip. The chip is composed by a 1024×768 array of square micromirrors of pitch $13.68\,\mu$m, and it is attached to the 45° tilted mount presented in the picture of Fig. 2.9 (a). The tilt state of each mirror is independently controlled by applying an external voltage to set it into the +12° or −12° state, labeled as ON and OFF respectively, as sketched in Fig. 2.9 (b). When the DMD is off and no external voltage is applied to the chip, all mirrors remain in the rest position of 0° tilting angle. ON and OFF states reflect the lights impinging on the device in different directions, so that the DMD acts as a light mask. In fact, when a binary black-and-white image is loaded on the device, the DMD mirrors are arranged in ON and OFF states following the coding of the image, which is reproduced on the DMD screen, as visible in Fig. 2.9 (a) where a smile picture is loaded on the DMD. The intensity profile of the light reflected in the ON direction has the same shape of the binary image sent to the DMD, namely the shape of a smile for the image of Fig. 2.9 (a). The reflection of the DMD is then projected into the atomic cloud to create a repulsive optical dipole potential, since we illuminate the DMD with blue-detuned light at 532 nm.

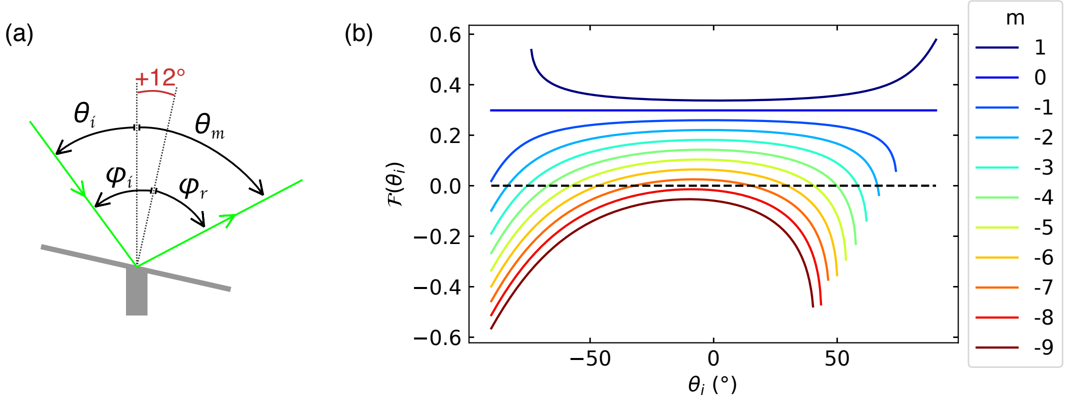

Figure 2.10: Blazing condition for DMD. (a) Sketch of the nomenclature for angles adopted in the text: θ (φ) angles are counted from the normal of the device surface (mirror surface). They are connected by the relation: $\theta = \varphi - 12°$. (b) Blazing condition $\mathcal{F}(\theta_i)$ calculated for different diffraction orders m under our experimental condition of $d = 13.68\,\mu$m and $\lambda = 532$ nm.

Blazing condition

To fully understand the optical behaviour of the DMD, its diffraction properties have to be taken into account. In fact, the DMD micromirror array acts as a diffraction grating that reflects the incident light into several diffraction orders. For the light power in the main order to be optimized, the blazing condition of the grating has to be fulfilled.

To analyze the diffraction behaviour of the DMD, we use the notation of Fig. 2.10 (a): θ angles are taken respect to the normal of the device surface, while φ angles respect to the normal of mirrors surface, differing from the previous ones by 12°. The incident light with angle θ_i is reflected in the direction θ_m for the m order of diffraction, ruled by the grating equation [117]:

$$m\lambda = d\,(\sin\theta_i + \sin\theta_m), \tag{2.11}$$

where λ is the light wavelength and d the grating pitch. The grating is blazed when all mirrors reflect the light in the same diffraction order, namely when $\theta_m = \theta_r$, where $\theta_r = \varphi_r - 12°$ is the direction of the reflection of a single mirror. By inserting this request into the grating equation we obtain the blazing condition:

$$\mathcal{F}(\theta_i) = \arcsin\left(\frac{m\lambda}{d} - \sin\theta_i\right) + \theta_i + 24° = 0. \tag{2.12}$$

In Fig. 2.10 (b) the blazing condition $\mathcal{F}(\theta_i)$ is plotted for the relevant diffraction orders over the range of all possible θ_i, using our experimental conditions of $d = 13.68\,\mu$m and $\lambda = 532$ nm. The blazing condition is fulfilled for m and θ_i such that $\mathcal{F}(\theta_i) = 0$, happening for the orders from -2 to -7 at different incident angles. Among all the possible blazed configurations, the ones with the smaller θ_i have to be preferred, to guarantee a good illumination of the DMD screen and prevent image distortions. In our case, the lowest incident angle that fulfills the blazing condition is $\theta_i = 16°$ for $m = -7$. However, it is possible to use an even smaller θ_i by working in a not perfectly blazed condition. In particular, the $\theta_i = -12°$ configuration offers the advantage of having the diffracted beam collinear with the incident one, that is useful to implement the DMD in a compact optical setup. In fact, the diffracted angle is connected to the incident one by the relation $\theta_m = -\theta_i - 24°$, that for $\theta_i = -12°$ gives $\theta_m = -\theta_i$. For such incident angle no order of diffraction is exactly blazed, but the $m = -8$ one almost fulfills the blazing condition, as $\mathcal{F}(m = -8, \theta_i = -12°) = -0.014$. We verify that under this condition the reflection efficiency of the DMD is of the order of 60%.

2.3.1 Optical setup for DMD projection

To create the DMD-made optical potentials, we image the device screen on the atomic cloud via the microscope objective system already presented, that guarantee a sub-micrometer resolution at 532 nm. In particular, we combine the imaging setup of Fig. 2.8 with the one sketched in Fig. 2.11 (a). The collimator of a large-mode optical fiber produces a collimated Gaussian beam with a large waist of about 0.7 cm, that we use to effectively illuminate the 1 × 1.5 cm screen of the DMD. The beam is sent to the device via a dichroic mirror, the leak of which is measured with a photodiode (PD) and used to stabilize the intensity of the beam with a PID feedback loop. In particular, the PID sets the amplitude of the driving signal of an AOM placed before the input of the optical fiber, regulating thus its output intensity. We work in the collinear configuration of $\theta_i = -12°$ already presented, and recombine incident and reflected beams through a polarizing beam-splitter (PBS), with the polarization set by the $\lambda/2$ and $\lambda/4$ waveplates. The following telescope, composed by the $f_1 = 250$ mm and $f_2 = 100$ mm lenses, set in $f_1 + f_2$ configuration to avoid aberrations in the wavefront, de-magnifies the DMD pattern of a factor 2.52. In the focal plane of the first lens we place an adjustable iris, that acts as a spatial filter to smoothen the discretized DMD image, if required. The DMD projection path is subsequently combined with the imaging one on a large 2" PBS, and focused onto the atomic cloud by the objective system. The DMD image is thus de-magnified by an overall factor 54.99: a single mirror of the DMD has a size of $0.25\,\mu$m in the atomic plane. A flip mirror is placed directly after the first telescope to focus the DMD image onto a Thorlabs CMOS camera. This path is used to check the DMD pattern and to run the feedback routine, that is presented in the next section. We also employ it to calibrate the de-magnification of the first telescope optical system: we load on the DMD an image of 3 dots placed in well known positions and measure their distance on the Thorlabs camera. We extract the de-magnification factor of 2.52 from the ratio between their distance on the DMD screen and the one measured on the camera.

On Fig. 2.11 (b) we show the realization of DMD-made arbitrary optical potentials projected on a quasi-2D atomic cloud. The sample is created by superimposing the high-power $\mathrm{TEM}_{(0,1)}$ potential to the infrared crossed trap at the end of evaporation

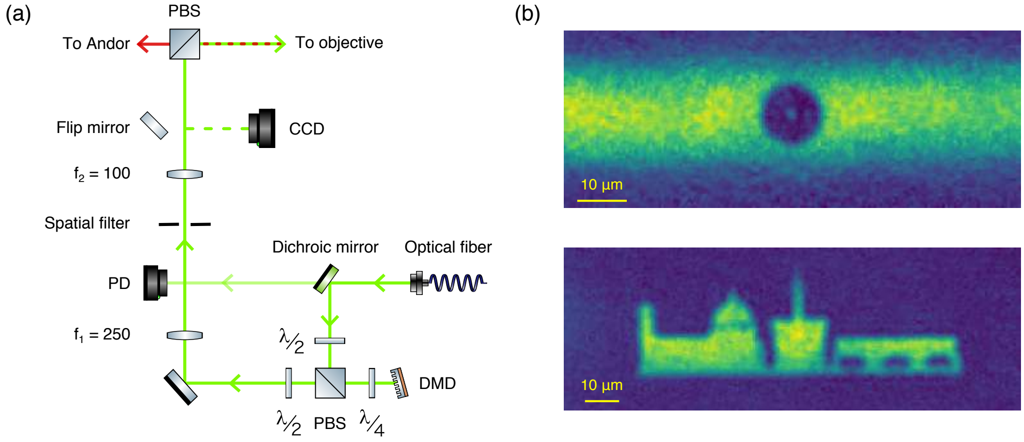

Figure 2.11: DMD pattern projection onto the atomic cloud. (a) Optical setup for DMD projection: the DMD pattern is first de-magnified by a telescope to be then recombined with the imaging beam (in red) on a PBS. A flip mirror allow for focusing the DMD image on a Thorlabs CCD camera after the telescope. (b) Arbitrary optical potentials on a quasi-2D cloud. On top: projection of a donut potential with a $1\,\mu$m hole. On bottom: Florence skyline.

and successively ramping on the DMD potential with the desired projected image. The cloud is squeezed on the z-direction to exploit the full resolution of the microscope objective system. Both images of Fig. 2.11 (b) consist of the sum of 20 single images of the atomic cloud, obtained with the imaging system presented in Sec. 2.2.2. On the top one a donut optical potential is projected onto the cloud. The central hole of the donut has 4 pixel diameter on the DMD screen that corresponds to about $1\,\mu$m on the atom plane. The fact that the hole of the donut is clearly visible means that the resolution of both the imaging system and the DMD projecting one is of the order of $1\,\mu$m. Despite not providing a proper characterization of the resolution of the objective system, such observation give us a higher limit for it. On the bottom image of Fig. 2.11 (b) we exploit the high resolution of our microscope objective system to shape the atomic cloud as Florence skyline: from left to right we can observe the Florence Cathedral with Giotto's Campanile and Brunelleschi's Dome, the town hall of Palazzo Vecchio and Ponte Vecchio bridge.

2.3.2 Controlling the DMD

In order to control the DMD-made optical potentials, the device needs to interface with a software program able to load, change and run a sequence of images. Vialux provides a pre-build controlling program for the DMD, the ALP basic GUI, that supports up to a maximum of 5 images sequence. We use such software only to project static optical potentials, while we developed a new program to produce dynamical ones. Our control software is based on the ALP4lib open source Python module by Sebastien Popoff [120], that allows for loading long sequences of images on the device as well as for setting the timing properties of the sequence display. Both the feedback program and the one for producing dynamical optical potentials presented below employ the ALP4lib to interface with the DMD.

Feedback program

Since the DMD acts as a light mask, the projected optical potentials maintains the Gaussian profile of the incident beam, cut by the device. For confining potentials as the ones used in Fig. 2.11 (b) this is not a problem since the 532 nm light we use is repulsive on lithium atoms. On the other hand, the residual Gaussian profile has to be removed from the pattern once the goal is to move an obstacle, whether a barrier or a dot, along the atom cloud while keeping its intensity constant during the whole process. To do that, we employ the feedback program I developed during my Master Thesis [121], able to create homogeneous pattern of light. The working principle of such routine is the same of a PID feedback loop: it compares a measured image with the target one, and minimizes the error between the two by applying a pixel-by-pixel error correction matrix on the DMD mirror array configuration. In particular, to run the feedback program, we close the spatial filter in between the telescope of Fig. 2.11 (a) to a small diameter of about a half millimeter and focus the DMD projection on the auxiliary CCD camera. The closed iris acts as a low-pass filter with bandwidth of a couple of μm, making the local pixel-by-pixel error correction effective to produce homogeneous profiles over a large area. We run the feedback routine to obtain a rectangular homogeneous profile as large as possible, so to cover the largest atomic cloud area. We then create the image sequence for a moving obstacle by cutting from the homogeneous profile the obstacle shape in the desired position. Such procedure provide us a versatile starting point for the creation of tailored homogeneous obstacle. In particular, we set as target image a black rectangular area of all ON mirrors. Both DMD images and the ones acquired with the CCD are in bitmap extension, so that each pixel takes values in the range $[0, 255]$, where 255 correspond to black (ON) and 0 to white (OFF). The intensity of the final homogeneous pattern is adjusted with the intensity threshold parameter $I_{th} \in [0, 255]$, that rescales the target image into grayscale at the beginning of the feedback routine. The grayscale target image is then binarized with a dithering algoritm that employs the Floyd-Steinberg method [121,122], and sent to the DMD. Images with different I_{th} correspond to a different percentage of ON mirrors in the dithered target image. In each cycle of the feedback loop, the image acquired with the CCD is compared with the grayscale target, and their error matrix is applied to the current DMD image to produce a new one. The loop breaks when the RMS error between target and acquired image is below a threshold, saving both the feedbacked DMD image and its acquisition on the CCD. In Fig. 2.12 (a) we show the x direction profile of a homogeneous 200×500 pixel rectangular area, obtained with the feedback program at different I_{th} and acquired with the CCD. Here, x refers to the atomic plane, being the axial direction of the cigar trap. All the obtained patterns show a good level of homogeneity, despite displaying intensity fluctuations on the scale

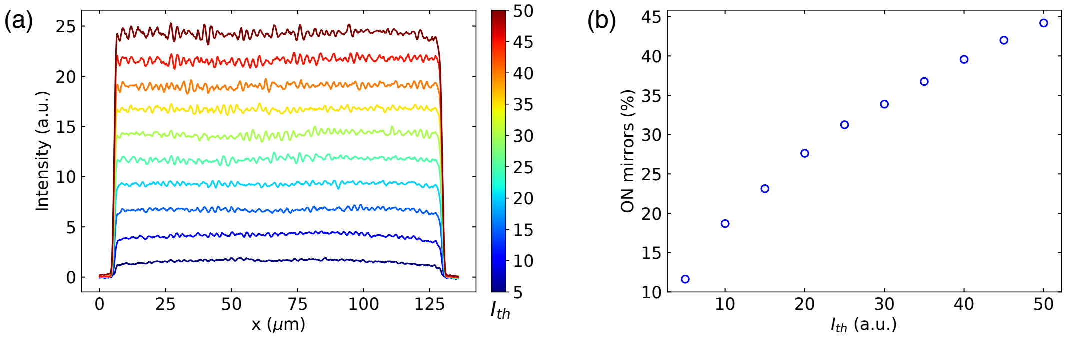

Figure 2.12: Homogeneous pattern creation with the feedback program. (a) x-direction profile of rectangular homogeneous patterns obtained with the feedback routine for different I_{th}. Each line corresponds to acquired image intensity value, averaged over 50 pixel along the y direction. Here, x and y directions refers to the atomic plane, corresponding to the axial and radial one of the cigar trap, respectively. (b) Conversion between the intensity threshold parameter I_{th} used in the feedback routine and the actual percentage of ON mirrors in the feedbacked images. The latter is calculated over a 40×40 pixels central region.

of a few μm on the atomic plane, that is expected not to affect the shape of small caved obstacles. The different intensity level is obtained by tuning the average number of ON mirrors, as reported in Fig. 2.12 (b). Here, the percentage of ON mirrors is calculated over a 40×40 pixel central region of the DMD where the Gaussian profile of the incident beam is expected not to change much. Therefore, the feedback routine allows for the creation of homogeneous profiles with tunable intensity, but more generally it can be used to produce patterns with varying intensity as well, such as gradients or lattices.

Dynamical control

To apply dynamical optical potentials to the atomic cloud, the capability of playing a long sequence of images is required, together with the control over the display timing properties. The first requirement is achieved by employing the ALP4lib module that allows for the loading of arbitrarily long sequence of images. In addition, the sequence display needs to be synchronized with the experimental cycle and thus controllable via the control program. To do that, we set the DMD in `SLAVE` mode and use the trigger input port of its V-7000 Vialux board to trigger the switch between two following images in a pre-loaded sequence via a TTL signal. The timing properties of the sequence display are thus set by the trigger inputs sent to the device via the control program, and are only limited by the intrinsic timing of the device. The time distance between two triggers is called *Picture Time*, measuring the display time of a single picture. The DMD allows for other two timing configurations, `MASTER` and `STEP` mode, a detailed description of which is presented in Appendix A.

To better understand the dynamic behaviour of the DMD, we tested it before implementing the device into the experimental setup. In particular, we play a simple sequence of two images alternating all black (ON) and all white (OFF) images and

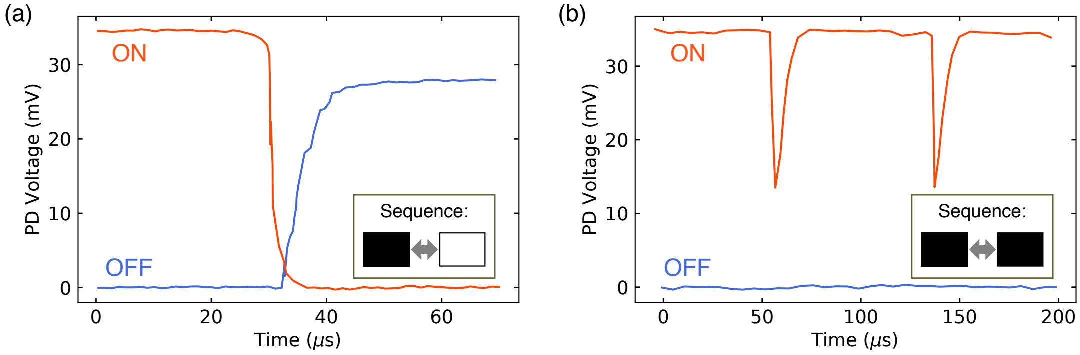

Figure 2.13: Test of the DMD timing properties: the reflected light in the ON (red) and OFF (blue) directions is recorded during the display of a sequence. In (a) the sequence alternates all black (ON) and all white (OFF) images and the signal is zoomed during the switch for the first to the second. In (b) a sequence of only all black (ON) images is displayed with a *Picture Time* of 80 μs.

record the light reflected into the ON and OFF directions with two photodiodes (PDs). Both PD resistors have been chosen to give a time response of the order of 70 ns, fast enough to resolve the changes in the DMD reflected light, expected to happen over timescale of tens of μs. To avoid dark phases, during which all the mirrors are kept in the OFF state, we set the DMD to operate in `UNINTERRUPTED` mode, that allows for the display of only binary image and reduces the minimum value of *Picture Time* to 44 μs. In Fig. 2.13 (a) the ON and OFF signals during the switch from a black to a white image is presented. The switch happens over a timescale of about 10 μs, the time needed for mirrors to swap their tilt state. The behavior of the mirrors during a trigger is highlighted on Fig. 2.13 (b), where we show the PD signals recorded during the display of a sequence of two images alternating always an all black (ON) image. Here, we set a constant *Picture Time* of 80 μs. When a trigger arrives to the DMD, the signal on the ON direction shows a dip, but the OFF one stays constant. Hence, during an image switch all the DMD mirrors goes to the rest position to then tilt to the new state, not caring whether it is different form the previous one or not.

To conclude, dynamical potentials are created by displaying the desired sequence of images on the DMD, which is operated in `SLAVE` mode so that the switch from an image to the following is controlled by TTL trigger signals. By setting the device to work in `UNINTERRUPTED` mode the minimum *Picture Time* is set to be 44 μs, that allows for reaching the maximum frame rate of the device of 22 kHz. The process of switching image takes about 10 μs, during which all mirrors goes to the rest position to then tilt to the new state. Practically, that means that during such 10 μs no light is actually projected into the cloud. The switching time has to be compared to the atom response time $\sim \hbar/\mu$, where μ is the chemical potential of the cloud, to see if the absence of light during the switching time can affect the atom density. For the measurements presented in Chapters 3 and 4, $\hbar/\mu \gtrsim 30\,\mu$s so that the effect of the dark switching time can be neglected.

Chapter 3

A current-biased Josephson junction between fermionic superfluids

Experiments performed so far with Josephson junctions of fermionic superfluids never enabled a direct measurement of the critical current I_c, which is hidden into the plasma frequency of oscillations in a voltage-biased junction. Similarly to superconducting Josephson junctions (SJJs), the critical current can be nevertheless directly measured from the complete current-chemical potential $I - \Delta\mu$ characteristic of the junction, acquired by monitoring the junction response after the injection of a controlled external current. In this chapter we present a novel protocol to implement a current-biased atomic Josephson junction, which allows for the direct measurement of I_c of fermionic superfluids throughout the BEC-BCS crossover. The $I-\Delta\mu$ characteristic shows a clear regime of dc Josephson, where a dissipationless supercurrent flow through the junction without developing any chemical potential difference. We corroborate the observation of dc Josephson effect by measuring for the first time the current-phase relation of an atomic junction, which is found to be sinusoidal for sufficiently strong barriers. From the $I - \Delta\mu$ characteristic we obtain a model-free determination of the critical current, the behavior of which is explored for different barrier parameters throughout the BEC-BCS crossover. From the comparison between the measured I_c and a semi-analytic theory model, we can extract the condensed fraction of fermionic superfluids in the BEC-BCS crossover. The results discussed in the following have been published in:

- W. J. Kwon, G. Del Pace, R. Panza, M. Inguscio, W. Zwerger, M. Zaccanti, F. Scazza and G. Roati, *Strongly correlated superfluid order parameters from dc Josephson supercurrents*, Science, **369**, 6499 (2020).

The chapter is organized as it follows. In Sec. 3.1 we describe the experimental realization of a current-biased atomic junction, focusing on the creation and characterization of the barrier and illustrating the DMD-based barrier translation protocol. Sec. 3.2 reports on the acquisition of the current-chemical potential characteristic of the junction and the following observation of dc Josephson effect, characterized by a sinusoidal-current phase relation, as we measure in the strong-barrier limit. In Sec. 3.3 we present the critical current characterization throughout the BEC-BCS crossover

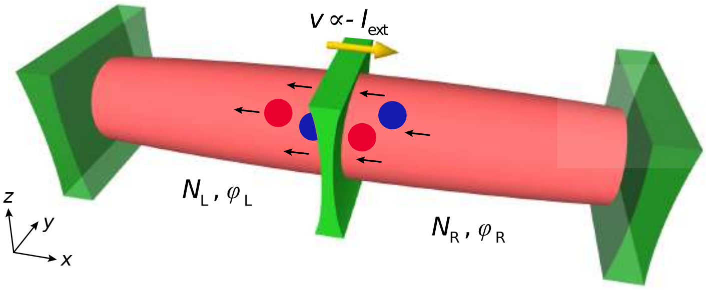

Figure 3.1: Sketch of the experimental realization of an atomic current-biased Josephson junction. Atoms are trapped in a hybrid optical dipole trap: on top of the harmonic crossed ODT we project a repulsive DMD-generated potential consisting in a central thin barrier plus two axial endcaps. The barrier is successively set into motion with constant velocity to inject an oppositely oriented current through the junction.

and the comparison with the analytic theory model, that enables us to extract the condensed fraction of fermionic superfluids. Finally, Sec. 3.4 introduces the discussion on the normal conductance of the junction, that accounts for the resistive behavior above I_c, and will be further developed in Chapter 4.

3.1 Experimental realization of a current-biased Josephson junction

We implement an atomic current-biased junction by confining strongly correlated fermionic superfluids in the hybrid optical dipole trap sketched in Fig. 3.1. In particular, we produce a superfluid sample of $N \simeq 1.3 \times 10^5$ atoms per spin state at $T/T_F = 0.06(2)$, confined in a harmonic trap of frequencies $\omega_{x,y,z} = 2\pi \times (12, 165, 140)$ Hz, and add on top of it a DMD-made repulsive potential consisting of a thin barrier and two side endcaps. The barrier is thin enough to allow the wavefunctions of the two reservoirs to overlap below it, so that coherent transport can occur. On the other hand, the endcaps consist of thick repulsive walls of potential that restrict the system to a smaller central region of the cloud, increasing the shot-to-shot stability while cutting out the most dilute and highest entropy sides of the cloud. To inject a controlled external current into the atomic junction, the barrier is translated in the axial direction of the cloud with a constant and tunable velocity, as proposed in Ref. [97]. Particles tunneling through the barrier in the opposite direction of its motion give rise to an effective injected current into the junction. At the low temperature we employ for all the measurements presented in this chapter, the sample is composed by paired fermions at all the interaction strengths explored, bosonic pairs being the carriers of the current in our junction. Therefore, all transport quantities, such as current and chemical potential, are here intended as pair quantities, but to ease the notation throughout this chapter we omit the subscript $_B$, adopted so far to individuate them.

In this section, we describe in detail the creation of the DMD pattern to produce the junction and the characterization of the properties of the barrier, namely its width and height. In particular, two different methods have been implemented to calibrate the barrier height, relying on the density equation of state of a weakly interacting BEC and on a phase imprinting technique, respectively. They give consistent calibrations of the barrier height and are presented further below. Finally, in Sec. 3.1.2 we discuss the barrier translation protocol exploited to implement the current-biased atomic junction.

3.1.1 Barrier creation and characterization

To translate the barrier through the atomic sample, we create a sequence of DMD-images, each one consisting of a barrier of fixed size displaced by 1 DMD mirror from the previous frame. Each barrier is cut from a homogeneous pattern of light, obtained with the feedback program presented in Sec. 2.3, with I_{th} set to give about 45% of ON mirrors on the peak of the Gaussian beam illuminating the device. In particular, we cut a rectangular area from the homogeneous profile, the smaller dimension of which can be adjusted to optimize the barrier width on atoms. On top of each image of the sequence, we add two 100 mirrors thick rectangular side regions to produce the endcaps. They are placed at 550 mirrors distance one from the other, that identify an about $140\,\mu$m long central region on the atomic cloud to form the junction.

Barrier width characterization

To smoothen the rectangular axial profile of the cut barrier, we close the spatial filter in the DMD setup (see Fig. 2.11 (a)), that eliminates the high frequencies of the image. Under our working conditions, the spatial filter represents the most limiting aperture of the DMD projecting optical system, which we verified by observing that the whole filtered pattern is well collected into the tube lens and objective apertures. Therefore, the image of the DMD pattern we acquire with the auxiliary camera on the secondary optical path of the setup provides a reliable approximation of the light pattern projected on the atomic cloud. We characterize the barrier profile by acquiring an image of it with the camera and then measuring its width. In Fig. 3.2 (a) the axial profiles of barriers of $4-10$ mirrors thickness on the DMD screen are plotted in different colors (symbols), together with a Gaussian fit of each (solid lines) to provide a measurement of the barrier width, defined as the Gaussian $1/e^2$ radius. The DMD allows for the fine tuning of the barrier width, from a minimum of $0.63\,\mu$m for the 4 mirrors barrier, to a maximum of $0.95\,\mu$m for the 6 mirrors one, while keeping the axial profile well approximated by a Gaussian. For larger barriers, namely from 8 mirrors on, the axial profile is rather flat-top, and the Gaussian approximation starts to fail. For the measurements presented further below in this chapter and in the next one, we mainly use the 6 mirrors barrier, unless otherwise specified, the Gaussian fit of which is compared with an Eckart one in Fig. 3.2 (b)-(c). The latter is performed by assuming the Eckart profile $V(x) = A/\cosh^2(x/d)$ and constraining the barrier dimension to $d = 0.6\,w$, where w is its Gaussian width. Both the Gaussian and the Eckart function provide a reasonable approximation of the axial profile of the barrier, with a value of χ^2

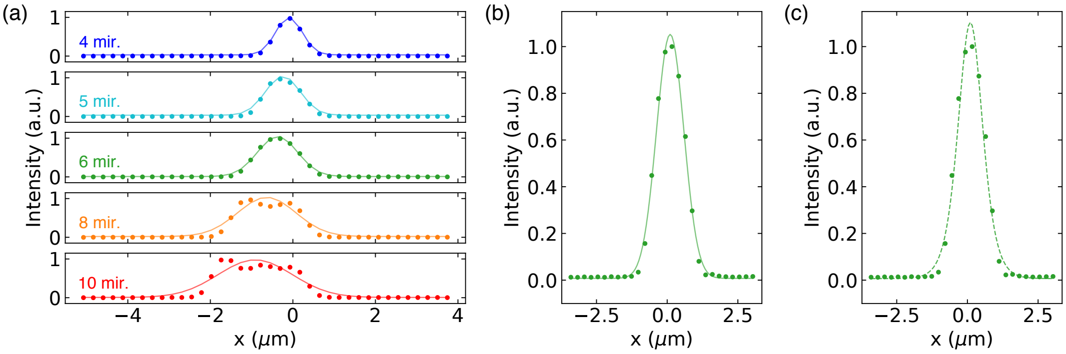

Figure 3.2: Barrier width characterization. (a) Comparison among the axial profiles of $4-10$ mirrors large barriers and their fit with a Gaussian function. The x coordinate indicates the axial direction on the atomic plane (see Fig. 3.1). The extracted Gaussian widths are 0.63, 0.82, 0.95, 1.38 and 1.8 μm for the 4, 5, 6, 8 and 10 mirrors barriers respectively. (b)-(c) Comparison between a Gaussian (solid line in (b)) and an Eckart (dashed line in (c)) fit of the 6 mirrors barrier. The Eckart fit is performed by constraining the dimension of the barrier to be $d = 0.6\,w$, where $w = 0.95\,\mu$m is its Gaussian width. The χ^2 is 0.14 and 0.23 for the Gaussian and the Eckart fit, respectively.

of the fits of 0.14 and 0.23 respectively. Here, we defined $\chi^2 = \sum_i (y_i - f(x_i))^2/f(x_i)$, where y_i are the measured values in correspondence of x_i, and $f(x_i)$ the functional model assumed for the fit. Despite providing a higher χ^2, the Eckart fit with $d = 0.6\,w$ is able to well represent the axial profile of the barrier, justifying the Eckart barrier approximation adopted in Sec. 3.3.1 to analytically calculate the tunneling probability amplitude. Whatever the fit function involved to describe it, the DMD-made repulsive barrier of our atomic junction has an axial dimension comparable with the healing length of the superfluids, while it is homogeneous in the y direction.

Barrier height calibration with BEC density equation of state

To characterize the atomic junction behavior, the barrier height V_0 should be precisely known. As a first method to calibrate the barrier height, we found out the value of V_0 that matches the chemical potential μ of a weakly interacting BEC, which can be accurately calculated knowing the system parameter. Such calibration method is analogous to the one used to measure the density equation of state of a two-dimensional homogeneous Fermi gas exploited in Ref. [123]. We prepare a molecular BEC with $1/k_F a \sim 9$ and about 60% condensed fraction, the interactions of which are weak enough to be well described by the standard weakly interacting BEC model, and we impose on the cloud in the crossed ODT a DMD square potential caved from the same homogenous profile we use for producing the barriers. In particular, we create a 30×30 mirrors pattern on the DMD screen, that correspond to a $7.5 \times 7.5\,\mu\text{m}^2$ region of the atomic plane, placed in the center of the cloud. The effect of the repulsive square potential on the atomic density is presented in Fig. 3.3 (a): as we increase the power of the beam impinging on the DMD, the atom density gets depleted in correspondence of

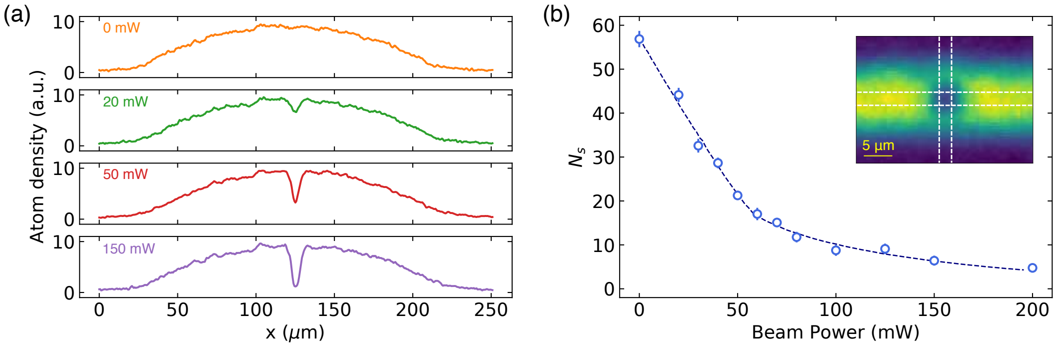

Figure 3.3: Barrier height calibration via density equation of state of a weakly interacting molecular BEC. (a) Density depletion of the atomic cloud when a $7.5 \times 7.5\,\mu\text{m}^2$ homogeneous square potential of increasing height is applied. The reported powers refers to the light impinging on the DMD screen. (b) Measured number of atoms N_s in the square potential region (blue circles), as a function of the beam power and relative fit to extract the calibration parameter α (dashed line). Inset: image of the molecular BEC when the square potential is applied with 70 mW power. N_s is obtained by integrating the density profile over the area delimited by the white dashed lines in the inset.

the square potential. By measuring the local atom number N_s inside the square region as a function of the beam power P, as reported in Fig. 3.3 (b), we can extract the DMD illumination power for which $V_0 = \alpha P = \mu$, where α is the calibration parameter. In particular, N_s is obtained by integrating the atom density inside the region delimited by the white dashed lines of the inset of Fig. 3.3 (b), and its trend can be fitted with a model based on the equation of state to extract α. In fact, N_s can be calculated from the density $n(\mathbf{r}, \mu, T)$ as:

$$N_s = \int_{\mathcal{V}} n(\mathbf{r}, \mu - V_0, T)\, d^3\mathbf{r}, \tag{3.1}$$

where the volume $\mathcal{V}$ extends over the potential square region in the $x - y$ plane and infinitely in the z direction. For a partially condensed BEC, n is given by the sum of the condensed density n_0 and that of the thermal cloud n_T. For a BEC confined in an harmonic trap of potential V_h, the condensed and thermal densities under the Thomas-Fermi approximation are given by [124]:

$$n_0(\mathbf{r}, \mu, T) = \frac{\mu - V_h}{g} \tag{3.2}$$

$$n_T(\mathbf{r}, \mu, T) = \frac{1}{\lambda_{dB}^3} g_{3/2}\left(e^{-|\mu - V_h|/k_B T}\right) \tag{3.3}$$

where $g = \frac{4\pi\hbar^2 a_B}{m}$ with $a_B = 0.6\,a$ is the dimer-dimer scattering length, $\lambda_{dB} = \sqrt{\frac{2\pi\hbar^2}{k_B T}}$ is the de Broglie wavelength and $g_{3/2}$ is the Bose function defined as $g_\alpha(z) = \sum_{i=1}^{\infty} z^i / i^\alpha$. Under the same approximations, the pair chemical potential is calculated as:

$$\mu = \frac{\hbar\bar{\omega}}{2}\left(\frac{15 N a_B}{a_h}\right)^{2/5}\left(\frac{N_0}{N}\right)^{2/5}, \tag{3.4}$$

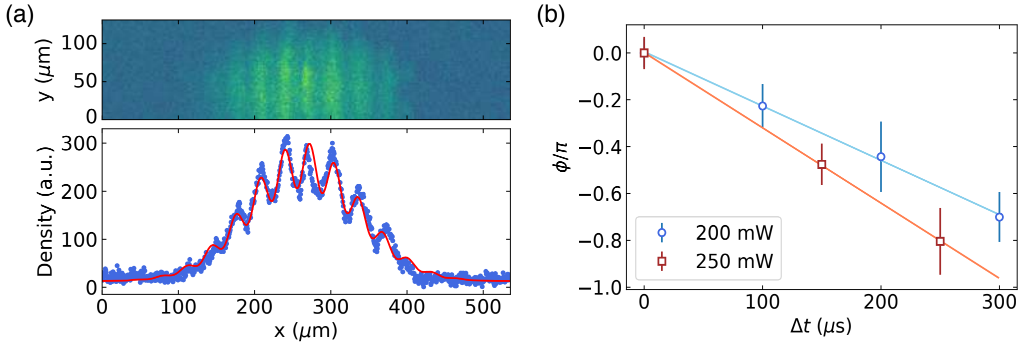

Figure 3.4: Barrier height calibration via a phase imprinting technique. (a) Interference pattern arising after 9 ms time-of-flight expansion and its integrated profile. Fringes are fitted with a Gaussian function modulated with a cosine to extract the relative phase between the two reservoirs. (b) Measured phase as a function of the imprinting time Δt for different DMD-illumation powers.

where $\bar{\omega} = (\omega_x \omega_y \omega_z)^{1/3}$ is the trap frequencies geometric mean, $a_h = \sqrt{\hbar/m\bar{\omega}}$ is the harmonic oscillator length and N_0/N the condensed fraction of the molecular BEC. By combining the previous equations for n_0 and n_T and calculating the chemical potential, we obtain the fit function reported as dashed blue line in Fig. 3.3 (b), setting α as the only fit parameter.

Barrier height calibration with phase imprinting

To further confirm the previous calibration of the barrier height, we implement an alternative method, that employs a phase imprinting technique on a molecular BEC. We shine a homogeneous pattern of light on the cloud for a short time to address only the phase of the condensate, and not its density. In fact, when the interaction time between the atomic sample and an optical potential $U(\mathbf{r}, t)$ is shorter than $\hbar/\mu$, the time evolution of the condensate wavefunction, described by the Gross-Pitaevskii equation in the weakly interacting limit, reduces to [125]:

$$\psi(\mathbf{r}, t) = e^{-i\,t\,U(\mathbf{r},t)/\hbar}\,\psi(\mathbf{r}, 0). \tag{3.5}$$

The phase of a condensate can be thus manipulated by shining for an imprinting time $\Delta t < \hbar/\mu$ a constant and homogeneous pattern of light to produce a potential $U(\mathbf{r}, t) = U_0$. In particular, the acquired phase during the imprinting time $\phi = U_0 \times \Delta t$ is directly proportional to the potential height and can be used to calibrate it. To do that, we prepare a molecular BEC at $1/k_F a \simeq 4.2$ for which $\hbar/\mu \simeq 800\,\mu$s, successively divided into two reservoirs by a thin optical barrier of height $V_0 > \mu$. The homogeneous optical potential is abruptly turned on on only one reservoir by switching the DMD image to a composition of the barrier and a feedbacked homogeneous profile on one of its sides. After a tunable imprinting time Δt, the DMD image is switched back to the simple barrier, and then all the optical potentials are switched off to let the cloud freely expand. From the the interference pattern arising after a 9 ms time of flight, as

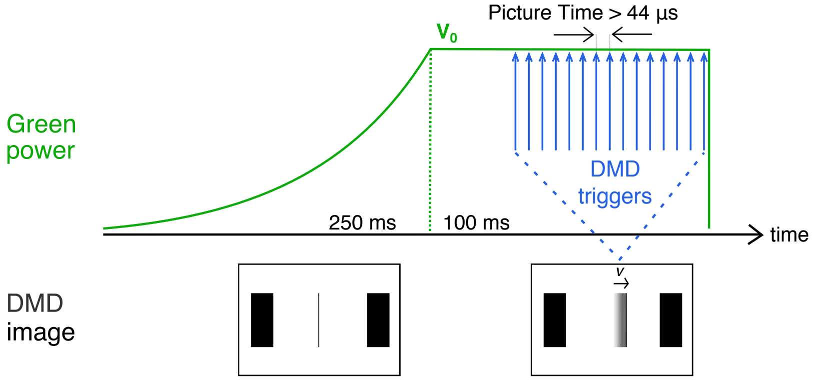

Figure 3.5: Sketch of the barrier translation protocol. In 250 ms we adiabatically ramp up the green beam, while the DMD is displaying the first image of the sequence with the barrier centered inside the 140 μm region delimited by the endcaps. When the barrier has reached the desired height V_0, it is set into motion by playing on the DMD a sequence of images with the barrier displaced by one DMD mirror respect to the previous frame. The switch between each picture and the following is controlled with a sequence of triggers equally spaced by the *Picture Time*, that sets the velocity of the barrier.

the one reported in Fig. 3.4 (a), we measure the imprinted phase by fitting the density distribution with a two-dimensional Gaussian function modulated by a cosine:

$$n(x, y) = A\, e^{-x^2/\sigma_x^2 - y^2/\sigma_y^2}\, (1 + B\cos(kx + \phi))\,. \tag{3.6}$$

In Fig. 3.4 (b) we report the measured imprinted phase for several imprinting times in the regime of $\Delta t < \hbar/\mu$ and for two different powers of the impinging beam on the DMD. For each dataset, the imprinted phase shows a linear trend with the imprinting time, in agreement with the expected behavior. We extract the calibration for the optical potential U_0 from a linear fit of the two datasets, which is found in agreement with that obtained with the method previously presented. We note that with both methods we calibrate the barrier height V_0 experienced by a bosonic pair of atoms, as both employs a molecular BEC. Such value of V_0 is related to the barrier height $V_{0,F}$ felt by a single fermions simply by $V_0 = 2V_{0,F}$, given that the polarizability of one pair is twice that of a single atom.

3.1.2 Barrier translation protocol

To inject a current inside the atomic junction, we set the barrier into motion by dynamically shaping the DMD optical potential. For this purpose, we create a sequence of images, each one showing the barrier shifted by one DMD mirror on the axial direction respect to the previous frame, and play it on the DMD. In particular, we employ the protocol sketched in Fig. 3.5: the junction is created by ramping up in 250 ms the power of the green beam impinging on the DMD, while the first image of the sequence is displayed on the device screen, showing the barrier centered on the 140 μm region delimited by the endcaps. The barrier potential creates two identical reservoirs with populations N_L and N_R for the left and right side, respectively. The position of the infrared crossed trap is precisely adjusted to give an initial relative population imbalance $z = (N_L - N_R)/N \simeq 0$, where $N = N_L + N_R \simeq 1.3 \times 10^5$ is the total pair number inside the junction. In particular, we tune the amplitude modulation offset of the IPG beam to move the crossed trap in the x direction until the previous condition is satisfied. In such balanced configuration, the initial chemical potential difference across the junction, defined as $\Delta\mu = \mu_L - \mu_R$ where μ is the pair chemical potential, is zero as well. Successively, when the barrier potential has reached the target height V_0, a series of triggers is sent to the DMD to play the rest of the sequence. In particular, we employ a 40 images long sequence, so that the total displacement of the barrier is $\delta x = 10\,\mu$m on the atomic cloud. The time interval between two triggers, the *Picture Time* t_P, is tunable and kept constant during the sequence display, yielding a constant velocity $v = 0.25/t_P$ mm/s, where t_P is measured in ms. The motion of the barrier effectively induces a pair current flowing in the opposite direction. The injected external current I_{ext} is calculated as the product of the number of pairs tunneling the barrier $|\bar{z}|\,\frac{N}{2}$, times the tunneling rate $v/\delta x$. Namely:

$$I_{\text{ext}} = -|\bar{z}|\,\frac{N}{2}\,\frac{v}{\delta x}, \tag{3.7}$$

where $\bar{z} = \pm 0.15$ is the equilibrium imbalance, measured with the barrier ramped on the final position of the movement $x_0 = \pm\delta x$. To tune the external injected current, we change the *Picture Time* to move the barrier with different velocities in the range between 0.1 to 2 mm/s. As already discussed in Sec. 2.3.2, the minimum value allowed for t_P is $44\,\mu$s, that sets the highest barrier velocity producible with the DMD to 5.6 mm/s. This constraint does not anyway represent a limit for our experimental investigation, as all the measured critical currents are found to be below 2 mm/s. On the contrary, we are limited on the lowest barrier velocity applicable in our junction: since the barrier displacement is constant, lower velocities imply longer times in performing the translation. For barrier velocities smaller than 0.01 mm/s, the *Picture Time* is so long ($t_P > 2.5$ ms) that atom losses due to the finite lifetime of our sample become non-negligible during the total barrier displacement time, as the lifetime on the BEC side of the resonance is of the order of hundreds of ms.

At the end of the barrier movement, we characterize the junction behavior by imaging the atomic density profile along the vertical direction. In particular, we use *in situ* imaging to extract the population imbalance z, while we let the cloud to expand for a time of flight of 18 ms to measure the relative phase ϕ between the two reservoirs. From the measured population imbalance we calculate the chemical potential difference developed across the junction as:

$$\Delta\mu = (z - \bar{z})\,E_c\,\frac{N}{2}, \tag{3.8}$$

where $E_c = 2\partial\mu_L/\partial N_L$ is the charging energy of the junction, calculated with $N_L = N/2$. We note that, by using the described procedure, the barrier velocity is sharply turned on to the desired value v. It is also possible to introduce an effective initial acceleration, that increases the velocity smoothly to the desired value, by adjusting the time spacing between the initial triggers. We have verified that, whether the velocity is sharply or smoothly turned on, the behavior of the junction is the same within our experimental resolution. Therefore, we employ the equidistant-trigger protocol to keep the translation time as short as possible. This prevents the contribution of incoherent pair transport across the barrier, that reduces the contrast of the measurement, to play a relevant role during the barrier movement.

3.2 Observation of the dc Josephson effect

The implementation of a current-biased atomic junction allows us to measure the whole current-chemical potential characteristic, distinguishing between the dc Josephson regime of $|I_{\text{ext}}| < I_c$ and the resistive branch at $\Delta\mu \neq 0$ for higher injected current. As discussed in Chapter 1, the dc Josephson effect is characterized by a dissipationless current $I_s(\phi)$ flowing across the junction without developing any chemical potential difference, namely keeping $\Delta\mu = 0$. Such current depends solely on the relative phase between the two reservoirs ϕ, and in the tunneling limit of strong barrier, i.e. low transmission, admits a sinusoidal current-phase relation: $I_s = I_c \sin(\phi)$, where I_c is the critical current. We observe the dc Josephson effect by monitoring the developed chemical potential difference across the junction after the injection of a controlled current I_{ext}, obtaining so the complete current-voltage characteristic of the atomic junction. As discussed in the following, the $I - \Delta\mu$ curve presents a plateau at $\Delta\mu \simeq 0$ for small currents, signaling the dc Josephson effect, as further confirmed by the observation of a sinusoidal current-phase relation under the same experimental conditions.

3.2.1 Measurement of the current-voltage characteristic

To obtain a complete current-voltage characteristic, we monitor the developed imbalance in the junction after the barrier translation. In particular, we measure z by integrating the density profiles of the two reservoirs, acquired by *in situ* absorption imaging. As reported in Fig. 3.6 for a molecular BEC (mBEC), the density profile of the compressed reservoir (right one in the figure) changes dramatically when increasing the velocity of the barrier above a critical value v_c. In fact, when $v < v_c$, as for Fig. 3.6 (a), the left and right density profiles are almost homogeneous in the axial direction, as all the interested pairs have coherently tunneled the barrier during its motion without developing any chemical potential difference. On the other hand, when $v > v_c$ as for Fig. 3.6 (b), the right reservoir shows a higher density than the left one, signaling the establishment of a non-zero chemical potential difference. By repeating the measurement for different barrier velocities, we obtain the complete current-voltage characteristic of Fig. 3.7. In particular, I_{ext} and $\Delta\mu$ are calculated from the set velocity and the measured z using Eq. (3.7) and (3.8), respectively. The obtained $I - \Delta\mu$ curve closely resembles the typical current-voltage characteristics of SJJs in the deep

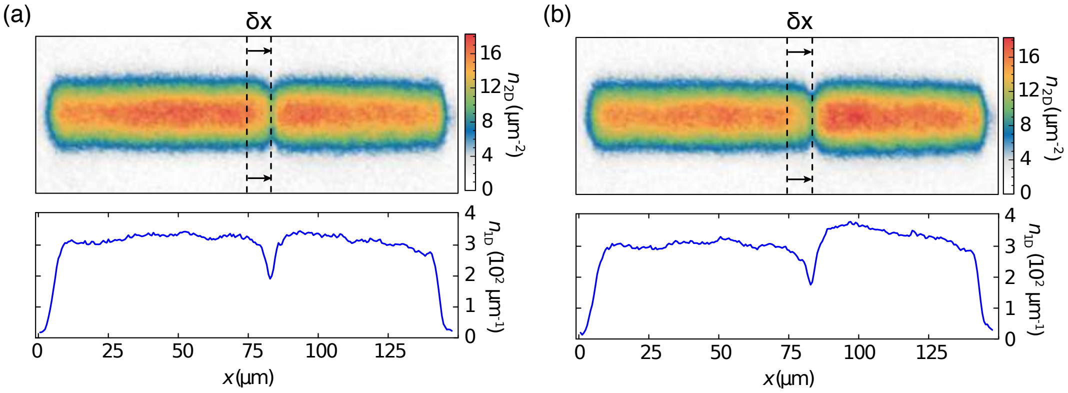

Figure 3.6: Density profile of the atomic junction acquired with *in situ* imaging immediately after the end of the barrier translation. In (a) $v < v_c$ and the density of the two reservoirs is observed to be the same, signaling that no chemical potential difference has developed during the movement. Conversely, when $v > v_c$ (b), the compressed reservoir shows an increased density respect to the other, indicating the establishment of a $\Delta\mu \neq 0$.

BCS regime [90], presenting a plateau at $\Delta\mu \simeq 0$ for $|I_{\text{ext}}| < I_c$, as expected for the dc Josephson effect. For higher injected currents instead, $|I_{\text{ext}}| > I_c$, the dissipative behavior takes over and a $\Delta\mu \neq 0$ develops across the junction. Data are fitted by employing the RCSJ-circuit model described in the next paragraph, to extract the critical current I_c and the normal conductance G of the junction.

The developed $\Delta\mu \neq 0$ in the resistive branch of the characteristic triggers an ac dynamic of the imbalance, similar to that already observed in our system in Ref.

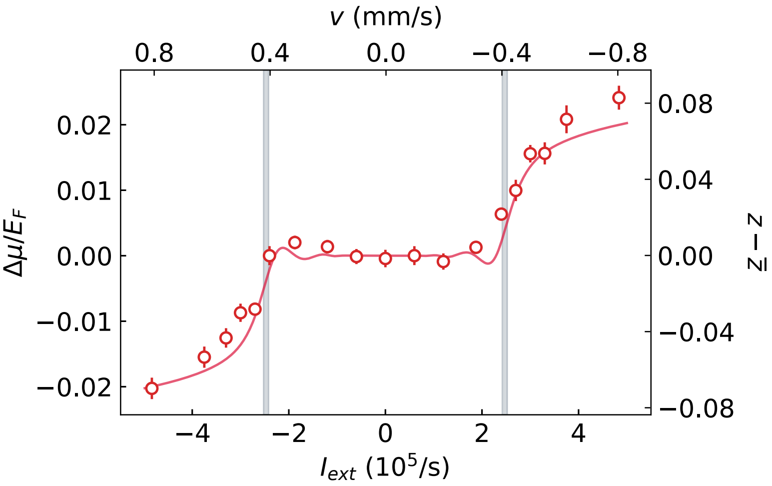

Figure 3.7: Complete current-voltage characteristic of a molecular BEC junction at $1/k_F a \simeq 4.2$ and barrier height $V_0 \simeq 0.6\, E_F = 1.8\, \mu$. Barrier velocity (relative imbalance) is translated into injected current (chemical potential difference) by means of Eq. (3.7) (Eq. (3.8)). The solid line denotes the RCSJ-circuit model fit, whose estimation of I_c standard confidence interval is reported as shaded vertical lines.

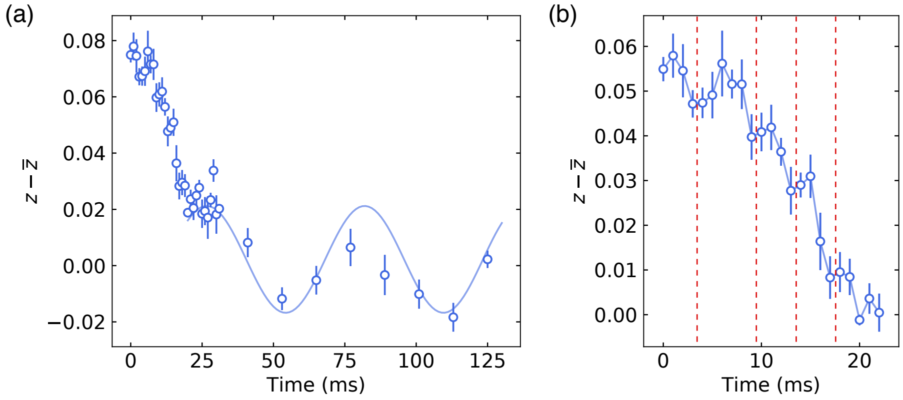

Figure 3.8: Post-translation dynamics in the resistive branch of a mBEC junction at $1/k_Fa \simeq 4.2$. The initial imbalance is created by moving a $0.63\,\mu$m-wide barrier with $V_0/\mu \simeq 3.3$ at a velocity $v \simeq 1.0$ mm/s, above the critical one. (a) The relative imbalance exhibits a decay towards $z - \bar{z} \simeq 0.02$ to subsequently perform plasma oscillations at frequency of 18.1(8) Hz, as obtained from a sinusoidal fit (blue solid line). (b) Zoom of the initial dynamics of (a). A fast modulation features the imbalance decay, suggesting the occurrence of several phase slips. Red dashed lines mark visible minima in the otherwise monotonic decay.

[126]. As reported in Fig. 3.8 for a mBEC, the initial imbalance is observed to decay down to a value of $z - \bar{z} \simeq 0.02$ and then it performs plasma oscillations around the equilibrium value of imbalance. The plasma frequency is measured to be 18.1(8) Hz, higher than the axial trap frequency because of the endcaps. Consistently with our previous results [126], dissipation dominates the ac Josephson dynamics with high initial imbalance. As illustrated by Fig. 3.8 (b), the increased stability of the system guaranteed by the endcaps allows for the observation of a modulation on top of the initial decay of the imbalance, never observed before. The presence of several minima is a signature of phase-slippage processes, that are expected to be the main dissipation mechanism in our system [126, 127]. In fact, when the initial population imbalance exceeds a critical value, vortex rings are generated in correspondence of the barrier, to successively enter the superfluid bulk inducing dissipation in the junction.

3.2.2 RCSJ-circuit model

To quantitatively describe the observed current-voltage characteristic, we employ the resistively and capacitively shunted junction (RCSJ) model, that is largely adopted for SJJs [80, 87]. We parallel our atomic current-biased junction with the equivalent circuit sketched in Fig. 3.9 (a), composed by a Josephson weak link with a current-phase relation $I_s = I_c \sin(\phi)$, a shunt resistance R and a capacitance C. The resistance accounts for the dissipative branch of the characteristic, without affecting the dc regime, while C is fixed by the charging energy as $C = 1/E_c$. The circuit dynamics is described by the Josephson equations (1.42) and (1.43), added by the resistive and capacitive

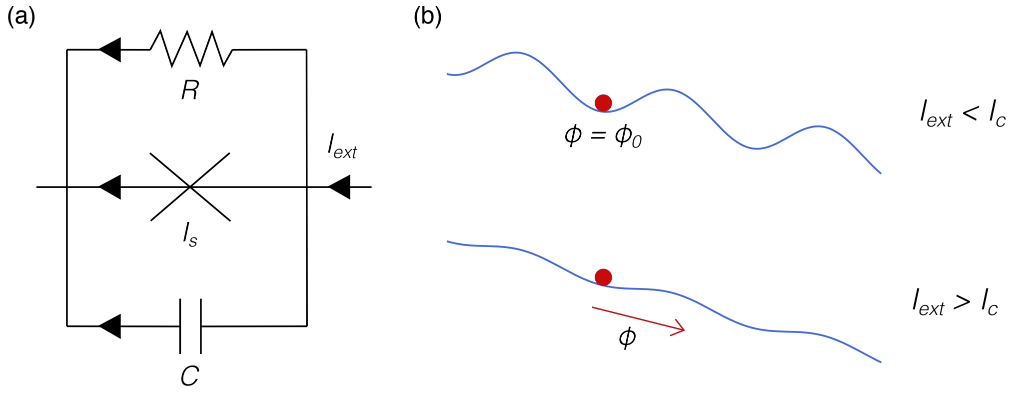

Figure 3.9: RCSJ-circuit model for quantitatively describing the atomic current-biased junction behavior. (a) Sketch of the RCSJ circuit: the ×-shaped element represents the Josephson junction, shunted on a resistance R and a capacitance C. (b) Washboard potential analogy of the RCSJ model. For $I_{\text{ext}} < I_c$ the phase is trapped in one of the minima of the potential and $\Delta\mu = 0$, as $\dot{\phi} = 0$. When $I_{\text{ext}} > I_c$ the system enters in the running phase regime: the washboard potential does not allow minima anymore and the phase increasing develops a non-zero chemical potential difference across the junction.

terms [87, 97]:

$$I_{\text{ext}} = I_c \sin\phi + G\Delta\mu + C\Delta\dot{\mu}, \tag{3.9}$$

$$\hbar\dot{\phi} = \Delta\mu, \tag{3.10}$$

where $G = 1/R$ is the conductance of the junction. By accounting Eq. (3.8) for the chemical potential, the first equation gets:

$$I_{\text{ext}} = I_c \sin\phi + G\Delta\mu + \frac{N}{2}\left(\dot{z} - \dot{\bar{z}}\right). \tag{3.11}$$

In fact, as the barrier translate, not only the imbalance z varies, but also its equilibrium value $\bar{z}$, that depends on the instantaneous position of the barrier. In particular, we assume $\bar{z}(t) = |\bar{z}_f| v\, t/\delta x$, where $\bar{z}_f = \pm 0.15$ is the equilibrium imbalance at time $t_f = \delta x/v$ when the barrier has completed the movement, that is otherwise always referred as $\bar{z}$ for simplicity. Such expression for $\bar{z}(t)$ approximate the axial region swept by the barrier to be homogeneous, which is reasonable considering the small barrier displacement employed. Therefore, by involving the previous time evolution of $\bar{z}$ and Eq. (3.7) for I_{ext}, the previous equation can be recast as:

$$\frac{N}{2}\dot{z} = -I_c \sin\phi - G\Delta\mu. \tag{3.12}$$

The experimental $I - \Delta\mu$ curves are fitted by numerically solving Eqs. (3.12) and (3.10), keeping only I_c and G as free parameter. The charging energy E_c is instead calculated by employing the self-consistent numerical results for crossover superfluids in Ref. [41] within the local density approximation. As illustrated in Fig. 3.7, the RCSJ model excellently captures the experimental $I - \Delta\mu$ characteristic. In the model we assume a purely sinusoidal current-phase relation, not considering higher order terms, which anyway does not affect the extracted value of I_c, that is found to be negligibly sensitive to E_c as well. We note that experimentally the two sides of the characteristic at $v \gtrless 0$ are measured separately. We perform on both an independent fit to extract the exact offset between each other and then use such information to attach them properly. The final values of I_c and G are obtained by fitting the complete characteristic as reported in Fig. 3.7.

To have an intuitive insight of the RCSJ circuit dynamics, the Josephson equations can be combined to give a second order differential equation for the phase, namely:

$$\frac{1}{\omega_p^2}\ddot{\phi} = \frac{I_{\text{ext}}}{I_c} - \sin\phi - \frac{1}{\omega_p}\sqrt{\frac{1}{\beta_c}}\dot{\phi}, \tag{3.13}$$

where we have introduced the plasma frequency $\omega_p = \sqrt{E_C E_J}/\hbar = \sqrt{I_c/(\hbar C)}$, and the Stewart-McCumber parameter $\beta_c = I_c C/(\hbar G^2) = Q^2$, where Q is the quality factor of the junction [87]. The Stewart-McCumber parameter determines whether the oscillatory evolution of the phase is underdamped, for $\beta_c \gg 1$, or overdamped, for $\beta_c \ll 1$, leading to a hysteretic or nonhysteretic $I - \Delta\mu$ characteristic, respectively. The previous expression can be interpreted as the equation of motion of a particle of mass $1/\omega_p^2$ subject to a viscous drag force $-1/\omega_p\sqrt{1/\beta_c}\,\dot{\phi}$ in the effective potential:

$$U(\phi) = 1 - \frac{I_{\text{ext}}}{I_c} - \cos\phi. \tag{3.14}$$

This is the washboard potential illustrated in Fig. 3.9 (b) in the two regimes of current. When $I_{\text{ext}} < I_c$, the potential presents several minima that the phase can stably occupy, and the current flows without the development of any chemical potential difference as long as ϕ is constant. On the other hand, when $I_{\text{ext}} > I_c$ the local minima of the tilted profile are turned into inflection points on top of a downward slope, so that no solutions of constant ϕ are admitted. In this regime, called of running-phase, ϕ grows monotonically and a chemical potential difference $\Delta\mu = \hbar\dot{\phi}$ develops across the junction.

3.2.3 Current-phase relation

To corroborate our observation of the dc Josephson effect, we combine the current-voltage characteristic already presented with the measurement of the current-phase relation under the same experimental conditions. In particular, we measure the relative phase ϕ emerged between the reservoirs after the injection of I_{ext} from their interference pattern arising in time-of-flight. We employ a protocol similar to that presented in Sec. 3.1.1: immediately after the barrier translation we switch off the dipole traps, let the cloud expand for a 18 ms time-of-flight and then fit the fringe pattern to extract ϕ. By repeating such procedure for various injected currents, we obtain the current-phase relation reported in Fig. 3.10 (a). The measurement is performed under the same experimental conditions of the $I - \Delta\mu$ characteristic of Fig. 3.7. The fitted value

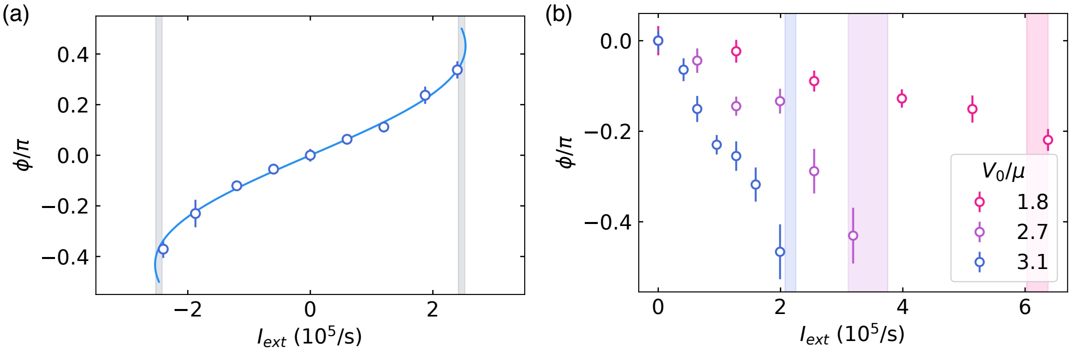

Figure 3.10: Current-phase relation of the atomic current-biased junction. (a) $I(\phi)$ measured under the same experimental condition as in Fig. 3.7. Blue solid line indicates a sinusoidal fit of data, including also the second harmonic term $I_2 \sin(2\phi)$, which contribution is found to be of the order of 10%. The confidence interval of I_c, as extracted from the fit of Fig. 3.7, is signaled by gray shaded regions. (b) Current-phase relations measured at various barrier heights V_0 with a barrier of Gaussian waist of $0.63\,\mu$m in a mBEC at $1/k_F a \simeq 4.2$. Shaded regions represent the confidence interval of I_c, independently obtained from the relative $I - \Delta\mu$ characteristics.

of I_c from Fig. 3.7 is indicated, together with its standard deviation, as the gray shaded regions. The measured $I(\phi)$ presents a clear non-linear behavior, that we fit with a sinusoidal function also accounting for a second order contribution $I_2\ \sin(2\phi)$. By constraining the first order current to be equal to the I_c value obtained from the current-voltage characteristic fit, the sinusoidal fit of $I(\phi)$ is observed to well represent the experimental data. In particular, the second order contribution is found to be small, namely $I_2/I_c = 0.12(2)$. Our measurement of a sinusoidal current-phase relation as the one originally predicted by Josephson [33] provides the first observation of the current-phase relation of a Josephson junction together with the work of Ref. [32], where $I(\phi)$ of two-dimensional crossover gases is measured with a phase imprinting technique. The evidence of a sinusoidal current-phase relation demonstrates that with our current-biased atomic junction we access the dc Josephson regime for $I_{\text{ext}} < I_c$.

Finally, we note that the regime of running-phase, for $I_{\text{ext}} > I_c$, is not addressed in our measurement. This regime of fast growing of ϕ would have been interesting to explore, as done for ac dynamics in Ref. [109] for a voltage-biased junction, but we observe that, as soon as a $\Delta\mu \neq 0$ develops, the fringe pattern contrast gets worse, making it impossible to extract a reliable value of ϕ.

The sinusoidal behavior observed in the presented current-phase relation is expected to hold only in the limit of strong barriers. In general, $I(\phi)$ is described by the Fourier expansion of Eq. (1.44), leading to different current-phase relations when the higher harmonics are included. We explore the non-sinusoidal regime by measuring $I(\phi)$ with a barrier of $0.63\,\mu$m Gaussian width, and varying its height V_0. In fact, thinner barriers are expected to facilitate the observation of the smooth change from a purely sinusoidal current-phase relation in the strong barrier regime to the one including

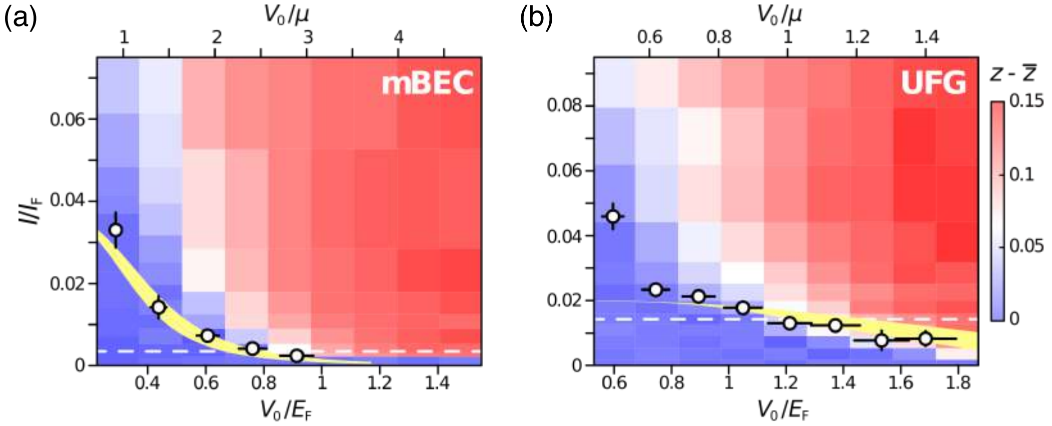

Figure 3.11: Current-imbalance characteristics for a molecular BEC (mBEC) ($1/k_Fa \simeq 4.2$) (a) and a unitary Fermi gas (UFG) ($1/k_Fa \simeq 0$) (b). Symbols indicate the values of I_c obtained from the RCSJ-model fits, normalized to $I_F \equiv I_{\text{ext}}(v = v_F)$ that represents the current injected into the junction when the barrier moves at the Fermi velocity $v_F = \sqrt{2E_F/m}$. Yellow shaded regions indicate the calculated I_{max} employing the model of Ref. [101] and following the procedure described in Sec. 3.3.1.

multiple harmonics as the barrier is weakened [128]. As reported in Fig. 3.10 (b), for sufficiently high V_0 the current-phase relation remains close to ideal case even for the thinner barrier, whereas it starts to deviate significantly from the sinusoidal form as V_0 is decreased, approaching the linear trend expected for a weak barrier for the dataset at lowest V_0/E_F [99, 128]. Furthermore, the maximum value of $|\phi|$, reached for $I_{\text{ext}} \approx I_c$, is observed to increase with the barrier height, confirming the theoretical predictions [99, 128].

3.3 Josephson critical current across the BEC-BCS crossover

The presented current-biased junction scheme provides a powerful method to measure directly the critical current I_c, which we extract from a fit of the $I - \Delta\mu$ characteristic with the RCSJ-circuit model fit. Measurements presented so far have been performed with a mBEC at $1/k_Fa \simeq 4.2$, but the same procedure applies for all fermionic superfluids in the BEC-BCS crossover. In Fig. 3.11 we report the current-imbalance characteristics of a mBEC (a) and a unitary Fermi gas (UFG) (b) measured for various barrier height V_0. For both interaction strengths we observe a plateau at $\Delta\mu \simeq 0$, represented by the blue regions in the contour plots in the figure, that witnesses the access to the dc Josephson regime even at unitarity. Each column of Fig. 3.11 (a) and (b) corresponds to a curve similar to that of Fig. 3.7, the RCSJ circuit model fit of which provides the measurement of I_c reported as a black circles. For both mBEC and UFG, the critical current is observed to monotonically decrease with V_0, as it is proportional to the tunnel amplitude $|t|$ of pairs through the barrier. Furthermore, the measured I_c can be quantitatively compared with the theoretical value expected from the semi-analytic method of Ref. [101] already presented in Sec. 1.4.3. In particular, the predictions of I_c, calculated with no free parameters as will be discussed in Sec. 3.3.1, is reported for each interaction strength as the yellow shaded region in Fig. 3.11 (a) and (b). On the one hand, the excellent agreement between experimental data and theory curve even at unitarity confirms the validity of the extention of the bosonic Eq. (1.49) to fermionic superfluids, at the basis of the model presented in Ref. [101]. As a second evidence of it, in Sec. 3.3.2 we present a comparison between the experimental data of I_c and its theoretical value throughout the crossover, that are found in quantitative agreement for all values of interactions. On the other hand, the possibility to describe the measured critical current with an expression involving the bulk properties of the superfluid allows for the extraction of their order parameter, namely the condensed fraction, as it will be discussed in Sec. 3.3.3.

3.3.1 Theoretical model for I_c in the crossover

To gain a precise microscopic understanding of the observed behavior of the Josephson critical current I_c, we employ the semi-analytic model of Ref. [101] that extends the validity of Eq. (1.49) to fermionic superfluids in the BEC-BCS crossover. The homogeneous current density of Eq. (1.49) can be generalized to harmonically-trapped samples via the local density approximation (LDA), giving [101]:

$$\hbar I_c = \int_{\mathcal{V}} d^3\mathbf{r}\, n_0(\mathbf{r})\, \mu(\mathbf{r})\, \frac{|t(\mu(\mathbf{r}), V_0)|}{4\, k(\mu(\mathbf{r}))\, R_z} = \int_{\mathcal{V}} d^3\mathbf{r}\, \lambda_0(\mathbf{r})\, n(\mathbf{r})\, \mu(\mathbf{r})\, \frac{|t(\mu(\mathbf{r}), V_0)|}{4\, k(\mu(\mathbf{r}))\, R_z}, \tag{3.15}$$

where R_z is the Thomas-Fermi radius in the z-direction of propagation of the barrier optical potential, $\mathcal{V}$ is the total volume of the junction, $n_0 = \lambda_0\, n$ is the condensate density and λ_0 the condensed fraction, $k(\mu) = \sqrt{2m_B\mu/\hbar}$, and $|t(\mu, V_0)|$ is the probability amplitude for a pair of mass $m_B = 2m$ and energy given by the pair chemical potential μ to tunnel through a barrier of height V_0.

To calculate the bulk properties of the junction across the BEC-BCS crossover, we rely on the zero-temperature polytropic approximation for the harmonically-trapped sample density profile. Under this assumption, the chemical potential is written as a power low of the density, $\mu \propto n^\gamma$, where $\gamma = \frac{\partial \log \mu}{\partial \log n}$ is the polytropic index, which is found to be a slowly varying quantity with $1/k_F a$. In particular, it takes values 1 in the BEC limit, and 2/3 for both unitary superfluids and in the BCS limit [129]. Under the polytropic approximation, the zero temperature density of an harmonically trapped sample of Fermi energy E_F is written as [130]:

$$n(\mathbf{r}) = \frac{N}{2\pi\, R_x\, R_y\, R_z\, B(3/2, 1/\gamma + 1)} \left[1 - \left(\frac{x}{R_x}\right)^2 - \left(\frac{y}{R_y}\right)^2 - \left(\frac{z}{R_z}\right)^2\right]^{1/\gamma}, \tag{3.16}$$

where N is the total number of pairs in the trap, $R_i = \sqrt{\frac{2E_F}{m\omega_i}}$ are the Thomas-Fermi radii in the three spatial directions and B is the Euler Beta function. We note that the previous expression reduces to the ideal Fermi gas density profile for $\gamma = 2/3$, as expected for a UFG at $T = 0$. The corresponding chemical potential is given by:

$$\mu(\mathbf{r}) = \mu_0 \left[1 - \left(\frac{x}{R_x}\right)^2 - \left(\frac{y}{R_y}\right)^2 - \left(\frac{z}{R_z}\right)^2\right], \tag{3.17}$$

where μ_0 is the peak chemical potential related to the homogeneous one μ_h by:

$$\mu_0 = 2E_F \left[\left(\frac{\mu_h}{2E_F}\right)^{1/\gamma} \times \frac{\sqrt{\pi}(1+\gamma)\Gamma(1/\gamma + 5/2)}{8\,\gamma\,\Gamma(1/\gamma + 2)}\right], \tag{3.18}$$

where Γ is the Gamma function. To estimate the above expressions of $\mu(\mathbf{r})$ and $n(\mathbf{r})$, we employ the Luttinger-Ward calculation of μ_h for crossover gases of Ref. [41], and use the measured value of N and ω_i in our experimental conditions. The results of Ref. [41] are taken into account also for estimating the local condensed fraction $\lambda_0(\mathbf{r})$. In fact, in an inhomogeneous system, a local interaction parameter $1/\kappa_F(\mathbf{r})a$ can be defined, where $\kappa_F(\mathbf{r}) = (6\pi^2 n(\mathbf{r}))^{1/3}$, so that the condensed fraction locally varies according to it, namely $\lambda_0(\mathbf{r}) = \lambda_0(1/\kappa_F(\mathbf{r})a)$.

We note that by employing the polytropic approximation and the Luttinger-Ward calculations of Ref. [41], we assume that our $T/T_F = 0.06(2)$ gas could be described as a zero-temperature system. As it will be demonstrated in Sec. 4.2.2 for a UFG, at the low temperature here investigated the condensed fraction is almost unaffected by the locally varying degeneracy of the cloud, as it essentially coincides with its $T = 0$ value throughout the sample. Furthermore, the critical current is observed to present a small dependency on T/T_F at low temperature, at least at unitarity, as it will be discussed in Sec. 4.2.1, so that the I_c value measured at $T/T_F = 0.06(2)$ is compatible with the zero-temperature one.

To model the single-pair junction transmission $|t(\mu, V_0)|$, we employ the analytic expression for the tunneling amplitude of a particle through an Eckart potential barrier. As already discussed in Sec. 3.1.1, the Eckart profile $V(x) = V_0/\cosh^2(x/d)$ provides a good approximation of the Gaussian barrier potential once the size of the Eckart barrier is set to $d = 0.6\,w$, where w is the barrier Gaussian width. The transmission probability $T = |t|^2$ for a particle of mass M and energy ϵ through an Eckart barrier of height V_0 is given by [131]:

$$T(\epsilon, V_0) = \begin{cases} \frac{\sinh^2\left(\pi\sqrt{2\epsilon/\epsilon_b}\right)}{\sinh^2\left(\pi\sqrt{2\epsilon/\epsilon_b}\right)+\cosh^2\left(\frac{\pi}{2}\sqrt{8V_0/\epsilon_b - 1}\right)} & \text{for } V_0/\epsilon_b \geq 1/8 \\ \frac{\sinh^2\left(\pi\sqrt{2\epsilon/\epsilon_b}\right)}{\sinh^2\left(\pi\sqrt{2\epsilon/\epsilon_b}\right)+\cos^2\left(\frac{\pi}{2}\sqrt{1 - 8V_0/\epsilon_b}\right)} & \text{for } V_0/\epsilon_b < 1/8 \end{cases}, \tag{3.19}$$

where $\epsilon_b = \hbar^2/(Md^2)$ is the characteristic energy of the barrier. We check the validity of the Eckart approximation by comparing its transmission probability T with that obtained for a Gaussin barrier [132]. Fig. 3.12 shows that the overlap between the two curves is very good in the regime of low energy $\epsilon \lesssim 0.5\,V_0$, while in the opposite limit, for $\epsilon > 0.5\,V_0$, the transmission probability of the Eckart barrier deviates more appreciably

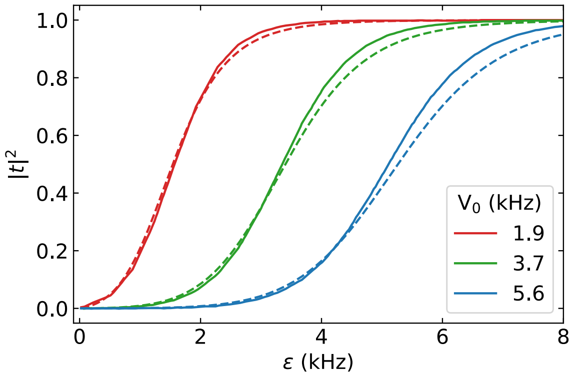

Figure 3.12: Comparison of the transmission probability through a Gaussian barrier of width $w = 0.95\,\mu$m (solid lines) and an Eckart one with dimension $d = 0.6\,w$ (dashed lines), for different barrier height V_0 as a function of the incident energy ϵ. Gaussian barrier transmissions are taken from Ref. [132].

from that of the Gaussian one. Anyway, the relative discrepancy between the two curves is within a few percent, small enough to not seriously affect the calculation of I_c. Moreover, the real barrier is typically set to transmission probabilities $T < 0.5$, so that only the region of best agreement between Eckart and Gaussian transmission is experimentally explored.

To calculate the tunneling probability amplitude of a pair, we set $M = 2m$, $\epsilon = \mu = 2\mu_F$, where μ_F is the single fermion chemical potential, and employ the barrier height V_0 obtained with the calibration presented in Sec. 3.1.1. Furthermore, we take into account the barrier divergence along the z propagation direction. In fact, the depth of focus of the projected Gaussian barrier of width $w_0 = 0.95\,\mu$m is comparable with the typical radial size of the harmonically trapped cloud, so that the barrier size and height are not constant along z. Therefore, we approximate the projected barrier as a single-mode Gaussian beam, focused at the center of the cloud ($z = 0$) where its waist and height are set to be w_0 and V_0, respectively. Within this approximation, away from the center, the barrier width and height are given by $w(z) \simeq w_0\sqrt{1 + (z/z_R)^2}$ and $V(z) \simeq V_0/\sqrt{1 + (z/z_R)^2}$, where $z_R = \pi w_0^2/\lambda$ is the Rayleigh length associated to w_0 and $\lambda = 532\,$nm.

To estimate the critical current more accurately, we include also the second-harmonic contribution to the supercurrent I_2. This correction increases the value of the total supercurrent, providing a more significant contribution as the strong barrier approximation $V_0 > \mu$ starts to fail. The second order current density of Eq. (1.50) can be generalized to harmonically trapped samples similarly to I_c, namely:

$$\hbar|I_2| = \int_{\mathcal{V}} d^3\mathbf{r}\,\lambda_0(\mathbf{r})\,n(\mathbf{r})\,\mu(\mathbf{r})\,\frac{|t(\mu(\mathbf{r}), V_0)|^2}{16\,k(\mu(\mathbf{r}))\,R_z}, \tag{3.20}$$

which we calculate under the same approximations previously described for I_c. The

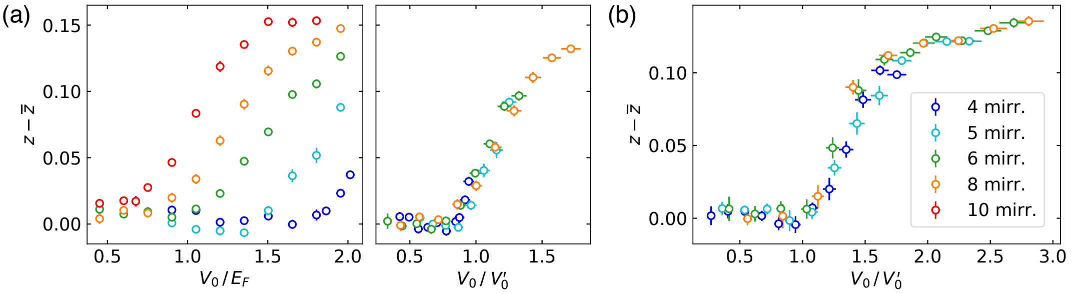

Figure 3.13: Response of the atomic junction after the injection of a constant current I_{ext} for different barrier height V_0 and size as specified in the legend in number of mirrors in the DMD image. (a) UFG at $1/k_F a \simeq 0$ and barrier velocity of 0.4 mm/s. Right panel: same data as in the left one, once rescaled for the calculated value of critical height V_0' with our theory model, such that $I_{\text{ext}} = I_c$ at the given barrier size. (b) mBEC at $1/k_F a \simeq 4.2$ and barrier velocity 0.1 mm/s. Data are rescaled as in (a-right) for the given interaction strength.

total supercurrent I_{max} is finally obtained as [133]:

$$I_{\text{max}} = f(g) I_c = \frac{(\sqrt{1+32\,g^2}+3)^{3/2}\,(\sqrt{1+32\,g^2}-1)^{1/2}}{32\,|g|} I_c, \tag{3.21}$$

where $g = |I_2|/I_c$. The correction factor $f(g) > 1$ is observed to increase I_{max} up to 10% for the lowest barriers employed in the measurements presented in this chapter. Therefore, we estimate the total maximum supercurrent using Eq. (3.21) and calculating I_c and I_2 with no free parameter. The yellow shaded regions of Fig. 3.11 are obtained by taking into account a 10% uncertainty on the barrier size w_0 and employing a condensed fraction of 1 for the mBEC and 0.51 for the UFG [41]. Measured I_c and calculated I_{max} with our model are found to be in quantitative agreement, deviating only for low barrier heights $V_0 < \mu$, where the hydrodynamic transport, not included in the model, is expected to become relevant.

As a further check of the validity of our model, we investigate the behavior of the atomic junction under varying the barrier size. In our model, the critical current depends on the barrier width solely via the tunneling amplitude $|t|$, that is a function of the barrier height as well. Therefore, to verify the separation between single- and many-particle properties of Eq. (1.49), namely between tunneling amplitude and bulk superfluid characteristics, we measure the imbalance developed in the junction after the injection of a constant current while changing the barrier size and height. As illustrated in Fig. 3.13 (a-left) for a UFG, the critical height V_0', for which the injected current $I_{\text{ext}} = I_c$, decreases as the barrier size is increased, since the tunneling amplitude is higher for thinner barriers. Furthermore, if we normalize V_0 to the critical barrier height V_0' calculated with our model for each value of w_0, all different datasets collapse onto each other, as reported in Fig. 3.13 (a-right). We note that in the second plot the dataset obtained with the largest barrier size of 10 DMD mirrors is not considered, as the shape of such barrier is rather flat-top than Gaussian (see Fig. 3.2 (a)) and the Eckart approximation starts to fail. The 8 DMD mirrors dataset is instead included

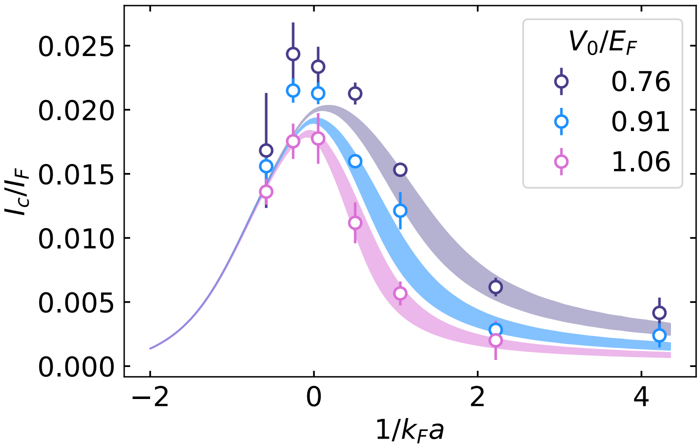

Figure 3.14: Critical current measurement across the BEC-BCS crossover for different barrier heights. Shaded regions are obtained with the analytic model presented in Sec. 3.3.1, employing the pair condensate fraction and chemical potential from Ref. [41] and accounting for a 5% uncertainty in the barrier width.

and observed to collapse onto the others, despite such large barrier already shows relevant deviation from a Gaussian shape. The same collapse of datasets at different w is observed also for a mBEC, as reported in Fig. 3.13 (b). This demonstrates that, for fixed interaction strength, not only the critical value of I_c, but the whole trend of the imbalance is mostly determined by the tunneling amplitude $|t|$, and that our model is able to well capture it.

3.3.2 Critical current of fermionic superfluids

The measurement of the critical current can be extended throughout the BEC-BCS crossover, by acquiring the $I-\Delta\mu$ characteristic of the atomic junction at different magnetic field. In particular, to do that we evaporate the gas at resonance and successively sweep the magnetic field to the desired value, before ramping up the DMD potential to create the junction. For all the interaction strengths investigated, the junction is observed to support the dc Josephson effect for injected current smaller than the critical one, which is extracted by performing an RCSJ-circuit model fit on the measured $I-\Delta\mu$ characteristic. The I_c results obtained for three different values of barrier height V_0 are reported in Fig. 3.14. All datasets show a non-monotonic trend of I_c peaked around unitarity, consistently with theoretical simulations [93, 99] and previous experimental results [85]. Shaded regions in the figure are obtained employing the theory model presented in the previous section with no free parameters: their agreement with experimental data is quantitatively good, especially for the largest barrier height V_0, which is more in the limit of strong barrier. This evidence demonstrate the validity of the extension of Eq. (1.49) for crossover gases proposed in Ref. [101] and confirms the interpretation of the critical current trend as due to the combination of the competing behavior of chemical potential and condensed fraction. As already discussed in Sec. 1.4.3, while the condensed fraction is expected to monotonically increase moving from the BCS to the BEC limit, the predicted trend of chemical potential is opposite, determining the non-monotonic behavior of the critical current, which is directly depending on both of them. Therefore, our results demonstrate that it is condensation, rather than superfluidity, at the basis of Josephson effect.

3.3.3 Measurement of the order parameter

The direct proportionality of the critical current with the condensed density n_0 in our model allows for the extraction of the condensed fraction of fermionic superfluids from the measured I_c. In fact, Eq. (3.15) can be approximated with:

$$\hbar I_c \approx \langle \lambda_0 \rangle \int_{\mathcal{V}} d^3\mathbf{r}\, n(\mathbf{r})\, \mu(\mathbf{r})\, \frac{|t(\mu(\mathbf{r}), V_0)|}{4\, k(\mu(\mathbf{r}))\, R_z}, \tag{3.22}$$

where $\langle \lambda_0 \rangle$ is the density weighted condensed fraction, defined as:

$$\langle \lambda_0 \rangle = \frac{\int_{\mathcal{V}} d^3\mathbf{r}\, \lambda_0(\mathbf{r})\, n(\mathbf{r})}{\int_{\mathcal{V}} d^3\mathbf{r}\, n(\mathbf{r})}. \tag{3.23}$$

A similar approximation for the second order critical current leads to the factorizations:

$$I_c \approx \langle \lambda_0 \rangle I_{c,\text{sup}}, \tag{3.24}$$

$$I_2 \approx \langle \lambda_0 \rangle I_{2,\text{sup}}, \tag{3.25}$$

where $I_{c,\text{sup}}$ and $I_{2,\text{sup}}$ are calculated by setting $\lambda_0(\mathbf{r}) \equiv 1$ in Eqs. (3.15) and (3.20), respectively. Being $\lambda_0(\mathbf{r})$ a slowly-varying quantity in harmonically trapped superfluids, the above approximation is well founded, as we further confirm by observing a discrepancy up to 3% from the exact evaluation of I_c and I_2 with Eqs. (3.15) and (3.20) across the experimentally explored range of interaction strengths. Therefore, the expression of the maximum Josephson current of Eq. (3.21) can be recast as:

$$I_{\text{max}} \approx \langle \lambda_0 \rangle f(g_{\text{sup}}) I_{c,\text{sup}}, \tag{3.26}$$

where $g_{\text{sup}} = |I_{2,\text{sup}}|/I_{c,\text{sup}}$. By employing the latter relation and the experimentally determined Josephson critical current I_c^{exp}, we extract $\langle \lambda_0 \rangle$ for each coupling strength across the BCS-BEC crossover as:

$$\langle \lambda_0 \rangle \approx \frac{I_c^{\text{exp}}}{f(g_{\text{sup}})\, I_{c,\text{sup}}}. \tag{3.27}$$

The values of density weighted condensed fraction obtained with the described procedure are presented in Fig. 3.15, compared with several theoretical predictions. In particular, we report as red squares data extracted from I_c^{exp} dataset at $V_0/E_F = 1.06$ only and as black circles the average $\langle \lambda_0 \rangle$ over all the datasets in Fig. 3.14. In the strongly interacting regime of $|1/k_F a| < 1$, the experimental data are observed to

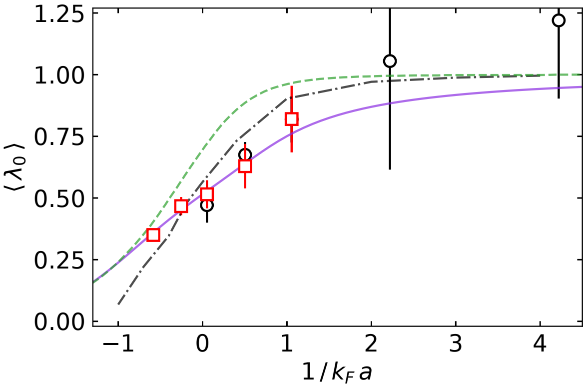

Figure 3.15: Density weighted condensed fraction $\langle \lambda_0 \rangle$ obtained from I_c measurement of Fig. 3.14 including all datasets (black circles) or only the $V_0/E_F \simeq 1.06$ one (red squares). Experimental values of $\langle \lambda_0 \rangle$ are compared with several theoretical predictions: homogeneous Luttinger-Ward calculations of Ref. [41] are plotted as solid purple line, Monte Carlo simulations and mean field theory of Ref. [60] in dot-dashed gray and dashed green lines respectively.

be consistent with the theoretical predictions of a $T = 0$ homogeneous sample. In particular, the value of $\langle \lambda_0 \rangle = 0.47 \pm 0.07$ found at unitarity is consistent with the Luttinger-Ward prediction of $\lambda_0 = 0.51$ of Ref. [41] and the value of $\lambda_0 = 0.43(2)$ recently calculated in Ref. [61] with auxiliary-field lattice Monte Carlo simulations, but slightly smaller than the $\lambda_0 = 0.57$ obtained with Monte Carlo simulations of Ref. [60]. Our result at unitarity is instead much smaller than the previous experimental results of Ref. [62, 63] in agreement with the mean field value of $\lambda_0 \simeq 0.7$. The mentioned experiments employed the rapid ramp technique, which is indeed expected to overestimate the condensed fraction [64]. Our results demonstrate Josephson effect as a quantitative probe for the condensed density, providing a direct measurement of the order parameter of fermionic superfluids, which determination has been so far challenged by the strong interactions.

3.4 Normal conductance characterization

The current-voltage characteristic provides a measurement of the conductance G of the atomic junction as well, which is extracted from the RCSJ model fit of the $I - \Delta\mu$ curve. The values of G measured from data reported in Fig. 3.11 are presented in Fig. 3.16 for a mBEC (a) and a UFG (b), together with the corresponding Stewart-McCumber parameter $\beta_c = I_c C/(\hbar G^2)$ (light blue circles). Both G and β_c shows an exponential dependency on the barrier height V_0. In particular, for both interaction strengths, the Stewart-McCumber parameter is observed to vary largely in the explored range of V_0, reaching the underdamped regime of $\beta_c \gg 1$, where the $I - \Delta\mu$ characteristic is expected to be highly hysteretic.

On the other hand, the conductance of our atomic junction is particularly high, suggesting the presence of an anomalous contribution in G not only for the mBEC. As

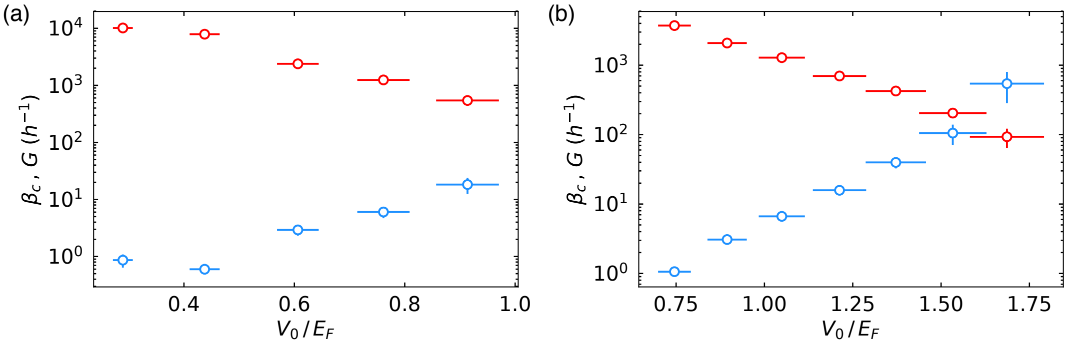

Figure 3.16: Normal conductance G (red circles) and Stewart-McCumber parameter β_c (light blue circles) as a function of the barrier height V_0 for a mBEC (a) and a UFG (b). G is extracted from the RCSJ model fit of data reported in Fig. 3.11.

already discussed in Sec. 1.4.3, for a weakly interacting BEC the normal conductance is expected to be non-zero even at zero temperature, thanks to an anomalous contribution to transport given by condensed particles coherently converted into phononic excitations. The high values of G measured for the UFG, almost of the same order of those of the mBEC, suggest the presence of an anomalous contribution even in the strongly-interacting regime, as it will be discussed in depth in the next chapter, where the unitary junction conductance is measured as a function of temperature. Here, we only remark that the observed scaling of the conductance with the critical current, as reported in Fig. 3.17, clearly differs from that of a SJJ, ruled by the Ambegaokar-Baratoff relation of Eq. (1.38). In fact, we find a quadratic scaling $G \propto I_c^2$, in agreement with the prediction for weakly interacting BECs, where dissipative normal currents are associated with the emission of Bogoliubov sound modes or localized vortex-like excitations and arise only in the second order of the tunneling amplitude [34].

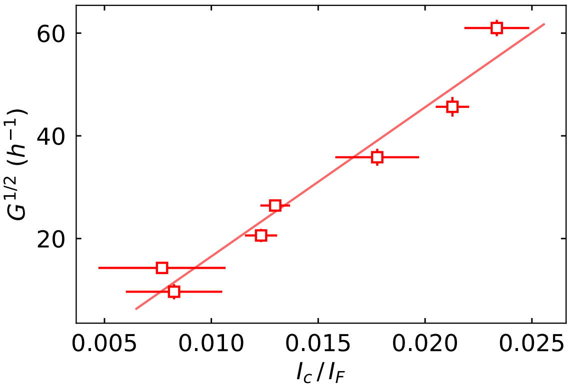

Figure 3.17: Scaling of the conductance G with the critical current I_c for a unitary junction ($1/k_F a \simeq 0$). Both G and I_c are extracted from the $I - \Delta\mu$ characteristic of Fig. 3.11 (b). The solid line represent a linear fit on data.

Chapter 4

A current-biased tunnel junction across the superfluid transition

The Josephson effect provides a powerful probe for any condensed state, that in the previous chapter we employed to characterize the superfluid order parameter as a function of the coupling strength across the BEC-BCS crossover. Here, we show how Josephson supercurrents can successfully characterize the superfluid phase at finite temperature as well. In particular, by exploiting the current-biased junction scheme already presented, we observe the current-chemical potential curve of a unitary junction to evolve from the highly non-linear revealed in the low temperature regime to fully resistive, as the superfluid phase transition is crossed from below. Because of condensate depletion for increasing temperature, the maximum supercurrent of dc Josephson, $I_{s,\max}$, is observed to vanish when the critical temperature $T_c \simeq 0.21\, T_F$ [134, 135] is approached, providing a striking signature of the phase transition. Remarkably, the presence of a condensed state is found to determine not only the dissipationless supercurrent, but also the Ohmic conduction, feeding both Josephson and normal currents. In particular, we observe a large anomalous contribution to the normal conductance G, which is due to the tunnel coupling between the condensate and phononic Bogoliubov-Anderson excitations. Furthermore, from the G scaling with the barrier parameters, we distinguish the nature of the conduction carriers, observing a change from paired fermions below T_c to unpaired particles immediately above critical. The main results of our work have been collected in the following publication:

- G. Del Pace, W. J. Kwon, M. Zaccanti, G. Roati and F. Scazza , *Tunneling transport of unitary fermions across the superfluid transition*, arXiv preprint arXiv:2010.00582, under evaluation in Phys. Rev. Lett.

This chapter is organizes as it follows. In Sec. 4.1.1 we present the protocol we implemented to tune the temperature of the junction and the thermometry methods employed both at unitarity and in the crossover. Sec. 4.2 discusses the breakdown of dc Josephson effect for temperatures approaching T_c. The vanishing trend of $I_{s,\max}$ is found to be in quantitative agreement with an extension to finite T of the theory model already presented and enables us to provide a lower limit of the critical temperature for the superfluid transition of strongly-interacting gases. Finally, in Sec. 4.3 we discuss the measurement of normal conductance at finite temperature, demonstrating the presence of the anomalous contribution and discriminating between paired and unpaired transport carriers.

4.1 Tuning the temperature of the junction

We explore the atomic Josephson junction behavior across the superfluid transition by varying the temperature of the sample. Tuning the temperature of an ultracold cloud without affecting other properties of the system is not an easy task. In fact, colder or hotter samples can be easily produced by tuning the final intensities of the beams forming the crossed ODT. However, this method has the drawback of changing the trap frequencies and particle number, that together fix the Fermi energy E_F of the sample. To vary the cloud temperature only, we thus employ a parametric heating technique [136, 137]. By introducing a small amplitude modulation of the Mephisto beam intensity, at a frequency about twice the radial one of the crossed ODT, we can excite the sample at a constant heating rate, without changing the final trap frequencies. However, the energy introduced in the system translates into atom losses, that modifies the number of trapped particles. We control the number of atoms in the final trap by adding a recompression stage after the evaporation sequence. Before reaching the final intensity configuration, that fixes the trap frequencies, IPG and Mephisto powers are reduced down to a variable minimum that sets the temperature and the number of atoms in the system. Such an intensity minimum is tuned together with the parametric heating duration and amplitude to produce a final cloud with $N \simeq 1.5 \times 10^5$ atoms per spin state at a variable temperature in the range $T/T_F = 0.07 - 0.23$. The trap frequencies in the crossed ODT for the measurements presented in this chapter are set to $(\omega_x, \omega_y, \omega_z) = 2\pi \times (17, 300, 290)$ Hz, so that the Fermi energy of the sample is $E_F \simeq h \times 11$ kHz.

Once the sample in the crossed trap is produced at the desired temperature, we create the atomic junction by following the same procedure described in Sec. 3.1. In particular, the two reservoirs consist of $N_{R,L} \simeq 4 \times 10^4$ atoms per spin state each, and are separated by the already presented DMD-made repulsive barrier of Gaussian width $w_0 = 0.95(9)\,\mu$m along the axial direction. We verify that turning on the DMD potential does not affect the temperature of the system, that we always measure in the crossed harmonic trap. In particular, we employ three different methods for measuring the temperature of the unitary cloud, as presented further below, together with the protocol we adopt for addressing the junction temperature away from unitarity.

4.1.1 Thermometry of a Unitary Fermi gas

The UFG temperature is extracted by analyzing the *in-situ* images of atoms in the crossed trap, obtained with the high-resolution vertical imaging presented in Sec. 2.2.2. In particular, we perform the analysis on the mean density profile of at least 10 ex-

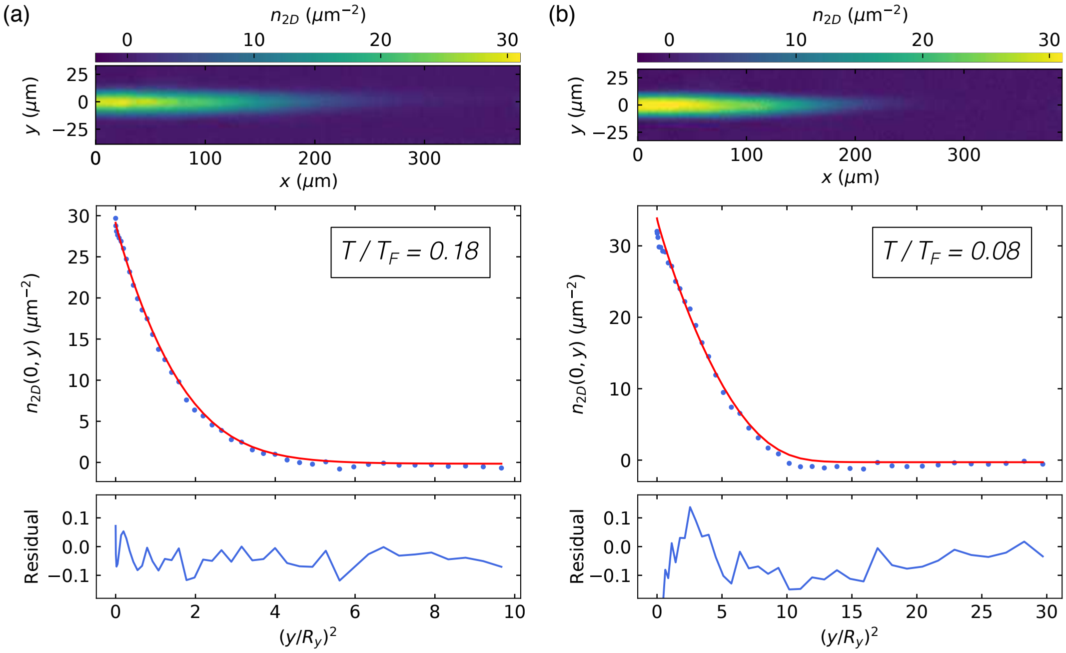

Figure 4.1: Temperature extraction via the two-dimensional non-interacting Fermi gas fit for a $T/T_F = 0.18$ (a) and $T/T_F = 0.08$ (b) sample. On top: in-situ images of the unitary Fermi gases ($1/k_Fa \simeq 0$) in the crossed optical dipole trap at the two temperature. Images consist of an average over about 10 experimental realizations, that for each temperature is used for thermometry, folded in half cloud by averaging the two axial sides. At the center: comparison of a radial cut of the top image (blue circles) with the non-interacting Fermi gas fit (red line). On bottom: relative residuals of the fit, defined as the difference between the data and the fitted function re-scaled by the average density. The y-axis is presented in adimensional unit, where $R_y = 8.05(1)\mu$m and $R_y = 4.48(3)\,\mu$m are the radial cloud size extracted from the fit of (a) and (b), respectively.

perimental realizations for each measurement, employing different methods that give consistent results. We first estimate the temperature of the UFG cloud by performing a two-dimensional fit of its density profile with the non-interacting fit function. We then check the validity of such phenomenological fit by comparing it with two additional methods that rely on the density equation of state of the unitary gas.

Phenomenological fit

As a first estimation of the unitary cloud temperature, we perform a phenomenological fit of the acquired two-dimensional density profiles with that of a harmonically trapped non-interacting Fermi gas. In particular, we use the following fitting function [16]:

$$n_{2D}(x,y) = n_{2D,0}\,\frac{\mathrm{Li}_2\left(-\exp\left[q_0 - \left(x^2/R_x^2 + y^2/R_y^2\right) f\left(e^{q_0}\right)\right]\right)}{\mathrm{Li}_2\left(-\exp(q_0)\right)}, \tag{4.1}$$

where $q_0 = \beta\mu_0$ is the logarithm of the fugacity, $R_{x,y}$ are the Thomas-Fermi radii and the function $f(x)$ is defined as:

$$f(x) = \frac{\mathrm{Li}_1(-x)}{\mathrm{Li}_0(-x)} = \frac{1+x}{x}\ln(1+x), \tag{4.2}$$

where $\mathrm{Li}_n(x)$ is the polylogarithm function of order n. The degeneracy of the cloud is then calculated from the fitted value of q_0 as:

$$\frac{T}{T_F} = \left[-6\mathrm{Li}_3\left(-e^{q_0}\right)\right]^{1/3}. \tag{4.3}$$

We note that there is no a priori reason way a UFG at finite T should be represented by the non-interacting equation of state, despite the two profiles coinciding at zero temperature. However, the shape of the two gases are experimentally found to be very similar, as illustrated by Fig. 4.1, and Eq. (4.1) is routinely used to fit the UFG density profile [16]. The real degeneracy of the UFG is obtained from the effective one of Eq. (4.3), upon rescaling by $\sqrt{\xi}$, which is the same factor that relates the peak chemical potential of an ideal gas to that on a UFG in an harmonic trap. Despite the Bertsch parameter being a function of T/T_F, the range of temperature explored in our measurements is small enough to use its zero-temperature value $\xi = 0.37$ for the rescaling of such parameter. Relying on a two-dimensional fitting procedure, this phenomenological fit provides a robust thermometry method against background fluctuations. However, it is expected to become less accurate at very low temperature, both for UFG and for an ideal Fermi gas. In fact, the information on T/T_F is contained in the low density wings of the cloud, that are progressively reduced as the temperature decreases. As shown in Fig. 4.1 (b), the phenomenological fit start to fail on the cloud wings for $T/T_F \lesssim 0.1$, and other thermometry methods must be employed to have a reliable thermometry in such a regime.

Fit with unitary gas equation of state

A more appropriate, but unfortunately less robust, method to measure the temperature of a unitary gas is to fit its density profile with the known equation of state (EoS). As presented in Sec. 1.2.4, the EoS of a homogeneous UFG is given by Eq. (1.26), which can be extended under local density approximation (LDA) for a trapped sample. Under this assumption, the local chemical potential can be written as:

$$\mu(\mathbf{r}) = \mu_0 - V_h(\mathbf{r}) = \mu_0 - \frac{1}{2}m\omega_x^2x^2 - \frac{1}{2}m\omega_y^2y^2 - \frac{1}{2}m\omega_z^2z^2, \tag{4.4}$$

where μ_0 is the peak chemical potential and $V_h(\mathbf{r})$ is the harmonic trap confinement of frequencies $\omega_{x,y,z}$. The UFG density profile is therefore obtained by employing a local $q(\mathbf{r}) = \beta\,\mu(\mathbf{r})$ into Eq. (1.22) to give:

$$\begin{aligned} n(\mathbf{r}) &= \frac{1}{\lambda_{dB}^3}\, f_n(q(x,y,z)) = \\ &= \frac{1}{\lambda_{dB}^3}\, f_n\left(\beta\mu_0 - \frac{\beta m}{2}\omega_x^2x^2 - \frac{\beta m}{2}\omega_y^2y^2 - \frac{\beta m}{2}\omega_z^2z^2\right) \end{aligned} \tag{4.5}$$

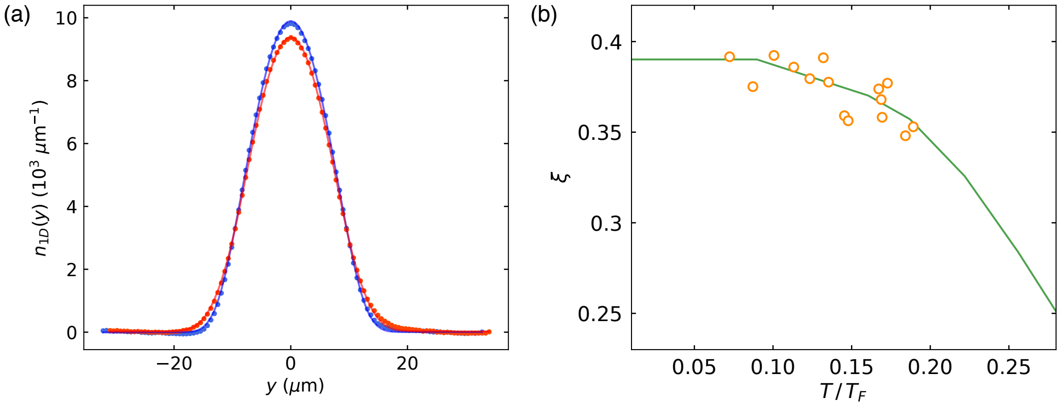

Figure 4.2: Fit with unitary EoS of the one dimensional density profile. (a) Comparison between experimental density profiles (circles) and corresponding fit with Eq. (4.7) (lines) at two different temperatures. Both fits are performed by calculating $\mathcal{A}$ and keeping $\tilde{T}$, $\tilde{\mu}$ and R_y as free parameters, yielding $T/TF = 0.077(5)$ and $T/TF = 0.125(3)$ for the blue and the red profile, respectively. (b) Estimated $\xi(T/T_F)$ from the one-dimensional density fit (orange circles) compared with the calculated values of μ_0/E_F employing the unitary gas EoS at fixed atom number and trap frequencies.

where the function $f_n(q)$ is given by Eq. (1.26). Such expression for the density can be integrated along the z imaging direction to provide an expression for n_{2D}, which we can employ to fit the acquired UFG distribution. Since f_n is not an analytic function, the integration must be performed numerically, and the two-dimensional fitting procedure turns out to be heavy and not particularly robust. Nonetheless, by integrating $n(\mathbf{r})$ along both z and x directions, and changing the integration variables from cartesian to cylindrical ones, the expression of the one-dimensional density profile $n_{1D}(y)$ is considerably simplified, taking the form [138, 139]:

$$n_{1D}(y) = \frac{2\pi}{m\omega_y\omega_z}\frac{k_BT}{\lambda_{dB}^3} f_s\left(\beta\mu_0 - \frac{\beta m}{2}\omega_y^2 y^2\right), \tag{4.6}$$

where we defined the function $f_s(q) = \int_{-\infty}^{q} f_n(s)ds$. The advantage of the one-dimensional fit, respect to the two-dimensional one, is that $f_s(q)$ can be integrated numerically once and for all, while the numerical integral for n_{2D} should be performed for each fitting procedure. Therefore, we employ the one-dimensional fit of the density profile, which provides a rapid procedure to extract the temperature, at the cost of the loss of information due to the integration of the acquired profile along the x direction. In particular, we recast the previous expression of n_{1D} into the convenient fitting function:

$$n_{1D}(y) = \mathcal{A}\tilde{T}^{5/2} f_s\left(\frac{\tilde{\mu} - y^2/R_y^2}{\tilde{T}}\right), \tag{4.7}$$

where $\mathcal{A} = \sqrt{2\pi/m}\,\omega_z\omega_x\hbar^3/E_F^{5/2}$, $R_y = \sqrt{2E_F/(m\omega_y^2)}$ is the Thomas-Fermi radius, $\tilde{T} = T/T_F$ is the rescaled temperature and $\tilde{\mu} = \mu_0/E_F$ is the reduced chemical potential. Fig. 4.2 (a) reports the fit of two different samples, performed by calculating $\mathcal{A}$

from the knowledge of trapping frequencies and number of atoms, while keeping $\tilde{T}$, $\tilde{\mu}$ and R_y as free parameters. The agreement between the measured density profile and the corresponding fit is extremely good for both temperatures, that are estimated to be $T/T_F = 0.077(5)$ and $0.125(3)$ for the blue and red data, respectively. Furthermore, being the reduced chemical potential $\tilde{\mu} = \mu_0/E_F = \sqrt{\xi}$ by definition, our fitting procedure provides also an estimation of the Bertsch parameter. In Fig. 4.2 (b), we plot as orange circles the ξ value extracted form the fit of all the available datasets as a function of the temperature. As a check of the fitting procedure consistency, we compare the fitted values with the calculated $(\mu_0/E_F)^2$ (green line) by employing the EoS Eq. (4.5), under the constraint of fixed number of atoms and trap frequencies. The agreement between fitted and calculated value of ξ verifies the reliability of the extracted T/T_F.

We note that with an identical procedure, the axial density profile $n_{1D}(x)$ can be computed. We choose to perform the fit along the y-direction, since the radial wings of the density profile lie entirely within the field of view of our imaging system, and they are essential for the temperature extraction. Conversely, as the axial dimension of our cloud is comparable with the 150 μm field of view of our microscope objective, the one-dimensional fit of the axial profile provides a less reliable estimation of T/T_F.

Virial theorem

As a last thermometry method, we employ a procedure based on the virial theorem, which has been demonstrated to be valid for strongly-interacting gases in Ref. [140]. The virial theorem states that the total energy E of a gas trapped in the confining potential $U(\mathbf{r})$ can be written as:

$$E = \langle U \rangle + \frac{1}{2}\langle \mathbf{r} \cdot \nabla U(\mathbf{r}) \rangle, \tag{4.8}$$

where the brackets indicate the trap average:

$$\langle U \rangle = \int d^3\mathbf{r}\, n(\mathbf{r})\, U(\mathbf{r}). \tag{4.9}$$

For a harmonic trapping potential, $\mathbf{r} \cdot \nabla U(\mathbf{r}) = 2\,U(\mathbf{r})$, and the total energy simply reduces to:

$$E = 2\langle U \rangle = 3m\omega_i^2 \langle r_i^2 \rangle, \tag{4.10}$$

where we have used the fact that $\omega_x^2\langle x^2 \rangle = \omega_y^2\langle y^2 \rangle = \omega_z^2\langle z^2 \rangle$. The total energy of an atomic cloud can be thus easily computed from its density profile, by measuring the trap frequencies and calculating the second moment of the density distribution $\langle r_i^2 \rangle$ as:

$$\langle r_i^2 \rangle = \int d^3\mathbf{r}\, n(\mathbf{r})\, r_i^2 = \int_{-\infty}^{+\infty} dr_i\, n_{1D}(r_i)\, r_i^2. \tag{4.11}$$

From the knowledge of the total energy of the cloud, we can directly determine its temperature, since the two quantities are connected by the EoS. In particular, the

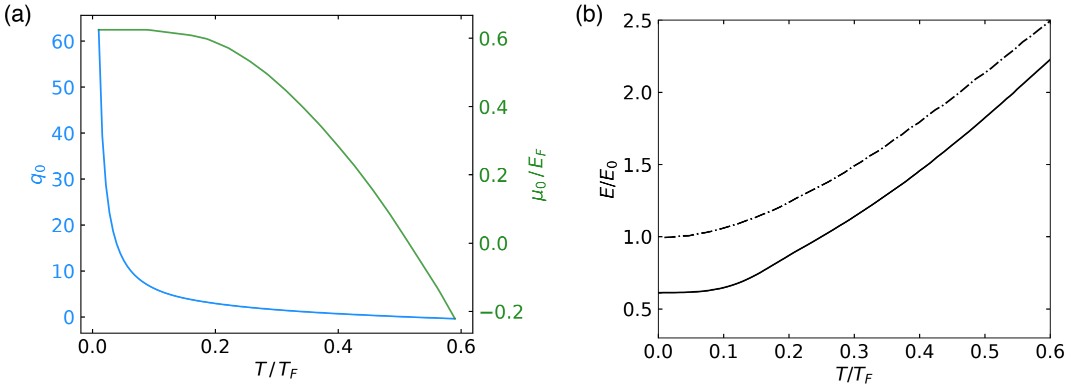

Figure 4.3: Total energy calculation via virial theorem as a function of temperature. (a) Peak chemical potential μ_0 and $q_0 = \beta\mu_0$ as a function of temperature. The first is calculated by numerically solving Eq. (4.5) under the constraint of fixed number of atoms. (b) Total energy E as a function of degeneracy parameter T/T_F for unitary (solid line) and non-interacting (dot-dashed line) Fermi gases, obtained by numerically solving Eq. (4.12), assuming the UFG and ideal EoS respectively. In both cases, E is normalized to the total energy $E_0 = \frac{3}{4}NE_F$ of a zero temperature non interacting cloud containing the same number of atoms.

total energy of a UFG, normalized to that of an ideal gas with the same number of particles at zero temperature $E_0 = \frac{3}{4}NE_F$, is given by [138]:

$$\frac{E}{E_0} = \frac{4\sqrt{2\pi}}{3(3\sqrt{2}\pi)^{1/3}} \frac{M_2(q_0)}{M_0(q_0)}, \tag{4.12}$$

where $q_0 = \beta\mu_0$ and $M_l(q)$ are the dimensionless moments of the EoS distribution, defined as:

$$M_l(q) = \int_{-\infty}^{q} (q-s)^{(l+1)/2} f_n(s)\, ds. \tag{4.13}$$

At a given temperature, the value of q_0 is set by μ_0, as reported in Fig. 4.3 (a), with the latter calculated by constraining the number of atoms in the EoS of Eq. (4.5) to be the same as in our experimental conditions. For each value of q_0, the integral in the definition of M_l can be numerically computed to calculate the E/E_0 trend as a function of temperature, shown in Fig. 4.3 (b) as solid line. Therefore, by measuring the total energy of the acquired UFG density distribution, the degeneracy T/T_F of the cloud is obtained by inverting the relation in Eq. (4.12).

The presented thermometry method thus relies on the estimation of the second moment of the distribution $\langle r_i^2 \rangle$, which can be done either by integrating the acquired column density, or by fitting n_{2D} with a given function and then analytically calculating its second moment. The first method suffers of background fluctuations, as the dominant contribution to the second moment is provided by the wings of the cloud. On the other hand, we already illustrated the capability of the non-interacting fit function of Eq. (4.1) to well reproduce the UFG density profile. Therefore, we can employ it to calculate $\langle r_i^2 \rangle$ with the curve fitting method, since the second moment of the function in Eq. (4.1) can be steadily calculated as:

$$\langle r_i^2 \rangle = \frac{N}{2} R_i^2 \frac{\mathrm{Li}_4\left(-e^{q_0}\right)}{\mathrm{Li}_3\left(-e^{q_0}\right)}, \tag{4.14}$$

where R_i is the Thomas-Fermi radius in the $i = x, y$ direction. From a two-dimensional fit of the acquired density profile we obtain all the needed parameter to calculate $\langle r_i^2 \rangle$ with the previous expression. We note that, in order to evaluate it, we have used the following property of the polylogarithm function [16]:

$$\int_{-\infty}^{+\infty} \mathrm{Li}_n\left(\alpha\, e^{-x^2}\right) dx = \sqrt{\pi}\, \mathrm{Li}_{n+1/2}(\alpha). \tag{4.15}$$

For all the analyzed datasets, we employ both methods to estimate the second moment of the density distribution: the difference between the two is found to be less then 1% when the background is properly rescaled.

As already mentioned, the total energy E can be expressed in the form of Eq. (4.10) only when the trapping potential is harmonic. However, optical dipole traps are created with Gaussian beams, that produce a harmonic profile only in first approximation, once particles explore only the region close to the potential minimum. The Gaussian profile of the optical trap is expected to provide a small correction to the total energy calculation, which anyway might be not negligible in the case of our crossed trap. In fact, a small misalignment of the IPG and Mephisto beams may cause the trap to be anharmonic. We estimate the first anharmonic correction to the total energy by assuming a Gaussian profile for the optical potential and Taylor expand it up to second order to calculate $\langle \mathbf{r} \cdot \nabla U(\mathbf{r}) \rangle$. By plugging the result on Eq. (4.8), we find that the total energy accounting for the first anharmonic correction is given by [141]:

$$E = 3m\omega_i^2 \langle r_i^2 \rangle - \frac{15m^2\omega_i^4}{8U_0} \langle r_i^4 \rangle, \tag{4.16}$$

where U_0 is the trap depth. To estimate the anharmonic contribution, we calculate the fourth moment of the density distribution of Eq. (4.1), which is found to be:

$$\langle r_i^4 \rangle = \frac{3}{16} N R_i^4 \frac{\mathrm{Li}_5\left(-e^{q_0}\right)}{\mathrm{Li}_3\left(-e^{q_0}\right)}. \tag{4.17}$$

By assuming a trap depth of $1.5\,\mu$K, the correction produced by the anharmonic term is found to be less than 10% in our experimental condition, small enough to be neglected for the temperature estimation.

The three presented thermometry methods provide consistent results. The final values of T/T_F reported in the rest of the chapter are obtained from a weighted average of the three methods results. The uncertainty over the degeneracy is set to ± 0.01, that corresponds to the mean observed deviation among the different methods. For datasets at very low temperatures, namely for $T/T_F \lesssim 0.1$, where the phenomenological fit is known to become inaccurate we consider only the weighted average of the other two methods for determining the final value of T/T_F.

4.1.2 Thermometry of crossover gases away from unitarity

Away from unitarity, the equation of state of strongly interacting gases is unknown and the thermometry is a hard task. We estimate the temperature of crossover gases at $1/k_F a \neq 0$ by measuring that of the corresponding UFG, before the magnetic field ramp is applied. In fact, to produce crossover gases, we always perform the evaporation at resonance and only at the end of it we tune the interaction strength via a 50 ms sweep of the Feshbach field. As the explored crossover region of $|1/k_F a| \lesssim 0.5$ is very close to unitarity, the magnetic field sweep is adiabatic, which we verify by measuring that the UFG temperature remains unchanged after a closed loop of the magnetic field ramp. According to Ref. [41], when varying the interaction strength at constant T/T_F, the entropy remains constant in the BCS side up to unitarity, and it monotonically decreases for $1/k_F a > 0$. Therefore, the temperature of the gas is constant during an adiabatic sweep of the Feshbach field towards the BCS side of the resonance. On the other hand, when moving towards the BEC limit, the temperature of the cloud increases to keep the entropy constant during the adiabatic process, as the entropy is a monotonically increasing function of the temperature for given interaction strength [41]. Therefore, by measuring T/T_F of the unitary cloud before the sweep, we have an exact estimation of the temperature of crossover gases in the BCS side, and a lower bound for that of gases in the BEC one.

4.2 Temperature induced dc Josephson breakdown

With the procedure described in the previous section we create strongly-interacting atomic junctions at finite temperature. Their response to an injected external current is then investigated by following the same protocol described in Sec. 3.1.2. In particular, we employ the 6 DMD mirrors barrier presented in Sec. 3.1.1 to create the junction, and we refer to the same section for the characterization of it. As for the low temperature junctions presented in the previous chapter, we acquire the full current-chemical potential characteristic at a given temperature, by injecting a controlled current I_{ext} via a constant velocity translation of the repulsive barrier. At the end of the barrier movement, we measure the developed chemical potential difference $\Delta\mu$ across the junction, by determining the particle imbalance in the reservoirs from the *in-situ* density profile. In Fig. 4.4 we report the $I - \Delta\mu$ characteristics obtained for a unitary junction at increasing temperature. At low T, the plateau at $\Delta\mu \simeq 0$ identifies the dc Josephson regime for injected current $|I_{\text{ext}}| < I_{s,\max}$ (blue diamonds), where $I_{s,\max}$ is the maximum Josephson supercurrent, that plays the role of the critical current I_c at finite temperature. As we increase T, the plateau is found to shrink (violet squares) until it completely vanishes (red circles), the $I - \Delta\mu$ characteristic turning from highly non-linear to Ohmic as for a fully resistive junction. As reported in the right panels, at high temperature a lower injected current is sufficient to develop a finite $\Delta\mu$ across the junction, reflected by an increase of the density in the compressed reservoir, namely $I_{s,\max}$ decreases for increasing temperature. The curves are fitted by

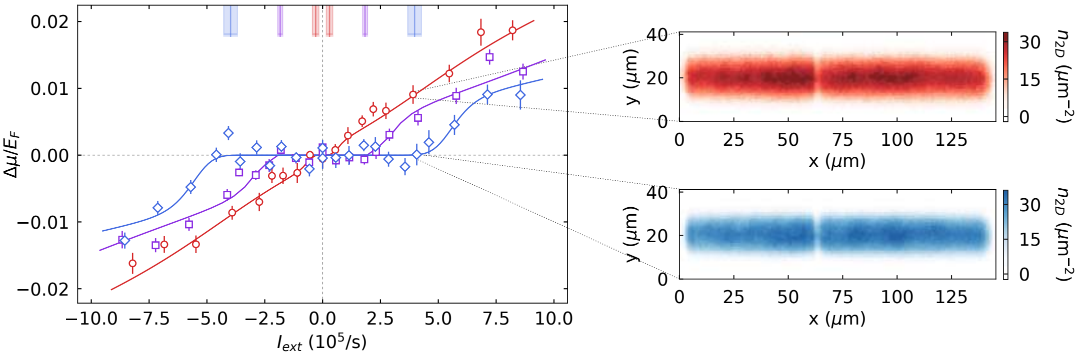

Figure 4.4: $I - \Delta\mu$ characteristics and relative fit with RCSJ-circuit model for atomic junctions at unitarity ($1/k_F a \simeq 0$) at $T/T_F = 0.08(1)$ (blue diamonds), $T/T_F = 0.15(1)$ (purple squares) and $T/T_F = 0.18(1)$ (red circles). Confidence intervals for $I_{s,\max}$ obtained from the RCSJ-circuit model fit are reported as shaded regions on the top x-axis. Data-point errorbars denote the standard deviation of mean over an average of about 10 experimental realizations. On the right: *in-situ* density profiles acquired for the two highlighted points in the left figure, after the injection of a current $I_{\text{ext}} \simeq 3.9 \times 10^5$ s^{-1}. Both images represent the average over about 10 experimental realizations.

employing the RCSJ-circuit model already presented in Sec. 3.2.2, calculating E_c at finite temperature from the equation of state of a unitary gas, and keeping $I_{s,\max}$ and the conductance G as the only free parameters. The confidence intervals for $I_{s,\max}$ obtained from the fits of data reported in Fig. 4.4 are represented as shaded regions on the top x-axis. By varying the junction temperature across the superfluid transition, we obtain the full characterization of the maximum supercurrent $I_{s,\max}$ as a function of the temperature of a unitary Fermi gas, as reported further below. We refer instead to Sec. 4.3 for the discussion on the normal conductance at finite T. Finally, we remark that, contrarily to Chapter 3, all the transport properties discussed throughout this chapter refer to single fermion quantities, instead of pair quantities. In particular, we employ $V_{0,F} = V_{0,B}/2$ and $\mu_{0,F} = \mu_{0,B}/2$, avoiding the subscript $_F$ to ease the notation.

4.2.1 Maximum supercurrent at finite temperature

The measured maximum Josephson supercurrent $I_{s,\max}$ of a unitary junction as a function of its temperature is plotted in Fig. 4.5. As suggested by the vanishing dc Josephson plateau in the $I - \Delta\mu$ curves for increasing temperature, $I_{s,\max}$ presents a decreasing trend approaching the critical temperature T_c, that qualitatively resembles the one predicted in BCS theory by the Ambegaokar-Baratoff formula of Eq. (1.38). However, such a formula is not expected to hold in the strongly-interacting regime [99], and thus to represent the observed behavior of $I_{s,\max}$ we employ a finite temperature extension of the theory model presented in Sec. 3.3.1, which links the Josephson supercurrent to the condensed density of the superfluid. In particular, we account for the two lowest order contributions to the supercurrent, I_1 and I_2, which are calculated following Eqs. (3.15) and (3.20) respectively. We numerically integrate their expressions

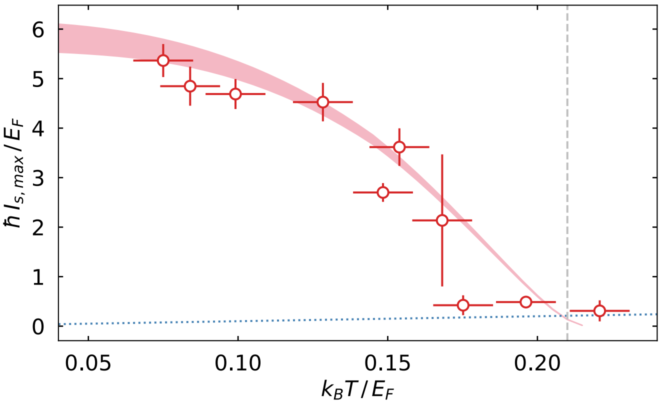

Figure 4.5: Maximum Josephson supercurrent $I_{s,\max}$ of a unitary junction as a function of temperature. Vertical errorbars combine the fitting error with the statistical one averaging typically 2 experimental realizations. The shaded region indicates the calculated $I_{s,\max}$ with our theory model, considering a 10% uncertainty around the nominal barrier width and a 3.5% uncertainty on the calculated E_F. The barrier height is fixed at $V_0/\mu_0 \simeq 0.7$, where $\mu_0 \approx \sqrt{\xi}\, E_F$. The critical temperature for the superfluid transition of $T_C = 0.21\, T_F$ is signaled by the gray dashed line. Blue dotted line identifies the thermal energy k_BT/E_F, rescaled by the Fermi energy, needed for thermal phase slips to activate.

by employing the unitary EoS at finite temperature for the pair chemical potential $\mu(\mathbf{r})$ and the density $n(\mathbf{r})$ per spin state, described by Eq. (4.4) and (4.5), respectively. Moreover, we use the condensate fraction λ_0 of a homogeneous unitary Fermi gas at finite temperature, obtained with the non-perturbative Luttinger-Ward technique of Ref. [41] that predicts a critical temperature of $T_c^h \simeq= 0.16\, T_F$ (see Fig. 4.6). In particular, the local condensed fraction $\lambda_0(\mathbf{r})$ of the trapped gas is calculated by defining a local degeneracy parameter $k_BT/\epsilon_F(\mathbf{r})$, where $\epsilon_F(\mathbf{r}) = \hbar^2/(2m)(6\pi^2 n(\mathbf{r}))^{2/3}$ is the local Fermi energy. In fact, as it will be discussed in detail in Sec. 4.2.2, the density inhomogeneity of our trapped samples causes the local degeneracy to largely vary throughout the cloud at high T, an effect taken into account by considering a locally varying condensed fraction $\lambda_0(\mathbf{r}) = \lambda_0(k_BT/\epsilon_F(\mathbf{r}))$. Furthermore, for the calculation of the tunneling amplitude $|t(\mu(\mathbf{r}), V_0)|$ we adopt the Eckart approximation already discussed in Sec. 3.3.1, accounting also for the barrier width expansion along the z propagation direction. Finally, by combining the I_1 and I_2 contributions according to Eq. (3.21), we obtain the maximum Josephson supercurrent plotted as shaded region in Fig. 4.5. In particular, we consider a 10% uncertainty on the nominal barrier width of $w_0 = 0.95\,\mu$m and a 3.5% uncertainty on the Fermi energy E_F, reflecting the statistical error in number of atoms and trap frequencies estimation.

With no free parameters, our theory model quantitatively reproduces the experimental data, highlighting that the connection between the maximum Josephson supercurrent and the condensed density holds even at finite temperature. Some discrepancies appears however once the critical temperature T_c is approached: while the calculated $I_{s,\max}$ vanishes at $T_c = 0.21\, T_F$, the measured one presents values consistent with zero

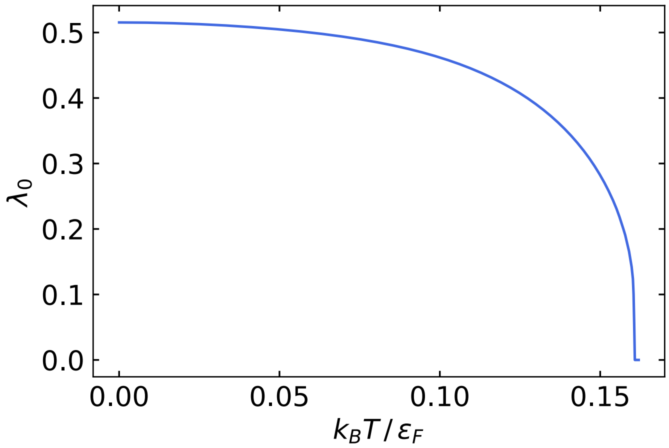

Figure 4.6: Condensed fraction of a homogeneous unitary Fermi gas as a function of temperature, calculated with the non-perturbative Luttinger-Ward formalism of Ref. [41].

already for lower temperatures. Such a deviation can be due to the radial inhomogeneity of the junction, that causes different shells of the cloud to undergo the superfluid transition at different temperature, as it will be discussed in depth in Sec. 4.2.2. Furthermore, a finite chemical potential difference $\Delta\mu$ at $T < T_c$ could develop from thermal fluctuations in the superfluid state [90, 142]. In particular, stochastic thermal phase slips are expected to become relevant when $\hbar I_{s,\max} \simeq k_BT$, since their probability scales as $\exp(-2\hbar I_{s,\max}/k_BT)$ [142]. The rescaled thermal energy k_BT/E_F of our system is plotted in Fig. 4.5 as the dotted blue line, which becomes of the order of $\hbar I_{s,\max}$ around $T \simeq 0.17\,T_F$, together with the observed drop in the maximum Josephson current. At this temperature indeed, thermal phase slips can provide a source of dissipation, not included in out theory model, that may cause the vanishing of $I_{s,\max}$.

4.2.2 Estimation of local quantities

For the calculation of $I_{s,\max}$ we employ the unitary Fermi gas EoS to describe the local quantities of $\mu(\mathbf{r})$, $n(\mathbf{r})$ and $k_BT/\epsilon_F(\mathbf{r})$. The fact that, as discussed in Sec. 4.1.1, the measured one-dimensional density profile can be well fitted with the EoS is a hint that such an assumption is well funded, as we further confirm by accessing the local 3D density of the cloud $n(x, y, z)$. Such quantity is not directly measured by means of absorption imaging, that provides instead its integration along the imaging direction z, i.e. the two-dimensional density $n_{2D}(x, y)$. The 3D density can be anyway reconstructed by means of the inverse Abel transformation. In fact, under the assumption of elliptical symmetry, valid in our crossed trap where $\omega_z \simeq \omega_y$, the local 3D density can be calculated as:

$$n(x, r) = -\frac{1}{\pi}\int_r^{+\infty} \frac{dn_{2D}(x, y)}{dy}\frac{dy}{\sqrt{y^2 - r^2}}, \tag{4.18}$$

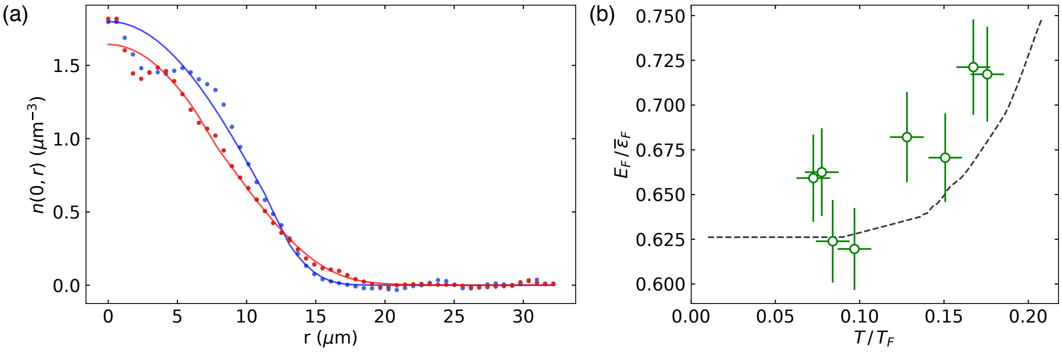

Figure 4.7: Estimation of local quantities. (a) Radial profiles of the reconstructed 3D density with Abel transformation of a unitary cloud at $T/T_F = 0.08(1)$ (blue points) and $T/T_F = 0.18(1)$ (red points). Both reconstructed trends are well represented by the calculated density profiles with Eq. (4.5) (solid lines), using no free parameter and assuming the same number of atoms and trap frequencies of our experimental conditions. (b) Comparison between the measured (green circles) and calculated with EoS (dashed line) rescaling factor $E_F/\bar{\epsilon}_F$ from local to trap averaged quantities. Here, $\bar{\epsilon}_F$ is the density weighted Fermi energy inside the volume spanned by the barrier translation defined by Eq. (4.19).

where $r = \sqrt{y^2 + z^2}$ is the radial coordinate. By performing the above transformation on the acquired n_{2D} of the gas in the crossed ODT, we reconstruct the local density reported in Fig. 4.7 for a unitary gas at $T/T_F = 0.08(1)$ (blue circles) and $T/T_F = 0.18(1)$ (red circles). In particular, we employ a pre-built Python function based on the Hansen-Law method to perform a fast and reliable inverse Abel transformation [143]. We compare the obtained local densities with the ones calculated with no free parameter via the unitary gas EoS, which are reported in Fig. 4.7 (a) as solid lines for the two temperatures, respectively. In particular, we employ Eq. (4.5) for the 3D density and calculate the chemical potential μ_0 at finite temperature by constraining atom number and trap frequencies to the experimentally measured ones (see Fig. 4.3 (a)). The agreement between experimental and calculated density profiles is extremely good especially on the wings of the cloud, confirming that the density profile of our unitary cloud is well described by the density EoS. Deviations between the two profiles are observed only close to the trap center, where the reconstructed density is affected by unavoidable noise from the inverse Abel transformation.

The reconstructed local density opens the access to the local Fermi energy $\epsilon_F(\mathbf{r}) = \hbar^2/(2m)(6\pi^2 n(\mathbf{r}))^{2/3}$, that allows for the conversion of all trap-averaged thermodynamic quantities presented so far in terms of local quantities. In our case, a convenient rescaling factor for local quantities employs the density-weighted Fermi energy $\bar{\epsilon}_F$ inside the volume spanned by the barrier translation $\mathcal{V}_b$, namely:

$$\bar{\epsilon}_F = \frac{\int_{\mathcal{V}_b} d^3\mathbf{r}\, \epsilon_F(\mathbf{r})\, n(\mathbf{r})}{\int_{\mathcal{V}_b} d^3\mathbf{r}\, n(\mathbf{r})}. \tag{4.19}$$

In particular, we define $\mathcal{V}_b$ as the volume delimited by a cylinder of height $\delta x = 10\,\mu$m and radius $r_b = 6\,\mu$m leaning on the $x = 0$ plane, where the barrier is placed at the

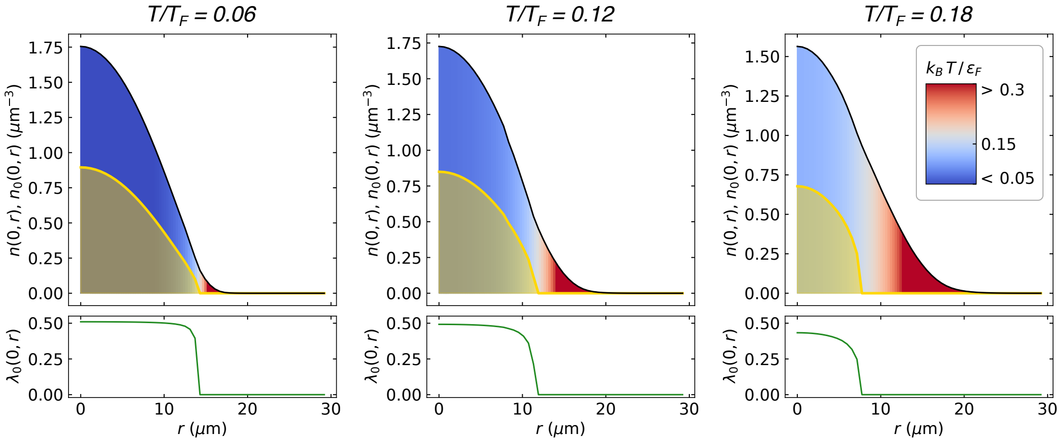

Figure 4.8: Radial density profile $n(0,r)$ (black solid line) of a unitary Fermi gas at different temperatures calculated by assuming the EoS of Eq. (4.5), with number of atoms and trap frequencies fixed by our experimental conditions. The color of each radial shell reflects the local degeneracy $k_BT/\epsilon_F(0,r)$ according to the legend on the right most figure. The local radial condensed density $n_0(0,r)$ (yellow solid line) is obtained by multiplying $n(0,r)$ times the local condensed fraction $\lambda_0(0,r) = \lambda_0(k_BT/\epsilon_F(0,r))$, which is plotted for each temperature in the bottom graph as solid green line. We employ LDA on the Luttinger-Ward formalism results of Fig. 4.6 for estimating $\lambda_0(k_BT/\epsilon_F(0,r))$.

beginning of the translation. Our choice represents a trade-off between a sufficiently small volume to express local information, and a sufficiently large one to average out the typical noise in the Abel reconstructed profile. The rescaling factor from local to trap averaged quantities is thus given by $E_F/\bar{\epsilon}_F$, the measured value of which is reported in Fig. 4.7 (b) for datasets at different temperature, together with the calculated one with the EoS, shown as the dashed line. The agreement between experimental points and calculated profile confirms once more that all local thermodynamic quantities in our experiment can be obtained by assuming the density profile of the EoS in Eq. (4.5), plugging in the formula the trap-averaged quantities relevant for our experimental conditions, i.e. total atom number and trap frequencies.

The possibility to approximate the density profile of our unitary cloud with the one of Eq. (4.5) allows for the calculation of the expected condensed density of the cloud, as reported in Fig. 4.8. In fact, the local Fermi energy $\epsilon_F(\mathbf{r})$ calculated from the density $n(\mathbf{r})$ sets the local degeneracy of the cloud $k_BT/\epsilon_F(\mathbf{r})$, that is represented in the figure by the color of each radial shell. By employing LDA, we can associate to each shell at constant $k_BT/\epsilon_F(\mathbf{r})$ a local condensed fraction $\lambda_0(k_BT/\epsilon_F(\mathbf{r}))$, that is used to calculate $I_{s,\max}$ with our theory model. As visible from the bottom graphs of Fig. 4.8, the condensed fraction is almost constant inside the unitary cloud at the lowest temperature, while it varies non negligibly as the temperature is increased. Once the local condensed fraction is known, the condensed density is simply calculated as $n_0(\mathbf{r}) = \lambda_0(k_BT/\epsilon_F(\mathbf{r})) \times n(\mathbf{r})$, and plotted as yellow solid line in the figure.

The flatness of $\lambda_0(0,r)$ for the $T/T_F = 0.06$ case is the reason why the density-weighted condensed fraction measured in Chapter 3 is found to be consistent with the theoretically predicted condensed fraction of a homogeneous system, as $\lambda_0(\mathbf{r})$ is almost constant inside the cloud. Furthermore, the fact that $\lambda_0(0,r) \simeq 0.51$ through all the radial profile justifies the assumption of considering the low temperature junctions of Chapter 3 as zero-temperature systems. On the other hand, as temperature is increased, the condensed density gets depleted, and consequently the maximum Josephson supercurrent decreases. In particular, for the highest temperature of $T/T_F = 0.18$ presented in Fig. 4.8, where the measured $I_{s,\max}$ is already consistent with zero, the condensed density is observed to vanish at less than $10\,\mu$m distance from the center of the cloud. The large contribution of non-condensed particles to the transport may explain why we observe a vanishing $I_{s,\max}$ even below the critical temperature of $T_c/T_F = 0.21$. In fact, according to our theory model, only the condensed part of the cloud contributes to the superflow, whereas the non-condensed one shows a resistive behavior and develops a finite chemical potential difference. As soon as the developed $\Delta\mu$ is above our experimental resolution, namely when the non-condensed part is large enough to produce a measurable relative imbalance $z - \bar{z} \neq 0$ after the barrier movement, we observe a vanishing $I_{s,\max}$ even for a finite condensed fraction system. This limit of our experimental procedure could explain the discrepancy with our theory model for $T/T_F \gtrsim 0.17$. In fact, the maximum Josephson supercurrent of our theory model is calculated as the sum of all the radial contribution, which is thereby non zero as long as there is a finite condensed density in the cloud, namely until $T_c/T_F = 0.21$. On the other hand, our experimental procedure reveals the averaged $I - \Delta\mu$ curve over all the radial shells, which presents a non-zero $\Delta\mu$, and thus a vanishing $I_{s,\max}$, as soon as the non-condensed part of the cloud provides a $z - \bar{z} \neq 0$ above resolution. In principle, this issue could be overcome by measuring the local $I - \Delta\mu$ characteristic of each radial shell. To do that, we could perform an inverse Abel transformation on the *in-situ* density profiles of the junction, define a set of sufficiently thin radial shells to acquire the local $I - \Delta\mu(\mathbf{r})$ characteristic and finally extract $I_{s,\max}$ as the sum of the maximum supercurrents of the different shells. Such a procedure might corrects the measured values of maximum Josephson supercurrent, but it is valid only under the assumption that each radial shell contributes to the transport independently from the others. However, because of radial oscillations in our harmonic trap presenting a period of $1/300\,\mathrm{Hz} \simeq 3$ ms, comparable with the barrier translation duration at the lowest velocities, radial shells share particles among each others, and the radial sum is practically meaningless.

4.2.3 Critical temperature of Josephson breakdown

The effect of radial inhomogeneity of the cloud discussed in the previous subsection, together with the possible occurrence of thermal phase slips for $T/T_F \gtrsim 0.17$, causes the maximum Josephson supercurrent $I_{s,\max}$ to vanish at a temperature $T_0 < T_c$. We can extract such a critical temperature for the dc Josephson breakdown from a phe-

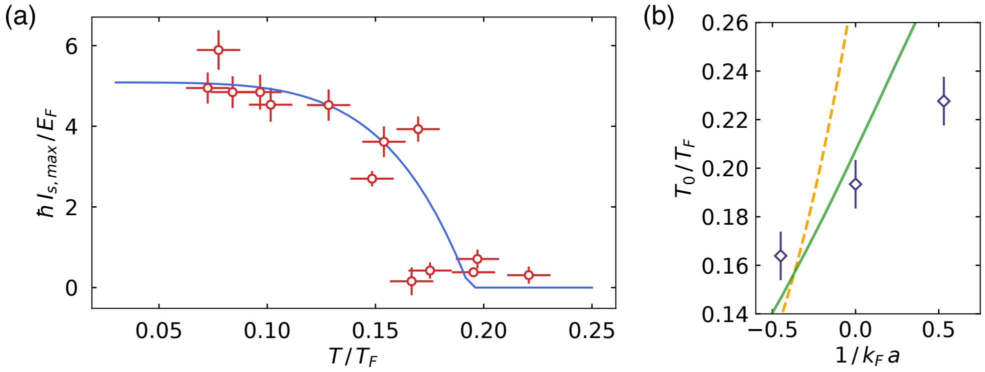

Figure 4.9: Critical temperature of dc Josephson breakdown. (a) Fit of measured $I_{s,\mathrm{max}}$ for a unitary junction with the function in Eq. (4.20). The extracted fit parameters are reported in Table 4.1. (b) Critical temperature of dc Josephson breakdown T_0 as a function of the interaction strength $1/k_F a$. The measured values, reported as dark blue diamonds, are compared with the critical temperature of the superfluid transition for harmonically trapped crossover gas of Ref. [134] (solid green line) and the critical temperature by BCS theory of Eq. (1.21) (dashed orange line).

nomenological fit of the observed $I_{s,\mathrm{max}}(T)$ trend with the piece-wise function:

$$I\left(T\right) = I_0 \left[1 - \left(\frac{T}{T_0}\right)^{\alpha}\right] \times \theta\left(T - T_0\right). \tag{4.20}$$

By keeping I_0, α and T_0 as free parameter, the above function is observed to well match the measured behavior, as illustrated by Fig. 4.9 (a) for a unitary gas. In particular, we obtain $T_0 = 0.19(1)\,T_F$, consistently with what expected from thermal phase slips. By performing an analogous characterization of $I_{s,\mathrm{max}}$ for crossover gases slightly away from unitarity, we obtain the trend of T_0 as a function of the interaction strength reported in Fig. 4.9 (b). In particular, each value of T_0 is obtained by fitting with Eq. (4.20) the $I_{s,\mathrm{max}}(T)$ characteristic at a given interaction strength, providing the fitting results listed in Table 4.1. The extracted value of I_0 are consistent with the zero temperature trend observed in the measurement reported in Chapter 3, despite the large uncertainty on the value at $1/k_F a = 0.53$. We note that such uncertainty, together with those on the values of the phenomenological α parameter, do not affect the critical temperature T_0, which is signaled by a clear drop of the maximum Josephson supercurrent at any interaction strength. As already discussed, the estimated values of T_0 provide a lower bound for the critical temperature of the superfluid transition. The observed monotonic trend is consistent with the theoretical prediction of Ref. [134], reported as green solid line in Fig. 4.9 (b), where the critical temperature of a harmonically trapped cloud in the crossover is calculated with a fully self-consistent t-matrix approach. We note that the monotonicity of the observed trend is not affected by the incorrect temperature estimation of the $1/k_F a = 0.53$ gas, the real temperature of which is expected to be higher than the reported one, as already discussed in Sec. 4.1.1.

Table 4.1: Results of the phenomenological fit with Eq. (4.20) of the measured $I_{s,\max}$ trend versus T/T_F, for three different interaction strengths $1/k_Fa$ in the BEC-BCS crossover regime.

$1/k_Fa$	$\hbar I_0/E_F$	T_0/T_F	α
-0.45	2.7(2)	0.164(10)	34(43)
0	5.1(4)	0.193(10)	5(2)
0.53	4.8(11)	0.228(10)	2(1)

4.3 Conductance across the superfluid transition

The $I - \Delta\mu$ characteristic also addresses the resistive behavior of current-biased atomic junctions. For $|I_{\text{ext}}| > I_{s,\max}$, the non-zero chemical potential difference indeed signals the presence of a finite conductance G, that we directly extract from the RCSJ-circuit model fit. So far, we focused our attention on the dc part of the characteristic, pointing out how the maximum Josephson supercurrent $I_{s,\max}$ is directly connected to the condensate density of the superfluid even at finite temperature. In this section, we move our attention to the normal conductance of the junction, exploring its properties at finite temperature across the superfluid transition. Remarkably, also the conductance is found to be affected by the presence of a condensed state, featuring a large anomalous contribution, which dominates at low temperature and decreases for increasing T/T_F, as discussed in detail in Sec. 4.3.1. Furthermore, the investigation of the conductance scaling with the barrier properties at finite temperature provides information about the nature of the normal current carriers. As discussed in Sec. 4.3.2, the conductance scaling is sensitive to whether transport is mediated by pairs or unpaired fermions, allowing us to elucidate the character of the carriers across the superfluid transition.

4.3.1 Anomalous contribution to the normal conductance

From the RCSJ-circuit model fit of the acquired $I - \Delta\mu$ characteristics at finite temperature, we extract the normal conductance of a unitary junction, reported as green diamonds in Fig. 4.10. G is observed to decrease monotonically for increasing temperature, its values ranging from $10^4\,h^{-1}$ at the lowest T/T_F to $10^3\,h^{-1}$ for the highest. Throughout the range of explored temperatures, G greatly exceeds the conductance $G_0 = 102(15)\,h^{-1}$ measured for a non-interacting spin-polarized Fermi gas at $T/T_F = 0.21(1)$ and same E_F, reported as the red square point in Fig. 4.10. This behavior is clearly different from the typical one revealed in the superconducting case, where the resistive branch of the current-voltage characteristic is determined by the normal-state conductance G_n, i.e. the conductance of a junction composed by normal metals at $T > T_c$. Therefore, the normal conductance G_n simply corresponds to the junction conductance in the case of ideal fermionic reservoirs, that for atomic junctions is given by a non-interacting Fermi gas junction, as the one that has been probed to extract G_0. To further confirm the deviation of the measured unitary conductance G from the normal G_0, we calculate the expected value of the latter by paralleling the

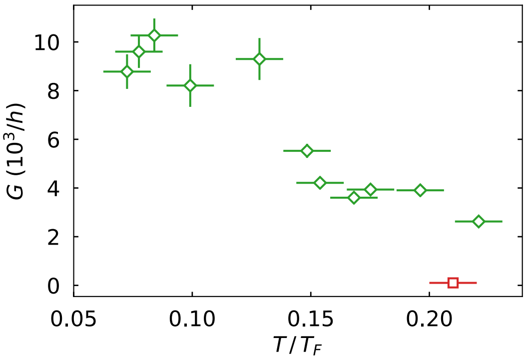

Figure 4.10: Normal conductance G as a function of the reduced temperature T/T_F, measured at unitarity under the same experimental conditions of Fig. 4.5 (green diamonds). The conductance per spin component $G_0 = 102(15)\, h^{-1}$ of a non-interacting Fermi gas is reported as the red square. The measurement of G_0 is performed on a spin-polarized Fermi gas at $T/T_F = 0.21(1)$ with an equivalent barrier height $V_0/\mu_0 \simeq 0.73$. Vertical error bars combine the standard error on the extracted conductance with statistical errors from averaging typically 2 independent measurements.

non-interacting atomic junction with a metal-insulator-metal (M-I-M) one. By considering a non-interacting electron model, the current density through a zero-temperature homogeneous M-I-M junction can be expressed as [144]:

$$j_n = \frac{2\,e}{h} \int_{E_F - eV}^{E_F} dE \int_0^E dE_\parallel\, \rho_\parallel\, |t(E - E_\parallel)|^2, \tag{4.21}$$

where the factor 2 accounts for the number of spin states, V is the potential difference across the junction, E_F and $\rho_\parallel = m/(2\pi\hbar^2)$ are its Fermi energy and density of states, respectively, and $|t(E)|^2$ is the probability for one electron of energy E to tunnel through the insulating barrier. Here, the subscript $_\parallel$ indicates the plane parallel to the barrier and orthogonal to the propagation direction of the particle flow. The above expression can be translated into the atomic junction formalism by considering that in the ideal Fermi gas case the current is produced by the flow of neutral particles tunneling through the barrier with probability $|t(E)|^2$, the chemical potential difference $\Delta\mu$ playing the role of the voltage. The atomic current density per single spin state of an ideal zero-temperature junction is thus given by:

$$j_n = \frac{1}{h} \frac{m}{2\pi\hbar^2} \int_{E_F - \Delta\mu}^{E_F} dE \int_0^E |t(E - E_\parallel, V_b)|^2\, dE_\parallel, \tag{4.22}$$

where V_b is the barrier height. In the limit of $\Delta\mu \to 0$, namely within the linear response regime, j_n scales linearly with the chemical potential difference:

$$j_n = \frac{1}{h} \frac{m}{2\pi\hbar^2} \int_0^{E_F} dE_\parallel\, |t(E - E_\parallel, V_b)|^2\, \Delta\mu, \tag{4.23}$$

so that the normal-state conductance per unit area is readily evaluated as $g_n = j_n/\Delta\mu$:

$$h\, g_n = \frac{m}{2\pi\hbar^2} \int_0^{E_F} dE_\parallel\, |t(E - E_\parallel, V_b)|^2. \tag{4.24}$$

The previous result, holding for a homogeneous system, can be extended to our trapped case within LDA. Defining a local Fermi energy $\epsilon_F(r,0) = \frac{\hbar}{2m}(6\pi^2 n(r,0))^{2/3}$ in each position $(r, x=0)$ of the gas at the barrier, the local conductance per unit area can be written as:

$$h\, g_n(r) = \frac{m}{2\pi\hbar^2}\int_0^{\epsilon_F(r,0)} dE_\parallel\, |t(\epsilon_F(r,0) - E_\parallel, V_b)|^2. \tag{4.25}$$

Finally, the total conductance of the junction G_n is calculated by integrating the local $g_n(r)$ over the radial direction:

$$G_n = \int_0^{R_\perp} g_n(r)\, 2\pi r\, dr, \tag{4.26}$$

where $R_\perp$ is the radial Thomas-Fermi radius of the cloud. We numerically solve the previous integral to evaluate G_n, employing the Eckart barrier approximation to calculate the transmission coefficient $|t(E, V_b)|^2$, and accounting for the Gaussian divergence of the barrier profile along its propagation direction, as done for the maximum supercurrent calculation. By considering a ±5% uncertainty on the nominal Eckart barrier width d, we obtain $G_n = 160(29)\, h^{-1}$, in reasonable agreement with the measured G_0 of a non-interacting spin-polarized Fermi gas. Despite the previous expression of G_n being strictly valid only at $T = 0$, we note that the conductance is marginally affected by finite temperature effects as long as $k_B T \ll E_F$, V_b, and the zero-temperature calculated value is in fact comparable with the measured one on an ideal Fermi gas at $T/T_F \simeq 0.21$.

We note that an identical expression for the nomal-state conductance can be retrieved from microscopical BCS theory. In particular, by following Ref. [100], in the limit of strong barrier of $|t|^2 \ll 1$, the critical current density of a zero-temperature junction is given by:

$$j_c = \frac{\Delta_0}{2}\frac{m}{2\pi\hbar^3}\int_0^{E_F} |t(E_F - E_\parallel)|^2 dE_\parallel, \tag{4.27}$$

where Δ_0 is the gap of the BCS superfluid. The total conductance per unit area can be retreived by plugging the above expression into the Ambegaokar-Baratoff relation of Eq. (1.38), obtaining:

$$h g_n^{\text{BCS}} = \frac{m}{\pi\hbar^2}\int_0^{E_F} |t(E_F - E_\parallel)|^2\, dE_\parallel. \tag{4.28}$$

The previous expression accounts for the transport of both spin state, whereas we measured G_0 of a spin polarized ideal gas, i.e. $g_n^{\text{BCS}} = 2g_n$. By dividing the previous expression by 2, an expression for g_n identical to Eq. (4.24) is obtained, confirming that the normal state conductance expected for a BCS superfluid junction coincides with the one of Eq. (4.26).

The conductance we measure for a unitary Fermi gas is therefore much higher than both the measured G_0 and the calculated G_n normal conductance throughout the range of temperature explored. Such a mismatch indicates that normal currents in our unitary junction do not arise from incoherent pair or quasi-particle tunneling, that provide

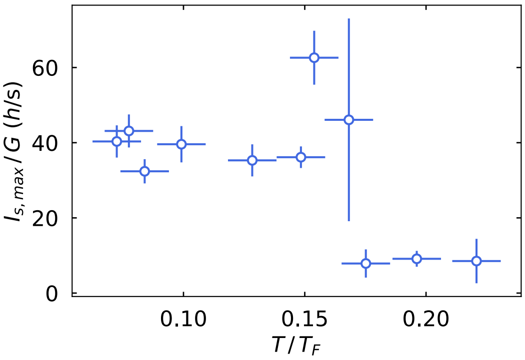

Figure 4.11: Experimentally obtained ratio between the Josephson maximum supercurrent $I_{s,\max}$ and the normal conductance G, reported in Fig. 4.5 and Fig. 4.10, respectively.

the main contribution to resistive transport in superconducting junction, but rather from collective bosonic excitations. In particular, the finite large values of the measured conductance of the unitary junction at low temperature suggests the presence of an anomalous contribution to G, directly connected to the condensed fraction, in agreement with measurements presented in Sec. 3.4. As already discussed in Sec. 1.4.3, the anomalous contribution arises from the tunneling of condensed particles, which are coherently converted into phononic excitations, represented by Bogoliubov-Anderson modes in fermionic superfluids. The anomalous contribution is instead absent in superconducting junctions, as Coulomb interaction turns such excitations into gapped plasma modes.

We further confirm the presence of a contribution in G directly proportional to the condensed density by comparing the ratio of measured $I_{s,\max}/G$ at different temperatures. As illustrated by Fig. 4.11, this ratio is approximately constant for all the non-zero values of maximum Josephson supercurrent, demonstrating the relation between conductance and condensate density. Therefore, the depletion of the condensate at high T causes the monotonically decreasing trend of G. After dropping by nearly an order of magnitude from its maximum because of the anomalous contribution vanishing, G shows no distinct feature across the superfluid transition, remaining much larger than G_0 also for $T > Tc$. We ascribe such an enhanced transport above critical to the hydrodynamic behavior of unpaired fermions at unitarity, that admits incoherent tunneling of sound modes even in the non-superfluid state [145, 146]. Contrarily, the collisionless character of a non-interacting Fermi gas does not allow any collective mode, and the normal conductance G_0 consists of single-particle contribution only. Finally, the finite-T contribution due to incoherent tunneling of thermally populated phonons is expected to grow as T^4, as already discussed in Sec. 1.4.3, providing a monotonically increasing trend of the conductance for higher temperatures. However, the relative weight of the anomalous and phononic terms is a theoretical challenge, but we expect the unitary gas conductance to approach that of a non-interacting gas at the same temperature for $T \gg T_c$.

4.3.2 Conductance scaling with barrier properties

By investigating the conductance behavior in dependence on the barrier properties we can determine whether the transport is mediated by single fermions or bosonic pairs. As discussed in Sec. 1.4.3, for a zero-temperature bosonic Josephson junction, the resistive term arises only as a second order process, ensuring the conductance to be proportional to the bosonic tunneling probability $|t_B|^2$. The same proportionality has been observed to hold in our unitary condensate at low temperature, as confirmed by the $G^{1/2} \propto I$ trend, already presented in Fig. 3.17. Therefore, as long as the gas is paired, we expect the conductance of a fermionic superfluid to be proportional to the tunneling probability of pairs, namely $G \propto |t_B|^2$. On the other hand, well above T_c where the gas is certainly composed by unpaired fermions, G is expected to account for the single fermions tunneling probability $|t_F|^2$, as for G_n of a non-interacting Fermi gas of Eq. (4.24). For increasing temperature, the conductance may thus turn from being proportional to $|t_B|^2$, as long as pairs provide the main contribution to normal transport, to $G \propto |t_F|^2$ when carriers are composed by single fermions. Since the dependence of the two bosonic and fermionic tunneling coefficients on the barrier properties is quantitatively different, the investigation of the G scaling with barrier height and size allows us to gain valuable information about the nature of the carriers in our system.

To analyze the scaling of the tunneling amplitude, we can employ the Eckart barrier approximation, as done for the calculation of $I_{s,\max}$ with our theory model. Under such condition, the tunneling probability $T = |t|^2$ for a generic particle of mass M and energy ϵ to tunnel though a barrier of height V and Eckart size d can be analytically expressed according to Eq. (3.19). In the tunneling limit of $V/\epsilon_b \gg 1/8$ and ϵ/ϵ_b, where $\epsilon_b = \hbar^2/(Md^2)$ is the characteristic energy of the barrier, the tunneling probability can be approximated with:

$$|t(\epsilon)|^2 \simeq \exp\left(2\pi\sqrt{\frac{2\epsilon}{\epsilon_b}}\right) \times \exp\left(-2\pi\sqrt{\frac{2V}{\epsilon_b}}\right). \tag{4.29}$$

By introducing the Fermi energy $E_F = \hbar^2 k_F^2/(2m)$, where m is the mass of one ^{6}Li atom, the logarithm of the tunneling probability reads:

$$\log|t(\epsilon)|^2 \simeq -2\pi\sqrt{\frac{M}{m}}\, k_F d \left(\sqrt{\frac{V}{E_F}} - \sqrt{\frac{\epsilon}{E_F}}\right). \tag{4.30}$$

It becomes thus clear that bosonic ($M = 2\,m$, $V = 2\,V_F$, $\epsilon = 2\,\epsilon_F$) and fermionic ($M = m$, $V = V_F$, $\epsilon = \epsilon_F$) tunneling probabilities are connected by the relation: $\log|t_B|^2 \simeq 2\log|t_F|^2$. Since $G \sim |t|^2$ both in the bosonic and the fermionic case, a similar factor of approximately 2 is expected to appear in the scaling of the conductance, whether the non-zero conductance in enabled by pairs or single fermions.

In order to gain information about the carrier nature, we therefore measure the conductance scaling with the barrier parameters that determine the tunneling amplitude: its height V_0 and size d, that we conveniently recast into the adimensional barrier

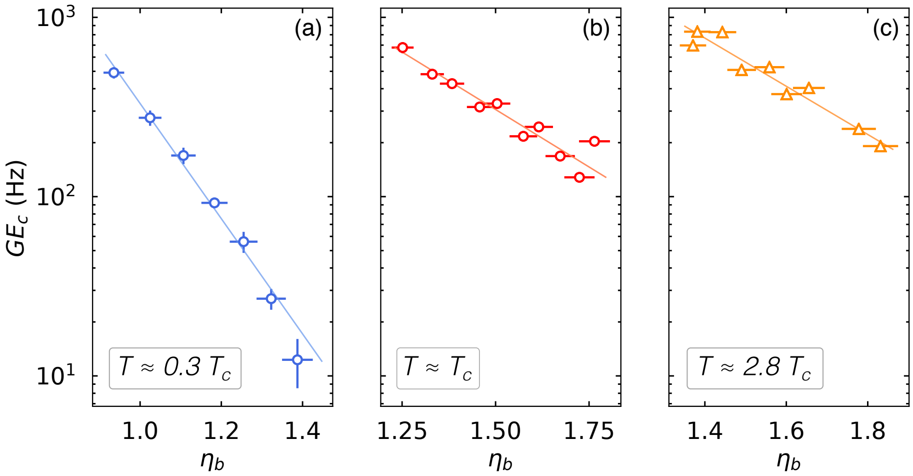

Figure 4.12: Measured charging rate GE_c scaling with the adimensional barrier strength $\eta_b = k_F d\sqrt{V_0/E_F}$ in different regimes: (a) a unitary Fermi gas with $1/k_F a \simeq 0$ at $T = 0.06(1)\,T_F \simeq 0.3\,T_c$ and $E_F = 2\pi\hbar \times 6$ kHz, (b) a unitary Fermi gas at $T = 0.20(1)\,T_F \simeq T_c$ and $E_F = 2\pi\hbar \times 11$ kHz and (c) a normal attractive Fermi gas with $1/k_F a \simeq -0.82$ at $T = 0.20(1)\,T_F \simeq 2.8\,T_c$ and $E_F = 2\pi\hbar \times 11$ kHz. The critical temperature for the superfluid transition on the BCS side of the resonance is calculated with Eq. (1.21). Vertical and horizontal error bars result from the standard error on G and the experimental uncertainty on V_0, respectively. Solid lines represent linear fits of $\log GE_c$. Data in (a) are the same already presented in Fig. 3.16 (b), now plotted as a function of η_b and employing the single fermions barrier height.

strength $\eta_b = k_F d\sqrt{V_0/E_F}$. In Fig. 4.12, the logarithmic trend of the charging rate GE_c is plotted versus η_b for a unitary gas at $T/T_F = 0.06(1)$ (a), $T/T_F = 0.20(1)$ (b) and a normal Fermi gas with $1/k_F a \simeq -0.82$ at $T/T_F = 0.20(1)$. Here, we report GE_c instead of the conductance G because of the impossibility to provide a reliable calculation of E_c for crossover gases away from unitarity. In all the presented cases, the logarithm of the charging rate presents a linearly decreasing trend for increasing η_b, as expected by $G \sim |t|^2$ and $|t|^2 \sim e^{-\eta_b}$. However, the slope of the scaling is observed to dramatically change when crossing the superfluid transition, namely its steepness decreases while temperature increases (see (a)-(b)). Already at $T \sim T_c$ the conductance scaling of a unitary Fermi gas closely resembles the one of a normal attractive gas in the BCS side of the resonance well above the critical temperature (see (b)-(c)). After having performed a linear fit of the logarithmic trends, we compare the slopes in the three different regimes, obtaining the ratios $s_a/s_b = 2.5(3)$ and $s_b/s_c = 0.95(14)$, where s_i identifies the slope of the (i) panel in Fig. 4.12. While the slopes of (b) and (c) are the same within experimental uncertainty, we measure a factor of 2.5(3) discrepancy between those of (a) and (b). The latter ratio is almost compatible with the factor of 2 expected between bosonic pair and single fermion transmission probabilities in the deep tunneling limit. This observation points to a change in the nature of resistive current carriers, from pairs to single fermionic quasi-particles, when crossing T_c from

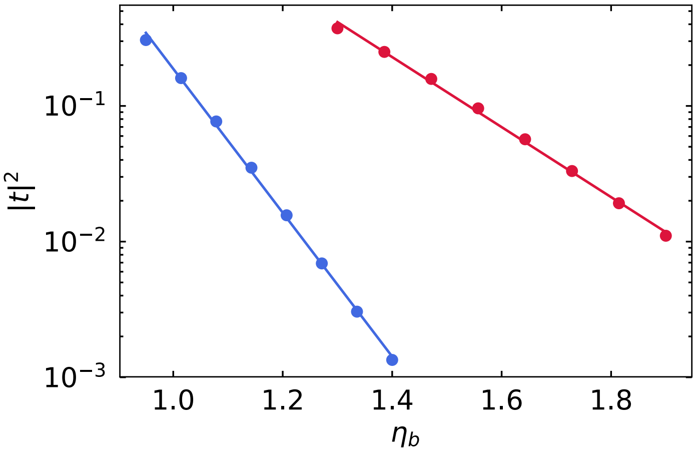

Figure 4.13: Tunneling probability $|t|^2$ through an Eckart barrier of dimension $d = 0.6 \times 0.95\,\mu$m as a function of the adimensional barrier strength η_b. $|t|^2$ is calculated following Eq. (3.19) for a particle of energy $\epsilon = h\sqrt{\xi} \times 6$ kHz and mass $2m$ (blue circles), and for a particle of energy $\epsilon = h\sqrt{\xi} \times 11$ kHz and mass m (red circles), where $\xi = 0.37$ is the zero-temperature Bertsch parameter. In both cases, the experimental conditions and the plotted range of η_b are the same as in Fig. 4.12 (a) and (b). Solid lines represent linear fits of $\log|t|^2$, which provide a ratio of 2.06 ± 0.07 between angular coefficients of blue and red points.

below at unitarity. The fact that the scaling behavior of a UFG immediately above critical (Fig. 4.12 (b)) is compatible with that of a normal attractive gas well above T_c (Fig. 4.12 (c)) suggests that for $T \gtrsim T_c$ incoherent transport at unitarity is strongly dominated by unpaired fermions. Anyway, our observation does not exclude the existence of a pseudogap phase above T_c, characterized by weak inter-particles correlations, to which low-momentum phonons, and therefore the conductance, are essentially insensitive [146].

To further confirm the compatibility of the measured s_a/s_b with the expected change in slope when passing from bosonic pairs to single fermions as carriers, we numerically compute the tunneling probability for an Eckart barrier under the same experimental conditions of Fig. 4.12 (a) and (b). Fig. 4.13 shows the calculated $|t_B|^2$ (blue circles) and $|t_F|^2$ (red circles) in the same range of the investigated η_b of panel (a) and (b), respectively. The scaling of $\log|t|^2$ is observed to undergo to a drastic change when passing from bosonic pair to single fermion carriers, which we quantify by performing a linear fit of it (solid lines in the figure) and extracting the slope for both cases. We find a ratio of 2.06 ± 0.07 between the pair and single-atom slopes, consistent with the expected factor of 2 from Eq. (4.30). This calculation confirms that, under the experimental conditions of Fig. 4.12, the scaling of $\log G$ is expected to differ by a factor of approximately 2 whether bound pairs or single atoms are the carriers of incoherent tunneling transport. The compatibility, within the experimental uncertainty, of our measurement of $s_a/s_b = 2.5(3)$ with the simple single-particle simulation suggests unpaired fermions as the carriers of resistive transport immediately above the critical temperature for the superfluid transition. Their hydrodynamic character, due to strong interactions, allows incoherent tunneling of sound modes even in the normal state, which determines the large conductance measured for a UFG above the critical temperature for the superfluid transition. The residual discrepancy between measured and simulated value of s_a/s_b might arise from a different mass or polarizability of the bosonic pairs in the strongly-correlated regime of UFG respect to the one we assumed for the simulation.

Chapter 5

Vortex shedding in quasi-homogeneous fermionic superfluids

One of the paradigmatic investigation of classical fluid dynamics is the study of the wake behind a moving obstacle. According to the value of the Reynolds number $\mathrm{Re} = vD/\eta$, where v and D are the obstacle velocity and dimension and η the fluid viscosity, different regimes of flow can be accessed [147]. For increasing Re, the steady or laminar flow created by the obstacle turns into a periodic shedding of vortices of alternating circulation, known as von Karman street. Finally, for even higher Re a turbulent regime is accessed, where the velocity and the pressure of the fluids vary chaotically. A similar phenomenology is expected to manifest in superfluids as well, despite the previous Reynolds number definition becoming nonsense for frictionless fluids with $\eta = 0$. As already discussed in Sec. 1.2.6, as long as the velocity of the obstacle is below the critical value v_c, its flow through the superfluid is friction-less since no excitations can be populated. For $v > v_c$ instead, dissipation occurs by nucleation of vortices with opposite circulation, namely vortex dipoles, as it has been observed in bosonic [148,149] and more recently also in fermionic superfluids [150]. The regular or chaotic emission of vortices, giving rise to the von Karman street and turbulent flow respectively, can be discriminated defining the superfluid Reynolds number $\mathrm{Re}_s = \frac{v-v_c}{\hbar/m}D$ [151]. Similarly to classical fluids, the obstacle produces a von Karman street of vortex dipoles for intermediate velocities, as observed for a BEC in Ref. [152], that is expected to turn into turbulent flow for $\mathrm{Re}_s \gtrsim 0.7$ [151]. Vortex shedding provides thus an elementary ingredient for the exploration of superfluid turbulence, which we address in the last part of this thesis work. In particular, in this chapter we report our preliminarily results on the observation of nucleated vortex dipoles in strongly interacting Fermi gases. To ease the vortex detection, we produce a quasi-homogeneous oblate cloud, where the vortex dynamic is expected to be substantially two-dimensional, since vortex line excitations are strongly suppressed in tightly confined gases along one direction [153,154]. In Sec. 5.1 we present the experimental procedure to create the quasi-homogeneous cloud, which is confined in a DMD-made box potential in the $x-y$ plane and squeezed along the vertical direction by the repulsive $\mathrm{TEM}_{(0,1)}$-like potential. Successively, Sec. 5.2 discusses the protocol employed to shed and observe vortices in both a molecular

BEC and a unitary Fermi gas (UFG), based on the dynamical shaping of the obstacle repulsive potential with the DMD. Finally, we report the measurements of the critical velocity at both interaction strengths, demonstrating the capability of our DMD setup to shed vortices into strongly interacting Fermi gases and providing a preliminary step towards the investigation of superfluid turbulence.

5.1 Production of the quasi-homogeneous sample

Uniform systems offer the possibility to directly access local quantities, which are instead extracted from trap averaged ones by means of local density approximation on trapped gases. In recent years, notable interest has been focused on the production and investigation of degenerate gases in homogeneous trapping potentials, which are typically created by shining a repulsive box trap on the atomic cloud. Following such recipe, both bosonic [155] and fermionic [156] degenerate states have been demonstrated in homogeneous potentials, even for the reduced dimensionality 2D case [123, 157]. An oblate and homogeneous superfluid offers the unique possibility of studying the two-dimensional vortex dynamic depending only on the interactions among vortices and with the medium, without introducing any trap effect such as their motion in a varying density background. In our setup, we create a quasi-homogeneous oblate gas by shaping a box potential with the DMD, to trap atoms in the $x-y$ plane, and squeezing the cloud along z with the $\mathrm{TEM}_{(0,1)}$-like repulsive beam propagating in the horizontal direction, as already illustrated in Sec. 2.1.1. The optical potential provided by the latter allows not only to contrast gravity, but also to compensate the harmonic potential provided by the Feshbach coils. Combining DMD and $\mathrm{TEM}_{(0,1)}$ optical potentials, we create quasi-homogeneous strongly-interacting Fermi gases, with a residual harmonic confinement in the z direction only. In the following, we present the optical scheme to produce the $\mathrm{TEM}_{(0,1)}$-like beam, together with a characterization of the beam profile, and subsequently discuss the experimental procedure for loading the cloud in the quasi-homogeneous potential.

5.1.1 $\mathrm{TEM}_{(0,1)}$ optical potential

We confine strongly-interacting Fermi gases in a quasi-homogeneous potential by trapping them in the vertical direction with a $\mathrm{TEM}_{(0,1)}$-like optical potentials, and shining a DMD-made box in the $x-y$ plane. To create the first beam, we employ 532 nm light, originating from the same Coherent Verdi V-8 laser we use for the DMD projection, and the optical setup reported in Fig. 5.1 (a). After the first telescope of f_1 and f_2 that sets the initial beam waist to $w_0 = 1.4$ mm, the symmetric Gaussian beam is turned into an elliptical one by magnifying it along the horizontal direction only with the cylindrical telescope $f_c - f_3$. Before the latter, the $\lambda/4$ and $\lambda/2$ waveplates are set to maximize the transmission of the following polarizing beam splitter, effectively cleaning the polarization of the beam to avoid spurious interference effects. We stabilize the beam power via a PID feedback loop relying on the measurement of the

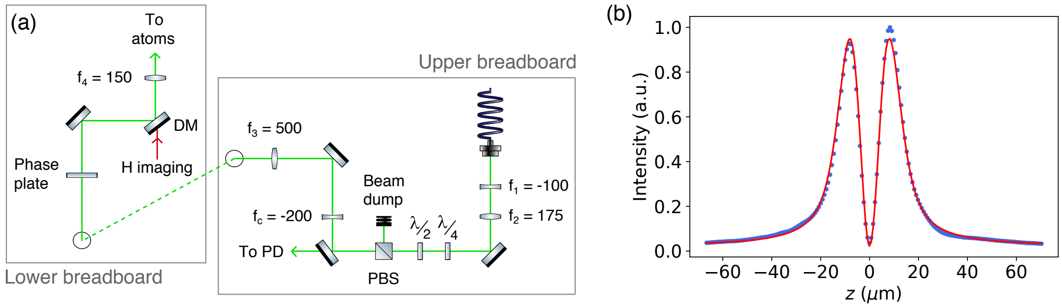

Figure 5.1: Production of the TEM$_{(0,1)}$-like beam. (a) Optical setup for the creation of the beam, extending over two breadboards at different levels. In the upper board the beam emerging from an optical fiber is shaped in the desired elliptic profile by the two telescopes, the last of which employing a cylindrical lens f_c. The $\lambda/4$ and $\lambda/2$ waveplates after the first telescope are set to maximize the transmission of the following polarizing beam splitter (PBS). The leak of the second mirror is measured by a photodiode (PD) and used to stabilized the beam power via a PID feedback loop. After being sent to the lower breadboard by a couple of 45° tilted mirrors, the beam acquires a phase shift of π of half of its profile thanks to the phase plate, and it is finally focused on the atomic cloud by the $f_4 = 150$ mm lens. The horizontal imaging beam shares the final path with the TEM$_{(0,1)}$-like one, to which it is recombined by the dichroic mirror (DM) to be then collimated by the $f_4 = 150$ mm lens. (b) TEM$_{(0,1)}$-like beam profile along the z direction, acquired by focusing it after the cell on a CCD camera by means of the horizontal imaging setup. The fit with Eq. (5.1) measures an equivalent waist of $\sigma = 8.73(3)\,\mu$m.

photodiode (PD), placed after the PBS to avoid polarization fluctuations to translate into intensity fluctuations. The elliptic beam created by the cylindrical telescope is then passed through a π step-phase plate by Silios Technologies, that imprints a phase shift of π on the electric field of only the lower half of the beam. This asymmetry in the beam phase produces a dip in its intensity, once focused on the atomic cloud by the f_4 lens. As already mentioned in Sec. 2.1.1, the TEM$_{(0,1)}$-like beam propagates collinearly with the horizontal imaging beam, which is recombined to the green path by the last dichroic mirror (DM) in the figure. The red beam is collimated to the atoms by the f_4 lens and, after exiting the cell, a telescope focuses it on an Andor camera to record the image of the atomic cloud. We employ the horizontal imaging setup to image the TEM$_{(0,1)}$ intensity profile on the atoms, obtaining the profile reported in Fig. 5.1 (b) along the vertical direction. Similarly to an Hermite-Gauss TEM$_{(0,1)}$ mode, the beam presents a node at the center of its z profile, the width of which is obtained by fitting it with the function:

$$I(x) = A \times \left[D\left(\frac{x - x_0}{\sigma} \right) \right]^2, \tag{5.1}$$

where $D(x)$ is the Dawson's integral defined as:

$$D(x) = e^{-x^2} \int_0^x e^{t^2}\, dt. \tag{5.2}$$

Eq. (5.1) represents the theoretically expected beam shape along the z direction, obtained by computing the intensity profile of a beam with a step like phase shift of π in the electric field [158]. From the fit with Eq. (5.1), we obtain an equivalent waist of $\sigma = 8.73(3)\mu$m, whereas along the y-direction, orthogonally to the propagation direction, the $\mathrm{TEM}_{(0,1)}$ profile is Gaussian with a waist of about $400\,\mu$m. Furthermore, such beam provides also an anti-confinement in the $x-y$ plane, which compensate the residual harmonic trap of roughly 8 Hz produced by the Feshbach field. In particular, the beam is designed to exactly compensate the magnetic trap when operating at high power (~ 2 W) [158], but we expect the harmonic contribution in the $x-y$ plane to be significantly reduced even for lower green powers.

When shining the $\mathrm{TEM}_{(0,1)}$ repulsive beam on the cloud, atoms get trapped inside the intensity node, the beam squeezing the cloud along the vertical direction and providing a support against gravity. For sufficiently high green power, the $\mathrm{TEM}_{(0,1)}$ confinement is tight enough to enter the quasi-2D regime of $\hbar\omega_z \ll E_F$, as the vertical trap frequency ω_z is proportional to the square root of the beam power. In particular, under our experimental conditions we expect 2 W to provide a vertical trap frequency of over 8 kHz, enough to access the kinematic two-dimensional regime with about 20×10^3 atoms. However, for the goal of observing quantized vortices, we don't need to access the quasi-2D regime, that has the disadvantage of constraining the number of atoms to such a low value that the vortex visibility is suppressed. For all the measurements presented in this chapter, we rather operate the $\mathrm{TEM}_{(0,1)}$-like beam at a low power $\lesssim 100$ mW, enough to squeeze the cloud in an oblate geometry, but far from the quasi-2D regime. Under our working conditions, the atomic motion along the z direction is not frozen and the system is therefore quasi-homogeneous, because of the harmonic confinement along the vertical. Moreover, we slightly defocus the $\mathrm{TEM}_{(0,1)}$ beam up up to an equivalent waist of $\sigma \simeq 10\,\mu$m, so to reduce the vertical squeezing of the cloud, which allow us to trap more atoms with the same power needed to contrast gravity.

5.1.2 Loading the quasi-homogeneous trap

To obtain a uniform system, atoms have to be transferred from the crossed ODT to the quasi-homogeneous one. For this purpose we employ the scheme illustrated in Fig. 5.2 (a). Before the evaporation in the crossed ODT is over, we ramp the $\mathrm{TEM}_{(0,1)}$ power up to the desired value in 100 ms, and successively ramp the DMD-made box potential as well. When both green beams have reached their set power, we adiabatically ramp down both the IPG and Mephisto beams simultaneously to then switch them off. After the end of the $\mathrm{TEM}_{(0,1)}$ ramp and before beginning the DMD one, the magnetic field is linearly swept from resonance, where the evaporation happens, to the BEC side, where we perform the first observations of quantized vortices. For experiments performed at unitarity instead, the magnetic field is kept on resonance during the whole transfer in the quasi-homogeneous trap.

Fig. 5.2 (b) shows the two-dimensional density profile of a molecular BEC at $1/k_F a \simeq 6$ trapped in two different box potentials. Whatever the geometry of the

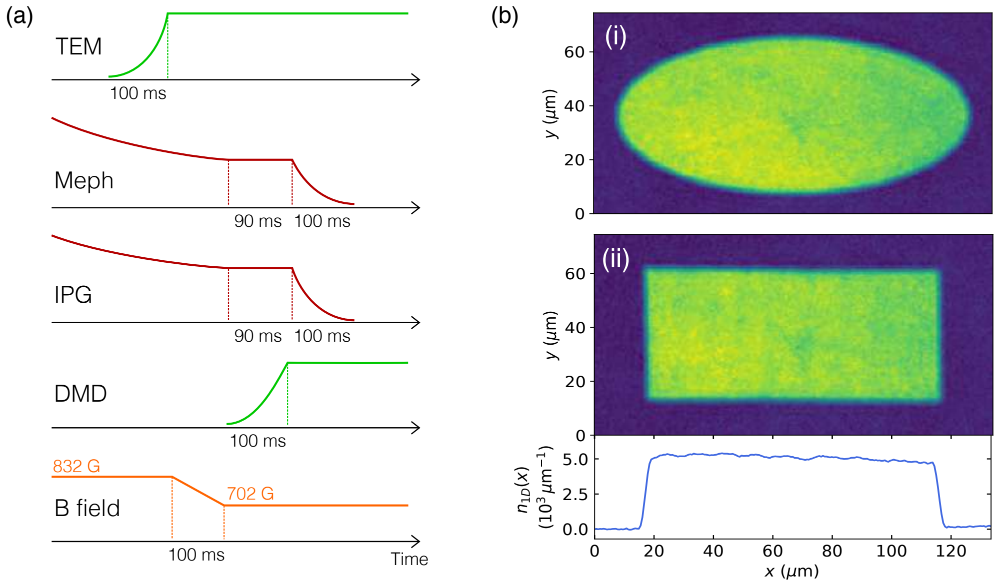

Figure 5.2: Quasi-homogeneous strongly interacting Fermi gases. (a) Loading of the quasi-homogeneous trap. Before the evaporation in the crossed ODT is over, the TEM$_{(0,1)}$ beam is ramped to the desired value in 100 ms, whereas the DMD ramp is started a few ms before IPG and Mephisto has reached their final evaporation threshold. When the DMD-made $x-y$ plane box has reached its set power, both crossing beams are adiabatically ramped down to be then switched off. After the end of the TEM$_{(0,1)}$ ramp and before beginning the DMD one, the magnetic field is swept from resonance (832 G) to a target value in the BEC side where we performed the first observation of quantized vortices (702 G). (b) Density profile of a molecular BEC at $1/k_F a \simeq 6$ in the quasi-homogeneous trap. With the TEM$_{(0,1)}$ power set to 40 mW, the vertical trap frequency is measured to be 356(2) Hz. The shape of the DMD-made box can be designed according to the experiment requirements, turning from an elliptical (i) to a rectangular one (ii). On the bottom of (ii) the integrated one-dimensional profile of the cloud in the rectangular box is reported. For both panels the total atom number measured inside the box is of about 50×10^3.

box, that we can freely tune with the DMD, the density is observed to be reasonably uniform all over the trap volume. The flatness of the integrated one-dimensional profile of (ii) (blue solid line on the bottom panel) demonstrates the homogeneity of our cloud in the $x-y$ plane. Even at the low 40 mW power of TEM$_{(0,1)}$ employed for the reported images, the anti-confinement of such beam is enough to significantly reduce the harmonic trap produced by the Feshbach field. In particular, we measure a trap frequency of $\omega_r \simeq 2.5$ Hz in $x-y$ plane when the gas is loaded in the combined trap provided by TEM$_{(0,1)}$ and Feshbach coils only, without shining the DMD box. With such information we can estimate the properties of our quasi-homogeneous cloud, that explore only a small portion of the big harmonic Feshbach potential thanks to the DMD box. By calculating the total atom number in the Feshbach trap needed to populate the box region with the 50×10^3 atoms we measure inside it, we estimate the Thomas-Fermi radius R_r of the residual harmonic confinement to be of the order of $500\,\mu$m.

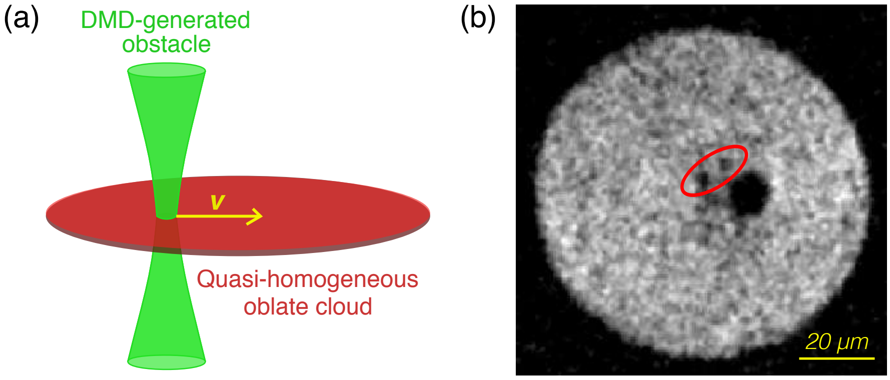

Figure 5.3: Vortex shedding in quasi-homogeneous fermionic superfluids. (a) Sketch of the protocol for vortex shedding: we shine a DMD-generated repulsive obstacle in the quasi-homogeneous cloud and move it with a constant tunable velocity v to induce vortex nucleation. (b) *In situ* image of a molecular BEC at $1/k_F a \simeq 6$ at the end of the motion of a round $10\,\mu$m sized obstacle with $v > v_c$. The image is taken before the obstacle is ramped down and a vortex dipole is clearly visible on its wake, signaled by the red line.

The quasi-homogeneous cloud, that extend up to $100\,\mu$m, explores therefore only less than 10% of R_r, so that we can reasonably assume it to be homogeneous.

5.2 Vortex shedding with DMD

We shed vortices over quasi-homogeneous fermionic superfluids by moving a DMD-generated obstacle through the atomic cloud with a constant velocity, as pictorially sketched by Fig. 5.3 (a). As for the barrier translation employed in the previous chapters, we dynamically control the picture of the DMD to produce an effective motion of the obstacle on the cloud, as it will be further discussed in Sec. 5.2.1. When the obstacle velocity is higher than the critical one, vortices nucleate on its wake, as visible in the *in-situ* image of Fig. 5.3 (b). The vortex detection from *in-situ* images is particularly challenging as the vortex core extend over a region comparable with the healing length, that for our fermionic superfluids is of the order of one micron. We instead observe vortices as clear density dips by performing a time-of-flight imaging of the cloud, that allows to detect them even in the strongly interacting regime when combined with a fast sweep of the magnetic field, as it will be discussed in Sec. 5.2.2. Finally, in Sec. 5.2.3 we report our measurement of the critical velocity for vortex shedding performed in both a molecular BEC and a UFG.

5.2.1 Shedding protocol

To move the obstacle through the atomic cloud, we employ an identical protocol to that illustrated in Sec. 3.1.2: we create a sequence of images displaying the obstacle at one DMD-pixel distance from one another and play it on the DMD with a constant

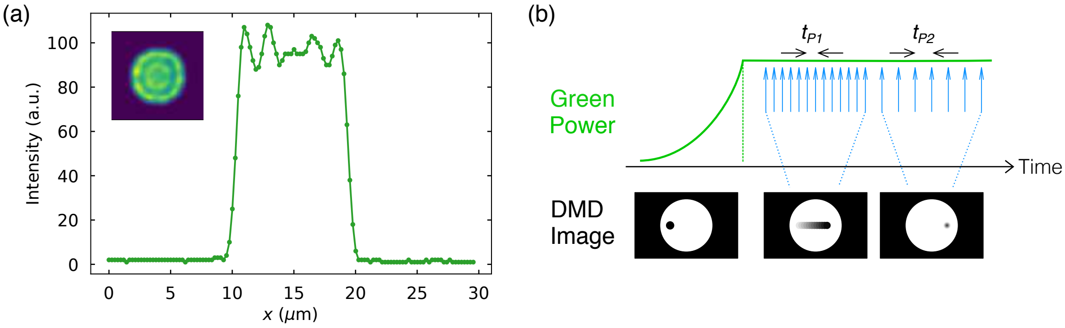

Figure 5.4: Vortex shedding with a DMD. (a) Characterization of the round obstacle of 40 DMD mirrors diameter. The image on the inset is acquired by imaging the DMD screen on the Thorlabs camera of the secondary path of Fig. 2.11, and its central cut along the vertical direction is plotted versus the coordinate x on the atomic plane. (b) Dynamic control of the DMD image for vortex shedding. When the green light impinging of the device is ramped up, the first image of the sequence is displayed on the DMD screen, showing the obstacle on the left side of the cloud. When the power has reached the set value, a sequence of triggers spaced by the *Picture time* t_{P1} is sent to the device to move the obstacle to the right with a velocity $v = 0.25/t_{P1}$, with t_{P1} measured in ms. At the end of the translation the obstacle is adiabatically ramped down by playing a sequence of images with a progressively shrinked obstacle with a *Picture time* t_{P2}.

and tunable *Picture Time*. The obstacle pattern is cut from an homogeneous profile optimized with the feedback procedure described in Sec. 2.3.2 to show about the 60% of ON mirror in the central region, so that the potential height felt by the atoms is the same during the whole movement. In particular, for the critical velocity measurements presented in Sec. 5.2.3, we employ a round obstacle of 40 DMD mirrors diameter, corresponding to 10 μm on the atomic plane. We characterize the shape of the obstacle by imaging its profile on the auxiliary camera placed in the secondary optical path of Fig. 2.11, obtaining the profile presented in Fig. 5.4 (a). The obstacle intensity is observed to deviate by about 10%, since the homogeneous profile is distorted by diffraction from the most limiting aperture of the DMD setup, which is the iris in between the telescope of Fig. 2.11. Anyway, such fluctuating profile is not expected to affect atoms as long as we set the DMD potential height to be higher than the chemical potential of the cloud, namely $V_0 > \mu$, as in Fig. 5.3 (b) where the obstacle is observed to carve a clear hole in the atomic density. Under such condition, that is fulfilled for all the measurements reported in this chapter, atoms explores only the lower part of the obstacle potential, without being influenced by the roughness of its profile.

As already mentioned, vortex visibility is much higher when letting the cloud to expand for a time of flight, after having switched off all the trapping potentials, including the obstacle one. However, abruptly turning off such potential produces density fluctuations in correspondence of its position, resulting from atoms moving to fill the hole it left, that sensibly reduces the vortex visibility. To clearly observe vortex, the obstacle has to be adiabatically ramped down at the end of its motion, which we do by adding a second set of images in the DMD sequence, showing the obstacle in its final position while progressively reducing its diameter. In particular, in each image of this ramp down sequence the obstacle shows a 2 DMD mirrors smaller diameter respect to the previous one, producing a symmetric reduction of its size. The second sequence is played on the DMD with a different picture time $t_{P2} = 0.5$ ms, long enough to ensure the adiabaticity of the process, and kept constant for all the dataset at different obstacle velocity. We set the last image of the ramp down sequence to consist of only the box potential, so that, after the display of the whole sequence, time-of-flight imaging can be performed by switching off all the remaining potentials, including the DMD one.

5.2.2 Vortex observation in strongly-interacting Fermi gases

As already mentioned in Sec. 1.2.6, vortices consist of a singularity in the order parameter phase, that result in a vanishing condensed density in correspondence of the vortex core. In bosonic superfluid, where the condensed fraction reaches unity at zero temperature, the presence of the vortex is signaled by a hole in the density of the gas, which extend over a length scale comparable with the healing length ξ_h of the condensate. For ξ_h being of the order of hundreds of nanometer in weakly-interacting BECs, vortices are typically observed by recording a time-of-flight (TOF) image of the cloud, to enlarge the vortex core by letting the superfluid to freely expand. However, nowadays the high resolution reachable with state-of-the-art imaging systems is sufficient to resolve vortices even *in situ* [159]. In particular, our sub-micron resolution along the vertical direction is able to resolve vortices *in situ* in molecular BECs, as testified by the picture of Fig. 5.3 (b). However, the contrast of *in situ* vortices is not particularly high and we decide to rely on TOF imaging to enhance their visibility. In particular, we employ 1 ms TOF to observe vortices in molecular BECs, enough for their core to be clearly visible, but still short to keep different vortices well separated.

TOF imaging is a consolidated technique to detect vortices in bosonic superfluids, applicable also in our case of molecular BEC, but only in the weakly interacting limit. In fact, the vanishing condensed density in correspondance of the vortex core does not produce a hole in strongly-interacting fermionic superfluids, since their condensed density monotonically decreases when moving toward resonance, as probed by the measurement reported in Sec. 3.3.3. As mentioned in Sec. 1.2.6, to detect vortices in fermionic superfluids the rapid ramp technique has to be applied. During the TOF, the magnetic field is quickly swept towards to BEC side, where pairs turning into tightly bound molecules effectively increase the vortex visibility. In fact, the expected enhancement of the condensed fraction during the magnetic ramp [64] clears the vortex core from non-condensed pairs, increasing thereby the vortex contrast. In particular, for the measurements reported in this chapter employing a UFG, vortices are observed by performing a linear sweep of the magnetic field towards $702\,G$ during a 1.5 ms TOF.

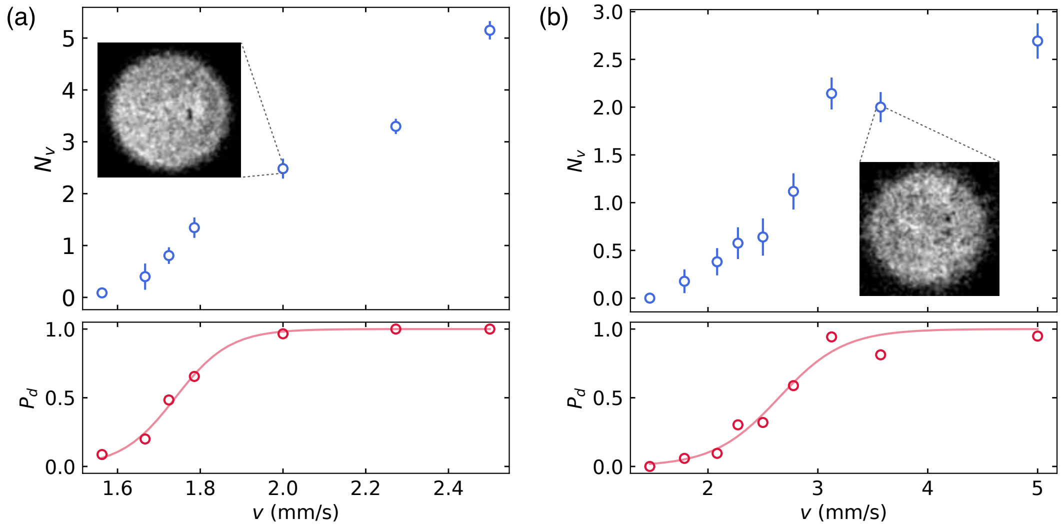

Figure 5.5: Critical velocity for vortex shedding for a molecular BEC (mBEC) at $1/k_F a \simeq 6$ (a) and a unitary Fermi gas (UFG) at $1/k_F a \simeq 0$ (b). Top panels: number of nucleated vortices counted in the time-of-flight image of the cloud. The shedding is performed following the protocol describe in Sec. 5.2.1 with a $10\,\mu$m diameter round obstacle of height $V_0 \gg \mu_B$, translated over a distance of $25\,\mu$m. Inset: time-of-flight image of the cloud at the two interaction strengths displaying a single vortex dipole. Bottom panels: probability of observing at least a vortex dipole as a function of the obstacle velocity. Data are fitted with the sigmoidal distribution of Eq. (5.3) to extract the critical velocities of $v_c = 1.74(10)$ mm/s for the mBEC and $v_c = 2.6(4)$ mm/s for the UFG.

5.2.3 Critical velocity for vortex shedding

Vortices nucleate in the wake of a moving obstacle only when it moves faster than the critical velocity for vortex shedding v_c. We measure v_c by counting the number of vortices in the TOF image of the cloud after an obstacle movement of $25\,\mu$m with varying velocities. We perform the experiment both in a molecular BEC (mBEC) at $1/k_F a \simeq 6$ and in a UFG, the results of which are reported in Fig. 5.5 (a) and (b), respectively. As visible in the two TOF images in inset, vortices are detected as clear holes in the density profile of the cloud at both interaction strengths, employing the rapid ramp technique for the UFG. The number of detected vortices N_v is observed to be non zero only above a threshold velocity to then increase monotonically. To extract the critical velocity for vortex shedding, for each dataset we calculate the probability of observing at least a vortex dipole P_d, which is plot as red circles on the bottom panel of (a) and (b), and fit it with the sigmoidal function [160]:

$$P(v) = \frac{1}{1 + e^{-(v-v_c)/\gamma}}. \tag{5.3}$$

With the above assumption for the probability distribution, the critical velocity v_c is defined as the velocity that gives a 50% probability of generating a dipole, whereas the width of the distribution γ can be employed to estimate the error over v_c [160].

In particular, we take $1.5\,\gamma$ as estimator of the uncertainty on v_c, which by definition corresponds to the probability range of $0.2 \leq P_d \leq 0.8$. With the described procedure, we obtain $v_c = 1.74(10)$ mm/s $\simeq 0.09\,v_F$ for the mBEC and $v_c = 2.6(4)$ mm/s $\simeq 0.1\,v_F$ for the UFG, where $v_F = \sqrt{2E_F/m}$ is the Fermi velocity of the two clouds at $E_F = h \times 3.0$ kHz and $h \times 7$ kHz, respectively. We note that the higher uncertainty on the v_c value at unitarity is due to the lower vortex visibility in a UFG. The critical velocity for vortex shedding is found to be higher at resonance, where the superfluid is expected to be the most robust, as already discussed in Sec. 1.2.6. The measured values at both interaction strenghts are much lower than the expected critical velocity following the Landau criterion of Eq. (1.33), which gives $v_{c,L} = c_s = \sqrt{\mu_B/m_B} \simeq 5.3$ mm/s for the mBEC and $v_{c,L} \simeq \sqrt{\xi/3}\,v_F \simeq 9.2$ mm/s at unitarity. However, a comparison between the two cannot be made straightforwardly, since their physical meaning is not the same: $v_{c,L}$ determines the onset of dissipation via the creation of microscopic excitations, whereas the shedding protocol probes the vortex nucleation dynamics within a finite obstacle movement $L = 25\,\mu$m. The Landau critical velocity and the one for vortex shedding may converge for infinitly long obstacle translation, but still the geometry of the obstacle and its height are expected to play a role. In particular, theoretical studies accounting for the compressible nature of the superfluid flow predict a critical velocity for vortex nucleation of $0.37\,c_s$ in the BEC regime, assuming the obstacle to be a hard cylinder of dimension much larger than the healing length [161]. We obtain $v_c \simeq 0.33\,c_s$ for the mBEC and $v_c \simeq 0.28\,c_s$ for the UFG, in reasonable agreement with the expected value if we consider that we overestimate the speed of sound. The effective sound speed for our oblate geometry consists indeed of the average c_s along the z direction, which is expected to be lower than the above reported values and could be measured by exciting sound waves in our oblate cloud. Finally, we note that our measured v_c are about a factor 2 lower than the critical velocity for vortex shedding measured in Ref. [150] for a similar obstacle movement length. We ascribe such discrepancy to the not high enough value of V_0 employed in our measurements, since v_c shows a minimum for $V_0 \simeq \mu$ to then saturate for $V_0 \gg \mu$.

The results presented in this chapter demonstrate the capability of our experimental setup to shed vortices and detected them even at unitarity, providing a preliminary but highly relevant step towards the investigation of superfluid turbulence. As already mentioned, the flow in the wake of a moving obstacle is expected to become turbulent for $\mathrm{Re}_s \geq 0.7$, that, given the obstacle size of $10\,\mu$m and the measured critical velocity v_c, corresponds to shedding velocity of about 2 mm/s for the mBEC and 3 mm/s for the UFG. Unfortunately, the regime of high speed of $v \geq 3.5$ mm/s cannot be easily explored with the presented protocol. In fact, for such a high speed, the *Picture Time* employed to display the image sequence on the DMD gets comparable with the switching time of $10\,\mu$s of the device, causing the motion of the obstacle to be rather step-wise than continuous. Such issue could be overcome in the future by using an elliptic obstacle, which is expected to present a lower critical velocity for vortex shedding [162].

Conclusions and outlook

In this thesis work we experimentally investigate the tunneling transport of strongly-interacting Fermi gases of lithium-6 atoms. In particular, we exploit the high resolution of our experimental setup to realize for the first time a current-biased Josephson junction of fermionic superfluids in the BEC-BCS crossover. We inject a controlled current into the junction by translating the repulsive barrier with constant velocity and we measure the current-chemical potential $I - \Delta\mu$ characteristic, the analogous of the current-voltage curve in a superconducting Josephson junction. In this way, we characterize the conduction of crossover gases across the superfluid transition, extracting valuable information on both the order parameter, and on the main excitations on top of the ground state.

In a first experiment, we characterize an atomic current-biased junction of fermionic superfluids. In all the explored regimes of superfluidity, we observe a highly-non linear current-chemical potential characteristic, featuring dc Josephson regime, where a dissipationless supercurrent flows through the junction up to the critical current I_c. We measure a sinusoidal current-phase relation, the fingerprint of dc Josephson effect. We characterize the critical current I_c as a function of the barrier properties and we map its evolution throughout the BEC-BCS crossover. Furthermore, from the comparison between the measured I_c and the analytic model presented in Ref. [101], we extract the order parameter of fermionic superfluids, namely their condensed fraction, which was so far predicted only by sophisticated theory models. Our work constitutes the first direct measurement of the order parameter in the BEC-BCS crossover, the quantitative determination of which has been so far indirect and somewhat inconclusive. We demonstrate Josephson critical current as a reliable quantifier of the condensed density, that could be employed for disclosing the nature and the symmetry of the order parameter of any condensed system [163, 164].

In a second experiment, we characterize the operation of our current-biased Josephson junction across the superfluid transition. We observe the $I - \Delta\mu$ curve to evolve from a highly non linear to an Ohmic behavior while approaching the critical temperature for condensation T_c. We measure the maximum Josephson critical current I_{max} across the superfluid transition, that, from the comparison with our analytic model, is observed to preserve the direct proportionality with the condensate density even at finite temperature. From the vanishing trend of I_{max} for increasing T, we extract a lower limit for the critical temperature of the superfluid transition for crossover gases, found in qualitative agreement with theoretical expectations. Remarkably, we observe how the presence of the fermionic condensate determines not only the dissipationless supercurrent, but also the Ohmic conduction, feeding both Josephson and normal currents. In particular, we observe an anomalous conductance to dominate at low temperature, arising from the coherent coupling between the condensate and phononic Bogoliubov-Anderson excitations. As temperature increases, we measure a decreasing conductance, that still remains much higher than that of an ideal Fermi gas even above T_c. We ascribe the enhanced transport at $T > T_c$ to the hydrodynamic behavior of unpaired fermions at unitarity, that admits incoherent tunneling of sound modes even in the normal (non-superfluid) state. We verify the single-particle nature of transport carriers by comparing the conductance scaling with the barrier properties across the superfluid transition. Our observations are anyway compatible with the presence of a pseudogap phase in the unitary Fermi gas phase diagram, which could be further tested by studying the conductance of a spin-current driven junction [165].

In the final part of this thesis, we explore fermionic superfluidity from a different point of view. Our experimental system offers indeed a versatile platform, where arbitrary and dynamical optical potentials can be imprinted to realize almost any desired geometry. In particular, we investigate the vortex shedding dynamics in the wake of a moving obstacle. To this purpose, we realize an oblate quasi-homogeneous cloud by means of a $\mathrm{TEM}_{(0,1)}$-like optical potential and we measure the critical velocity for vortex shedding. This represents a preliminary step towards the exploration of quantum turbulence in strongly-interacting Fermi superfluids.

The implementation of the $\mathrm{TEM}_{(0,1)}$-like beam allows to explore the intriguing two-dimensional (2D) superfluidity of crossover gases [166], as pioneered by the recent works in Refs. [32, 167–169]. In 2D, phase fluctuations inhibit true long-range coherence, and only superfluidity of the Berezinskii-Kosterlitz-Thouless (BKT) type can exist [170, 171]. However, it is precisely in two-dimensional solid state materials that high-T_c superconductivity occurs at ambient pressure [172]. Ultracold fermions confined in two dimensions offer thus the perfect playground to address the topic from both a fundamental physics and quantum simulation point of view.

Finally, the versatility of our experimental system allows for adding one last ingredient in our ultracold fermionic cloud: the presence of tunable disorder. As I demonstrated in my Master Thesis in Ref. [121], disordered optical potentials can be straightforwardly implemented with the DMD, with the possibility to tune their statistical properties by varying the resolution of the imaging system. In particular, we can generate two different kinds of disorder: a binary point-like disorder and a more standard speckles one. They differ not only in statistical properties, but also for their expected localization effect on a 2D atomic cloud [173]. Whereas speckles present a constant percolation threshold indeed, the one of point-like disorder can be reduced by setting the proper density and size of disorder elements, so to produce negligible classical trapping effects. DMD-generated point-like disorder can be thereby employed to explore quantum localization effects on degenerate fermionic clouds. In the case of non-interacting ideal Fermi gases, point-like disorder represents a unique opportunity to study Anderson Localization phenomena in 2D [102], that have been never observed so far. On the other hand, for interacting particles, and in case superfluid, the combination of a homogeneous potential and point-like disorder may offer an ideal playground to study many-body localization effects [174] and the onset of the superfluid-to-insulator transition [175], the understanding and characterization of which are still under debate in fermionic systems.

Appendix A

Timing properties of the DMD

When producing an arbitrary dynamical optical potential with the DMD, it is essential that the sequence display settings are perfectly synchronized with the rest of the experimental sequence. The dynamical DMD control presented in Sec. 2.3.2 relies on an externally triggered configuration for the switch between an image and the following, namely on the `SLAVE` mode, that allows for setting the sequence display directly from the control program of the experiment. However, the DMD can be operated in other two timing configurations, `MASTER` and `STEP` mode, which are presented in the following. Before discussing the three possible timing configurations, we illustrate the two displaying modes of the DMD: the `DEFAULT` and the `UNINTERRUPTED` one.

`DEFAULT` and `UNINTERRUPTED` mode

In general, a pre-loaded image sequence is displayed by the DMD according to two timing parameters, both settable with the ALP4lib of Ref. [120]: the *Illumination Time* t_I, that sets the display time of each image of the sequence, and the *Picture Time* t_P, that regulates the sequence period. *Illumination* and *Picture Time* do not coincide in the `DEFAULT` operation mode of the device, as a dark phase of duration $t_D = t_P - t_I$ is included in the sequence, during which all mirrors are arranged in the ON direction, as depicted in Fig. A.1 (a). When both t_P and t_I are set by the user, the dark time is adapted to fulfill the previous relation, under the constraint of $t_D \geq 44\,\mu$s. On the other hand, when $t_P - t_I < 44\,\mu$s, t_I is reduced to have the minimum dark time of $t_D = 44\,\mu$s. The `DEFAULT` mode does not access the highest frame rate of the DMD because of the presence of the dark phases, but allows for the display of gray-scaled images. In particular, grayscale is produced out from the binary ON-OFF states of the mirrors by opportunely flickering them to fade the original black or white color. However, to produce tailored optical potentials we do not need such feature, as grayscale patterns on atoms can be created by employing dithering algorithms and reducing the resolution of the DMD projecting setup. We therefore operate the DMD under the `UNINTERRUPTED` mode, which avoids dark phases at the cost of allowing the display of black-and-white images only. In such configuration, only t_P suffices for setting the timing properties of the sequence display and $t_D = 0$, as illustrated in Fig.

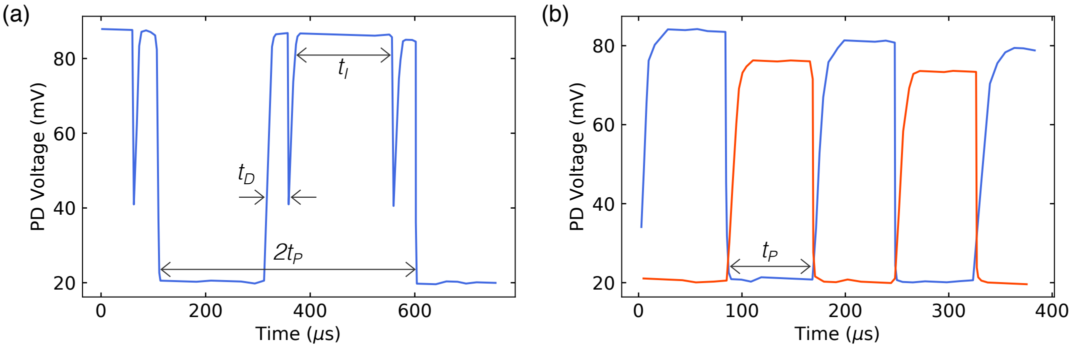

Figure A.1: Timing properties of the DMD in the `DEFAULT` (a) and `UNINTERRUPTED` mode (b). Signals are collected by focusing the reflected light in the ON and OFF direction of the DMD on two photodiodes (PDs), similarly as for data in Fig. 2.13, when a sequence alternating an all-black to an all-white image is loaded on the device. Blue (red) line corresponds to the signal in the ON (OFF) direction. (a) When the DMD is operated in `DEFAULT` mode, at the end of each image display the device presents a dark phase of duration $t_D = t_P - t_I$, where all mirrors are set in the ON direction. In the reported image we set $t_I = 200\,\mu$s and t_P is adjusted to fulfill the relation $t_P = t_I + t_D$, with $t_D = 44\,\mu$s. (b) In the `UNINTERRUPTED` mode, dark phases are avoided and the display timing is controlled by setting t_P only. In the reported image we set $t_P = 80\,\mu$s.

A.1 (b). The value of *Picture Time* has to be chosen according to $t_P \geq 44\,\mu$s, that sets the highest frame rate of the device to 22.7 kHz. Whenever t_I is specified as well, its value is ignored, and the sequence is displayed according to t_P only.

In the following we present all the possible timing configurations, assuming the device to be operated in `UNINTERRUPTED` mode.

`MASTER` mode

When the DMD is set in `MASTER` mode, the pre-loaded image sequence is displayed with a *Picture Time* t_P set by the user, and counted by the internal clock of the device. If a value of $t_P < 44\,\mu$s is set, the sequence is anyway displayed with the minimum allowed *Picture Time* of $44\,\mu$s. In both Fig. A.1 (a) and (b) the DMD was set to operate in `MASTER` mode.

`SLAVE` mode

The sequence display timing can be controlled by external triggers, if operating the DMD in `SLAVE` mode, as already discussed in Sec. 2.3.2. Under such configuration, the set value of $t_P \geq 44\,\mu$s by the user define the time interval after which the device allows a second trigger, ignoring all signals arriving before t_P. For the production of the dynamical potentials presented in this thesis, we always set $t_P = 44\,\mu$s so that the highest frame rate of the device can be exploited, and then adjust the trigger sequence to produce the desired display timing. We note that throughout this thesis, we call

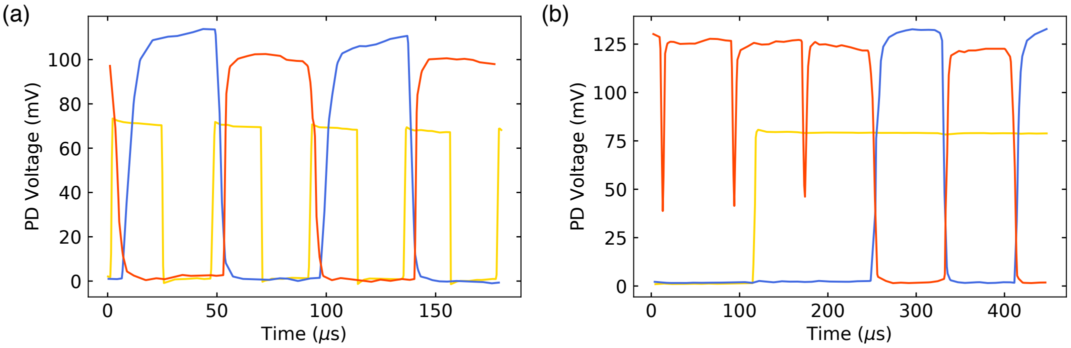

Figure A.2: Timing properties of the DMD operating in `SLAVE` (a) and `STEP` (b) mode. As for Fig. A.1, blue and red lines represent the light reflected in the ON and OFF directions, respectively, whereas the yellow line reports the trigger signal, collected directly from the function generator we used to produce it. (a) In `SLAVE` mode, the DMD switches from an image to the following in the pre-loaded sequence when an external trigger arrives to the device. Here we set $t_P = 44\,\mu$s, the minimum allowed value, so that the DMD can exploit its maximum frame-rate and the switching is completely controlled by the external triggers, as long as their time distance is higher than t_P. The trigger frequency is set to 22.7 kHz. (b) In `STEP` mode the sequence display is regulated by an internal timing, but under conditional frame transition. The trigger signal acts as a gate: only when the signal is detected the DMD switches images with the set timing. Here, we set $t_P = 80\,\mu$s.

Picture Time the time interval between two trigger signals, which set the actual display time of each image when the device is operated in `SLAVE` mode, whereas $t_P = 44\,\mu$ set with the ALP4lib corresponds to the minimum allowed *Picture Time* of the sequence. As visible in Fig. A.2 (a), when a trigger arrives to the DMD, the image is switched to the following in the sequence, with a time delay of $\simeq 5\,\mu$s due to the signal transmission time, that anyway doesn't affect the production of the dynamical potential. The device can be set to switch the image whether in correspondence of the rising or the falling edge of the trigger signals, and a further delay time between the trigger and the actual switch can be introduced.

`STEP` mode

Finally, the DMD can be operated in the `STEP` mode, where the internal timing is combined with a conditional frame transition regulated by an external trigger. As illustrated in Fig. A.2 (b), as long as the conditional trigger is OFF, the device keeps displaying the same picture, and only when an ON trigger is detected it starts to play the sequence with a *Picture Time* $t_P > 44\,\mu$s set by the user and counted with the internal clock of the DMD. The trigger signal acts thereby as a gate: every t_P the device goes checking the trigger state, and only if this is found in the correct state it switches the image to the following in the sequence. Also in `STEP` mode, the trigger level to be considered as an open gate can be set to be both the top or the bottom level.

The `SLAVE` mode is the most suitable configuration for imprinting dynamical optical potentials with the DMD, as it allows for the fine tuning of the display timing directly from the control program of the experiment and a consequent perfect synchronization with the rest of the experimental sequence. We note that the `STEP` mode offer the advantage of having a single trigger signal to send to the DMD for the image sequence to be displayed, at the cost of introducing a jitter time delay in the starting of the sequence, due to the possible not perfect syncronization between the experimental cycle and the device internal timing.

Bibliography

[1] W. Zwerger, *The BCS-BEC crossover and the unitary Fermi gas*, vol. 836. Springer Science & Business Media, 2011.

[2] S. Giorgini, L. P. Pitaevskii, and S. Stringari, "Theory of ultracold atomic Fermi gases," *Reviews of Modern Physics*, vol. 80, no. 4, pp. 1215–1274, 2008.

[3] M. Troyer and U.-J. Wiese, "Computational complexity and fundamental limitations to fermionic quantum Monte Carlo simulations," *Physical Review Letters*, vol. 94, no. 17, p. 170201, 2005.

[4] R. P. Feynman, "Simulating physics with computers," *Int. J. Theor. Phys*, vol. 21, no. 6/7, 1982.

[5] I. M. Georgescu, S. Ashhab, and F. Nori, "Quantum simulation," *Reviews of Modern Physics*, vol. 86, no. 1, pp. 153–185, 2014.

[6] I. Bloch, J. Dalibard, and W. Zwerger, "Many-body physics with ultracold gases," *Reviews of Modern Physics*, vol. 80, no. 3, p. 885, 2008.

[7] T. Esslinger, "Fermi-Hubbard physics with atoms in an optical lattice," 2010.

[8] C. Gross and I. Bloch, "Quantum simulations with ultracold atoms in optical lattices," *Science*, vol. 357, no. 6355, pp. 995–1001, 2017.

[9] H. Büchler, M. Hermele, S. D. Huber, M. P. Fisher, and P. Zoller, "Atomic quantum simulator for lattice gauge theories and ring exchange models," *Physical Review Letters*, vol. 95, no. 4, p. 040402, 2005.

[10] S. Giovanazzi, "Hawking radiation in sonic black holes," *Physical Review Letters*, vol. 94, no. 6, p. 061302, 2005.

[11] U. R. Fischer and R. Schützhold, "Quantum simulation of cosmic inflation in two-component Bose-Einstein condensates," *Physical Review A*, vol. 70, no. 6, p. 063615, 2004.

[12] C. Chin, R. Grimm, P. Julienne, and E. Tiesinga, "Feshbach resonances in ultracold gases," *Reviews of Modern Physics*, vol. 82, no. 2, p. 1225, 2010.

[13] M. Greiner, O. Mandel, T. Esslinger, T. W. Hänsch, and I. Bloch, "Quantum phase transition from a superfluid to a Mott insulator in a gas of ultracold atoms," *nature*, vol. 415, no. 6867, pp. 39–44, 2002.

[14] R. Jördens, N. Strohmaier, K. Günter, H. Moritz, and T. Esslinger, "A Mott insulator of fermionic atoms in an optical lattice," *Nature*, vol. 455, no. 7210, pp. 204–207, 2008.

[15] U. Schneider, L. Hackermüller, S. Will, T. Best, I. Bloch, T. A. Costi, R. Helmes, D. Rasch, and A. Rosch, "Metallic and insulating phases of repulsively interacting fermions in a 3D optical lattice," *Science*, vol. 322, no. 5907, pp. 1520–1525, 2008.

[16] W. Ketterle and M. W. Zwierlein, "Making, probing and understanding ultracold Fermi gases," *Proceedings of the International School of Physics "Enrico Fermi"*, vol. 164, no. June 2006, pp. 95–287, 2007.

[17] D. S. Petrov, "Quantum mechanical stabilization of a collapsing Bose-Bose mixture," *Phys. Rev. Lett.*, vol. 115, p. 155302, Oct 2015.

[18] G. Semeghini, G. Ferioli, L. Masi, C. Mazzinghi, L. Wolswijk, F. Minardi, M. Modugno, G. Modugno, M. Inguscio, and M. Fattori, "Self-bound quantum droplets of atomic mixtures in free space," *Physical Review Letters*, vol. 120, no. 23, p. 235301, 2018.

[19] C. Cabrera, L. Tanzi, J. Sanz, B. Naylor, P. Thomas, P. Cheiney, and L. Tarruell, "Quantum liquid droplets in a mixture of Bose-Einstein condensates," *Science*, vol. 359, no. 6373, pp. 301–304, 2018.

[20] L. Tanzi, S. Roccuzzo, E. Lucioni, F. Famà, A. Fioretti, C. Gabbanini, G. Modugno, A. Recati, and S. Stringari, "Supersolid symmetry breaking from compressional oscillations in a dipolar quantum gas," *Nature*, vol. 574, no. 7778, pp. 382–385, 2019.

[21] G. Natale, R. van Bijnen, A. Patscheider, D. Petter, M. Mark, L. Chomaz, and F. Ferlaino, "Excitation spectrum of a trapped dipolar supersolid and its experimental evidence," *Physical Review Letters*, vol. 123, no. 5, p. 050402, 2019.

[22] F. Böttcher, J.-N. Schmidt, M. Wenzel, J. Hertkorn, M. Guo, T. Langen, and T. Pfau, "Transient supersolid properties in an array of dipolar quantum droplets," *Physical Review X*, vol. 9, no. 1, p. 011051, 2019.

[23] J. Léonard, A. Morales, P. Zupancic, T. Esslinger, and T. Donner, "Supersolid formation in a quantum gas breaking a continuous translational symmetry," *Nature*, vol. 543, no. 7643, p. 87, 2017.

[24] N. Goldman, J. C. Budich, and P. Zoller, "Topological quantum matter with ultracold gases in optical lattices," *Nature Physics*, vol. 12, no. 7, pp. 639–645, 2016.

[25] M. J. H. Ku, A. T. Sommer, L. W. Cheuk, and M. W. Zwierlein, "Revealing the superfluid lambda transition in the universal thermodynamics of a Unitary Fermi Gas," vol. 335, no. February, pp. 563–568, 2012.

[26] M. Inguscio, W. Ketterle, and C. Salomon, "Ultra-cold Fermi Gases: Proceedings of the International School of Physics "Enrico Fermi", Course CLXIV, Varenna, 20 to 30 June 2006," 2008.

[27] M. W. Zwierlein, J. R. Abo-Shaeer, A. Schirotzek, C. H. Schunck, and W. Ketterle, "Vortices and superfluidity in a strongly interacting Fermi gas," *Nature*, vol. 435, no. 7045, pp. 1047–1051, 2005.

[28] S. Gupta, Z. Hadzibabic, M. Zwierlein, C. Stan, K. Dieckmann, C. Schunck, E. Van Kempen, B. Verhaar, and W. Ketterle, "Radio-frequency spectroscopy of ultracold fermions," *Science*, vol. 300, no. 5626, pp. 1723–1726, 2003.

[29] A. Schirotzek, Y.-i. Shin, C. H. Schunck, and W. Ketterle, "Determination of the superfluid gap in atomic Fermi gases by quasiparticle spectroscopy," *Physical Review Letters*, vol. 101, no. 14, p. 140403, 2008.

[30] A. Behrle, T. Harrison, J. Kombe, K. Gao, M. Link, J.-S. Bernier, C. Kollath, and M. Köhl, "Higgs mode in a strongly interacting fermionic superfluid," *Nature Physics*, vol. 14, no. 8, pp. 781–785, 2018.

[31] S. Krinner, T. Esslinger, and J. P. Brantut, "Two-terminal transport measurements with cold atoms," *Journal of Physics Condensed Matter*, vol. 29, no. 34, 2017.

[32] N. Luick, L. Sobirey, M. Bohlen, V. P. Singh, L. Mathey, T. Lompe, and H. Moritz, "An ideal Josephson junction in an ultracold two-dimensional Fermi gas," *Science*, vol. 369, no. 6499, pp. 89–91, 2020.

[33] B. D. Josephson, "Possible new effects in superconductive tunnelling," *Phys. Lett.*, vol. 1, no. 7, pp. 251 – 253, 1962.

[34] F. Meier and W. Zwerger, "Josephson tunneling between weakly interacting Bose-Einstein condensates," *Physical Review A - Atomic, Molecular, and Optical Physics*, vol. 64, no. 3, p. 15, 2001.

[35] S. Uchino, "Role of Nambu-Goldstone modes in the fermionic-superfluid point contact," *Phys. Rev. Research*, vol. 2, p. 023340, Jun 2020.

[36] S. Uchino and J.-P. Brantut, "Bosonic superfluid transport in a quantum point contact," *Physical Review Research*, vol. 2, no. 2, 2020.

[37] C. J. Pethick and H. Smith, *Bose-Einstein condensation in dilute gases*. Cambridge university press, 2002.

[38] J. J. Sakurai, *Modern quantum mechanics.* Addison-Wesley Pub. Co, 1994.

[39] J. Dalibard, "Collisional dynamics of ultra-cold atomic gases," in *Proceedings of the International School of Physics-Enrico Fermi*, vol. 321, p. 14, 1999.

[40] G. Zürn, T. Lompe, A. N. Wenz, S. Jochim, P. Julienne, and J. Hutson, "Precise characterization of ^{6}Li Feshbach resonances using trap-sideband-resolved RF spectroscopy of weakly bound molecules," *Physical Review Letters*, vol. 110, no. 13, p. 135301, 2013.

[41] R. Haussmann, W. Rantner, S. Cerrito, and W. Zwerger, "Thermodynamics of the BCS-BEC crossover," *Physical Review A - Atomic, Molecular, and Optical Physics*, vol. 75, no. 2, pp. 1–22, 2007.

[42] D. Eagles, "Possible pairing without superconductivity at low carrier concentrations in bulk and thin-film superconducting semiconductors," *Physical Review*, vol. 186, no. 2, p. 456, 1969.

[43] A. J. Leggett, "Diatomic molecules and Cooper pairs," in *Modern trends in the theory of condensed matter*, pp. 13–27, Springer, 1980.

[44] P. Nozieres and S. Schmitt-Rink, "Bose condensation in an attractive fermion gas: From weak to strong coupling superconductivity," *Journal of Low Temperature Physics*, vol. 59, no. 3-4, pp. 195–211, 1985.

[45] E. J. Mueller, "Review of pseudogaps in strongly interacting Fermi gases," *Reports on Progress in Physics*, vol. 80, no. 10, p. 104401, 2017.

[46] D. Petrov, C. Salomon, and G. Shlyapnikov, "Scattering properties of weakly bound dimers of fermionic atoms," *Physical Review A*, vol. 71, no. 1, p. 012708, 2005.

[47] H. Heiselberg, "Fermi systems with long scattering lengths," *Physical Review A*, vol. 63, no. 4, p. 043606, 2001.

[48] T.-L. Ho, "Universal thermodynamics of degenerate quantum gases in the unitarity limit," *Physical Review Letters*, vol. 92, no. 9, p. 090402, 2004.

[49] M. Horikoshi, S. Nakajima, M. Ueda, and T. Mukaiyama, "Measurement of universal thermodynamic functions for a unitary Fermi gas," *Science*, vol. 327, no. 5964, pp. 442–445, 2010.

[50] S. Nascimbène, N. Navon, K. Jiang, F. Chevy, and C. Salomon, "Exploring the thermodynamics of a universal Fermi gas," *Nature*, vol. 463, no. 7284, pp. 1057–1060, 2010.

[51] N. Navon, S. Nascimbene, F. Chevy, and C. Salomon, "The equation of state of a low-temperature Fermi gas with tunable interactions," *Science*, vol. 328, no. 5979, pp. 729–732, 2010.

[52] E. Taylor, H. Hu, X.-J. Liu, L. Pitaevskii, A. Griffin, and S. Stringari, "First and second sound in a strongly interacting Fermi gas," *Phys. Rev. A*, vol. 80, no. 5, p. 053601, 2009.

[53] Y.-H. Hou, L. P. Pitaevskii, and S. Stringari, "First and second sound in a highly elongated Fermi gas at unitarity," *Phys. Rev. A*, vol. 88, no. 4, p. 043630, 2013.

[54] T.-L. Ho and E. J. Mueller, "High temperature expansion applied to fermions near Feshbach resonance," *Physical Review Letters*, vol. 92, no. 16, p. 160404, 2004.

[55] X.-J. Liu, H. Hu, and P. D. Drummond, "Virial expansion for a strongly correlated Fermi gas," *Physical Review Letters*, vol. 102, no. 16, p. 160401, 2009.

[56] L. D. Landau, E. M. Lifšic, E. M. Lifshitz, and L. Pitaevskii, *Statistical physics: theory of the condensed state*, vol. 9. Butterworth-Heinemann, 1980.

[57] O. Penrose and L. Onsager, "Bose-Einstein condensation and liquid helium," *Physical Review*, vol. 104, no. 3, p. 576, 1956.

[58] C. N. Yang, "Concept of off-diagonal long-range order and the quantum phases of liquid He and of superconductors," *Reviews of Modern Physics*, vol. 34, no. 4, p. 694, 1962.

[59] L. Salasnich, N. Manini, and A. Parola, "Condensate fraction of a Fermi gas in the BCS-BEC crossover," *Physical Review A*, vol. 72, no. 2, p. 023621, 2005.

[60] G. Astrakharchik, J. Boronat, J. Casulleras, and S. Giorgini, "Momentum distribution and condensate fraction of a fermion gas in the BCS-BEC crossover," *Physical Review Letters*, vol. 95, no. 23, p. 230405, 2005.

[61] R. He, N. Li, B. N. Lu, and D. Lee, "Superfluid condensate fraction and pairing wave function of the unitary Fermi gas," *Physical Review A*, vol. 101, no. 6, pp. 1–7, 2020.

[62] C. Regal, M. Greiner, and D. S. Jin, "Observation of resonance condensation of fermionic atom pairs," *Physical Review Letters*, vol. 92, no. 4, p. 040403, 2004.

[63] M. Zwierlein, C. Stan, C. Schunck, S. Raupach, A. Kerman, and W. Ketterle, "Condensation of pairs of fermionic atoms near a Feshbach resonance," *Physical Review Letters*, vol. 92, no. 12, p. 120403, 2004.

[64] M. Zwierlein, C. Schunck, C. Stan, S. Raupach, and W. Ketterle, "Formation dynamics of a fermion pair condensate," *Physical Review Letters*, vol. 94, no. 18, p. 180401, 2005.

[65] L. Landau, "Theory of the superfluidity of helium II," *Physical Review*, vol. 60, no. 4, p. 356, 1941.

[66] L. Salasnich, "Low-temperature thermodynamics of the unitary Fermi gas: Superfluid fraction, first sound, and second sound," *Physical Review A*, vol. 82, no. 6, p. 063619, 2010.

[67] R. Combescot, M. Y. Kagan, and S. Stringari, "Collective mode of homogeneous superfluid Fermi gases in the BEC-BCS crossover," *Physical Review A*, vol. 74, no. 4, p. 042717, 2006.

[68] D. E. Miller, J. K. Chin, C. A. Stan, Y. Liu, W. Setiawan, C. Sanner, and W. Ketterle, "Critical velocity for superfluid flow across the BEC-BCS crossover," *Physical Review Letters*, vol. 99, no. 7, pp. 1–4, 2007.

[69] W. Weimer, K. Morgener, V. P. Singh, J. Siegl, K. Hueck, N. Luick, L. Mathey, and H. Moritz, "Critical velocity in the BEC-BCS crossover," *Physical Review Letters*, vol. 114, no. 9, pp. 1–5, 2015.

[70] L. A. Sidorenkov, M. K. Tey, R. Grimm, Y.-H. Hou, L. Pitaevskii, and S. Stringari, "Second sound and the superfluid fraction in a Fermi gas with resonant interactions," *Nature*, vol. 498, no. 7452, pp. 78–81, 2013.

[71] M. B. Dahan, E. Peik, J. Reichel, Y. Castin, and C. Salomon, "Bloch oscillations of atoms in an optical potential," *Physical Review Letters*, vol. 76, no. 24, p. 4508, 1996.

[72] G. Roati, C. D'Errico, L. Fallani, M. Fattori, C. Fort, M. Zaccanti, G. Modugno, M. Modugno, and M. Inguscio, "Anderson localization of a non-interacting Bose-Einstein condensate," *Nature*, vol. 453, no. 7197, pp. 895–898, 2008.

[73] J. Billy, V. Josse, Z. Zuo, A. Bernard, B. Hambrecht, P. Lugan, D. Clément, L. Sanchez-palencia, P. Bouyer, and A. Aspect, "Direct observation of Anderson localization of matter waves in a controlled disorder," *Nature*, vol. 453, no. 7197, pp. 891–894, 2008.

[74] M. R. Matthews, B. P. Anderson, P. Haljan, D. Hall, C. Wieman, and E. A. Cornell, "Vortices in a Bose-Einstein condensate," *Physical Review Letters*, vol. 83, no. 13, p. 2498, 1999.

[75] J. Abo-Shaeer, C. Raman, J. Vogels, and W. Ketterle, "Observation of vortex lattices in Bose-Einstein condensates," *Science*, vol. 292, no. 5516, pp. 476–479, 2001.

[76] J.-P. Brantut, J. Meineke, D. Stadler, S. Krinner, and T. Esslinger, "Conduction of ultracold fermions through a mesoscopic channel," *Science*, vol. 337, no. 6098, pp. 1069–1071, 2012.

[77] J.-P. Brantut, C. Grenier, J. Meineke, D. Stadler, S. Krinner, C. Kollath, T. Esslinger, and A. Georges, "A thermoelectric heat engine with ultracold atoms," *Science*, vol. 342, no. 6159, pp. 713–715, 2013.

[78] S. Krinner, D. Stadler, D. Husmann, J.-P. Brantut, and T. Esslinger, "Observation of quantized conductance in neutral matter," *Nature*, vol. 517, no. 7532, pp. 64–67, 2015.

[79] M. Lebrat, S. Häusler, P. Fabritius, D. Husmann, L. Corman, and T. Esslinger, "Quantized conductance through a spin-selective atomic point contact," *Physical Review Letters*, vol. 123, no. 19, p. 193605, 2019.

[80] A. Barone and G. Paterno, *Physics and applications of the Josephson effect.* Wiley, 1982.

[81] K. Sukhatme, Y. Mukharsky, T. Chui, and D. Pearson, "Observation of the ideal Josephson effect in superfluid He," *Nature*, vol. 411, no. 6835, pp. 280–283, 2001.

[82] E. Hoskinson, Y. Sato, I. Hahn, and R. Packard, "Transition from phase slips to the Josephson effect in a superfluid ^{4}He weak link," *Nature Physics*, vol. 2, no. 1, pp. 23–26, 2006.

[83] J. Davis and R. Packard, "Superfluid ^{3}He Josephson weak links," *Reviews of Modern Physics*, vol. 74, no. 3, p. 741, 2002.

[84] F. Cataliotti, S. Burger, C. Fort, P. Maddaloni, F. Minardi, A. Trombettoni, A. Smerzi, and M. Inguscio, "Josephson junction arrays with Bose-Einstein condensates," *Science*, vol. 293, no. 5531, pp. 843–846, 2001.

[85] G. Valtolina, A. Burchianti, A. Amico, E. Neri, K. Xhani, J. A. Seman, A. Trombettoni, A. Smerzi, M. Zaccanti, M. Inguscio, and G. Roati, "Josephson effect in fermionic superfluids across the BEC-BCS crossover," *Science*, vol. 350, no. 6267, pp. 1505–1508, 2015.

[86] M. Abbarchi, A. Amo, V. Sala, D. Solnyshkov, H. Flayac, L. Ferrier, I. Sagnes, E. Galopin, A. Lemaître, G. Malpuech, *et al.*, "Macroscopic quantum self-trapping and Josephson oscillations of exciton polaritons," *Nature Physics*, vol. 9, no. 5, pp. 275–279, 2013.

[87] M. Tinkham, *Introduction to Superconductivity.* New York: McGraw-Hill, 2nd ed. ed., 1996.

[88] K. Likharev, "Superconducting weak links," *Reviews of Modern Physics*, vol. 51, no. 1, p. 101, 1979.

[89] V. Ambegaokar and A. Baratoff, "Tunneling between superconductors," *Phys. Rev. Lett.*, vol. 10, pp. 486–489, Jun 1963.

[90] J. Anderson and A. Goldman, "Thermal fluctuations and the Josephson supercurrent," *Physical Review Letters*, vol. 23, no. 3, p. 128, 1969.

[91] A. Smerzi, S. Fantoni, S. Giovanazzi, and S. R. Shenoy, “Quantum coherent atomic tunneling between two trapped Bose-Einstein condensates,” *Physical Review Letters*, vol. 79, no. 25, pp. 4950–4953, 1997.

[92] I. Zapata, F. Sols, and A. J. Leggett, “Josephson effect between trapped Bose-Einstein condensates,” *Physical Review A - Atomic, Molecular, and Optical Physics*, vol. 57, no. 1, pp. R28–R31, 1998.

[93] P. Zou and F. Dalfovo, “Josephson oscillations and self-trapping of superfluid fermions in a double-well potential,” *Journal of Low Temperature Physics*, vol. 177, no. 5-6, pp. 240–256, 2014.

[94] G. Milburn, J. Corney, E. M. Wright, and D. Walls, “Quantum dynamics of an atomic Bose-Einstein condensate in a double-well potential,” *Physical Review A*, vol. 55, no. 6, p. 4318, 1997.

[95] M. Albiez, R. Gati, J. Fölling, S. Hunsmann, M. Cristiani, and M. K. Oberthaler, “Direct observation of tunneling and nonlinear self-trapping in a single bosonic Josephson junction,” *Physical Review Letters*, vol. 95, no. 1, p. 010402, 2005.

[96] G. Spagnolli, G. Semeghini, L. Masi, G. Ferioli, A. Trenkwalder, S. Coop, M. Landini, L. Pezze, G. Modugno, M. Inguscio, *et al.*, “Crossing over from attractive to repulsive interactions in a tunneling bosonic josephson junction,” *Physical Review Letters*, vol. 118, no. 23, p. 230403, 2017.

[97] S. Giovanazzi, A. Smerzi, and S. Fantoni, “Josephson effects in dilute Bose-Einstein condensates,” *Physical Review Letters*, vol. 84, no. 20, pp. 4521–4524, 2000.

[98] S. Levy, E. Lahoud, I. Shomroni, and J. Steinhauer, “The a.c. and d.c. Josephson effects in a Bose-Einstein condensate,” *Nature*, vol. 449, no. 7162, pp. 579–583, 2007.

[99] A. Spuntarelli, P. Pieri, and G. Strinati, “Josephson effect throughout the BCS-BEC crossover,” *Physical Review Letters*, vol. 99, no. 4, p. 040401, 2007.

[100] A. Spuntarelli, P. Pieri, and G. C. Strinati, “Solution of the Bogoliubov-de Gennes equations at zero temperature throughout the BCS-BEC crossover: Josephson and related effects,” *Physics Reports*, vol. 488, no. 4-5, pp. 111–167, 2010.

[101] M. Zaccanti and W. Zwerger, “Critical Josephson current in BCS-BEC crossover superfluids,” jul 2019.

[102] P. W. Anderson, “Random-phase approximation in the theory of superconductivity,” *Physical Review*, vol. 112, no. 6, p. 1900, 1958.

[103] G. Valtolina, *Superfluid and spin dynamics of strongly interacting atomic Fermi gases*. PhD thesis, Scuola Normale Superiore di Pisa, 2016.

[104] A. Amico, *Probing the many body dynamics of ultracold repulsive Fermi gases of Lithium atoms.* PhD thesis, Università degli Studi di Firenze, 2018.

[105] R. Grimm, M. Weidemüller, and Y. B. Ovchinnikov, "Optical dipole traps for neutral atoms," *Advances in atomic, molecular, and optical physics*, vol. 42, pp. 95–170, 2000.

[106] H. J. Metcalf and P. van der Straten, *Laser Cooling and Trapping.* Springer Science & Business Media, 2012.

[107] M. Inguscio and L. Fallani, *Atomic physics: precise measurements and ultracold matter.* OUP Oxford, 2013.

[108] C. Cohen-Tannoudji and D. Guéry-Odelin, *Advances in atomic physics: an overview.* World Scientific, 2011.

[109] A. Burchianti, G. Valtolina, J. Seman, E. Pace, M. De Pas, M. Inguscio, M. Zaccanti, and G. Roati, "Efficient all-optical production of large ^{6}Li quantum gases using D1 gray-molasses cooling," *Physical Review A*, vol. 90, no. 4, p. 043408, 2014.

[110] M. Cetina, M. Jag, R. S. Lous, I. Fritsche, J. T. Walraven, R. Grimm, J. Levinsen, M. M. Parish, R. Schmidt, M. Knap, *et al.*, "Ultrafast many-body interferometry of impurities coupled to a fermi sea," *Science*, vol. 354, no. 6308, pp. 96–99, 2016.

[111] A. Amico, F. Scazza, G. Valtolina, P. Tavares, W. Ketterle, M. Inguscio, G. Roati, and M. Zaccanti, "Time-resolved observation of competing attractive and repulsive short-range correlations in strongly interacting Fermi gases," *Physical Review Letters*, vol. 121, no. 25, p. 253602, 2018.

[112] F. Scazza, G. Valtolina, A. Amico, P. Tavares, M. Inguscio, W. Ketterle, G. Roati, and M. Zaccanti, "Exploring emergent heterogeneous phases in strongly repulsive Fermi gases," *Physical Review A*, vol. 101, no. 1, p. 013603, 2020.

[113] F. Scazza, G. Valtolina, P. Massignan, A. Recati, A. Amico, A. Burchianti, C. Fort, M. Inguscio, M. Zaccanti, and G. Roati, "Repulsive Fermi polarons in a resonant mixture of ultracold ^{6}Li atoms," *Physical Review Letters*, vol. 118, no. 8, p. 083602, 2017.

[114] P. Massignan, M. Zaccanti, and G. M. Bruun, "Polarons, dressed molecules and itinerant ferromagnetism in ultracold Fermi gases," *Reports on Progress in Physics*, vol. 77, no. 3, p. 034401, 2014.

[115] B. H. Bransden, C. J. Joachain, and T. J. Plivier, *Physics of atoms and molecules.* Pearson education, 2003.

[116] J. Goodman, *Introduction to Fourier Optics.* McGraw-Hill physical and quantum electronics series, W. H. Freeman, 2005.

[117] B. M. and W. E., *Principle of Optics.* Cambridge University Press, 1999.

[118] K. Hueck, N. Luick, L. Sobirey, J. Siegl, T. Lompe, H. Moritz, L. W. Clark, and C. Chin, "Calibrating high intensity absorption imaging of ultracold atoms," *Optics Express*, vol. 25, no. 8, p. 8670, 2017.

[119] C. J. Foot, *Atomic physics*, vol. 7. Oxford University Press, 2005.

[120] S. M. Popoff, "wavefronthsaping/alp4lib: First release," Feb 2017.

[121] G. Del Pace, "Tailored optical potentials for experiments with atomic superfluids," Master's thesis, Università degli studi di Firenze, 2017.

[122] E. Perego, "Generation of arbitrary optical potentials for atomic physics experiments using a digital micromirror device," Master's thesis, Università degli studi di Firenze, 2015.

[123] K. Hueck, N. Luick, L. Sobirey, J. Siegl, T. Lompe, and H. Moritz, "Two-dimensional homogeneous Fermi gases," *Physical Review Letters*, vol. 120, no. 6, p. 60402, 2018.

[124] M. Naraschewski and D. M. Stamper-Kurn, "Analytical description of a trapped semi-ideal Bose gas at finite temperature," *Physical Review A - Atomic, Molecular, and Optical Physics*, vol. 58, no. 3, pp. 2423–2426, 1998.

[125] L. Dobrek, M. Gajda, M. Lewenstein, K. Sengstock, G. Birkl, W. Ertmer, *et al.*, "Optical generation of vortices in trapped Bose-Einstein condensates," *Physical Review A*, vol. 60, no. 5, p. R3381, 1999.

[126] A. Burchianti, F. Scazza, A. Amico, G. Valtolina, J. Seman, C. Fort, M. Zaccanti, M. Inguscio, and G. Roati, "Connecting dissipation and phase slips in a Josephson junction between fermionic superfluids," *Physical Review Letters*, vol. 120, no. 2, p. 025302, 2018.

[127] K. Xhani, E. Neri, L. Galantucci, F. Scazza, A. Burchianti, K.-L. Lee, C. Barenghi, A. Trombettoni, M. Inguscio, M. Zaccanti, *et al.*, "Critical transport and vortex dynamics in a thin atomic Josephson junction," *Physical Review Letters*, vol. 124, no. 4, p. 045301, 2020.

[128] F. Piazza, L. Collins, and A. Smerzi, "Current-phase relation of a Bose-Einstein condensate flowing through a weak link," *Physical Review A*, vol. 81, no. 3, p. 033613, 2010.

[129] H. Heiselberg, "Collective modes of trapped gases at the BEC-BCS crossover," *Physical Review Letters*, vol. 93, no. 4, p. 040402, 2004.

[130] W. Wen, S.-Q. Shen, and G. Huang, "Propagation of sound and supersonic bright solitons in superfluid Fermi gases in BCS-BEC crossover," *Physical Review B*, vol. 81, no. 1, p. 014528, 2010.

[131] D. Ter Haar, *Problems in quantum mechanics.* Courier Corporation, 2014.

[132] F. M. Fernández, "Wronskian method for one-dimensional quantum scattering," *American Journal of Physics*, vol. 79, no. 8, pp. 877–881, 2011.

[133] E. Goldobin, D. Koelle, R. Kleiner, and A. Buzdin, "Josephson junctions with second harmonic in the current-phase relation: Properties of φ junctions," *Physical Review B*, vol. 76, no. 22, p. 224523, 2007.

[134] M. Pini, P. Pieri, M. Jäger, J. H. Denschlag, and G. C. Strinati, "Pair correlations in the normal phase of an attractive Fermi gas," *New Journal of Physics*, vol. 22, no. 8, p. 083008, 2020.

[135] R. Haussmann and W. Zwerger, "Thermodynamics of a trapped unitary Fermi gas," *Physical Review A*, vol. 78, no. 6, p. 063602, 2008.

[136] T. Savard, K. O'hara, and J. Thomas, "Laser-noise-induced heating in far-off resonance optical traps," *Physical Review A*, vol. 56, no. 2, p. R1095, 1997.

[137] M. E. Gehm, K. M. O'Hara, T. A. Savard, and J. E. Thomas, "Dynamics of noise-induced heating in atom traps," *Physical Review A*, vol. 58, no. 5, pp. 6742–6749, 1998.

[138] E. R. S. Guajardo, M. K. Tey, L. A. Sidorenkov, and R. Grimm, "Higher-nodal collective modes in a resonantly interacting Fermi gas," *Physical Review A*, vol. 87, no. 6, p. 063601, 2013.

[139] D. Husmann, S. Uchino, S. Krinner, M. Lebrat, T. Giamarchi, T. Esslinger, and J.-P. Brantut, "Connecting strongly correlated superfluids by a quantum point contact," *Science*, vol. 350, no. 6267, pp. 1498–1501, 2015.

[140] J. Thomas, J. Kinast, and A. Turlapov, "Virial theorem and universality in a unitary Fermi gas," *Physical Review Letters*, vol. 95, no. 12, p. 120402, 2005.

[141] L. Luo, *Entropy and Superfluid Critical Parameters of a Strongly Interacting Fermi Gas.* PhD thesis, Duke University, 2008.

[142] B. I. Halperin, G. Refael, and E. Demler, "Resistance in superconductors," in *Bcs: 50 Years*, pp. 185–226, World Scientific, 2011.

[143] E. W. Hansen and P.-L. Law, "Recursive methods for computing the Abel transform and its inverse," *JOSA A*, vol. 2, no. 4, pp. 510–520, 1985.

[144] C. B. Duke, *Theory of Metal-Barrier-Metal Tunneling*, pp. 31–46. Springer, Boston MA, 1969.

[145] C. Kuhn, S. Hoinka, I. Herrera, P. Dyke, J. Kinnunen, G. Bruun, and C. Vale, "High-frequency sound in a unitary Fermi gas," *Physical Review Letters*, vol. 124, no. 15, p. 150401, 2020.

[146] P. B. Patel, Z. Yan, B. Mukherjee, R. J. Fletcher, J. Struck, and M. W. Zwierlein, "Universal sound diffusion in a strongly interacting Fermi gas," *arXiv preprint arXiv:1909.02555*, 2019.

[147] C. H. Williamson, "Vortex dynamics in the cylinder wake," *Annual review of fluid mechanics*, vol. 28, no. 1, pp. 477–539, 1996.

[148] S. Inouye, S. Gupta, T. Rosenband, A. Chikkatur, A. Görlitz, T. Gustavson, A. Leanhardt, D. Pritchard, and W. Ketterle, "Observation of vortex phase singularities in Bose-Einstein condensates," *Physical Review Letters*, vol. 87, no. 8, p. 080402, 2001.

[149] T. Neely, E. Samson, A. Bradley, M. Davis, and B. P. Anderson, "Observation of vortex dipoles in an oblate Bose-Einstein condensate," *Physical Review Letters*, vol. 104, no. 16, p. 160401, 2010.

[150] J. W. Park, B. Ko, and Y.-i. Shin, "Critical vortex shedding in a strongly interacting fermionic superfluid," *Physical Review Letters*, vol. 121, no. 22, p. 225301, 2018.

[151] M. Reeves, T. Billam, B. P. Anderson, and A. Bradley, "Identifying a superfluid Reynolds number via dynamical similarity," *Physical Review Letters*, vol. 114, no. 15, p. 155302, 2015.

[152] W. J. Kwon, J. H. Kim, S. W. Seo, and Y. Shin, "Observation of von Kármán vortex street in an atomic superfluid gas," *Physical Review Letters*, vol. 117, no. 24, pp. 1–5, 2016.

[153] B. Jackson, N. Proukakis, C. Barenghi, and E. Zaremba, "Finite-temperature vortex dynamics in Bose-Einstein condensates," *Physical Review A*, vol. 79, no. 5, p. 053615, 2009.

[154] S. Rooney, P. Blakie, B. Anderson, and A. Bradley, "Suppression of Kelvon-induced decay of quantized vortices in oblate Bose-Einstein condensates," *Physical Review A*, vol. 84, no. 2, p. 023637, 2011.

[155] A. L. Gaunt, T. F. Schmidutz, I. Gotlibovych, R. P. Smith, and Z. Hadzibabic, "Bose-Einstein condensation of atoms in a uniform potential," *Physical Review Letters*, vol. 110, no. 20, pp. 1–5, 2013.

[156] B. Mukherjee, Z. Yan, P. B. Patel, Z. Hadzibabic, T. Yefsah, J. Struck, and M. W. Zwierlein, "Homogeneous atomic Fermi gases," *Physical Review Letters*, vol. 118, no. 12, pp. 1–5, 2017.

[157] J. Ville, T. Bienaimé, R. Saint-Jalm, L. Corman, M. Aidelsburger, L. Chomaz, K. Kleinlein, D. Perconte, S. Nascimbène, J. Dalibard, *et al.*, "Loading and compression of a single two-dimensional Bose gas in an optical accordion," *Physical Review A*, vol. 95, no. 1, p. 013632, 2017.

[158] R. Panza, "Manipulating ultracold atomic fermi gases with tailored optical potentials," Master's thesis, Università degli studi di Milano, 2018.

[159] R. J. Fletcher, A. Shaffer, C. C. Wilson, P. B. Patel, Z. Yan, V. Crépel, B. Mukherjee, and M. W. Zwierlein, "Geometric squeezing into the lowest Landau level," *arXiv preprint arXiv:1911.12347*, 2019.

[160] W. J. Kwon, G. Moon, S. W. Seo, and Y.-i. Shin, "Critical velocity for vortex shedding in a Bose-Einstein condensate," *Physical Review A*, vol. 91, no. 5, p. 053615, 2015.

[161] F. Pinsker and N. G. Berloff, "Transitions and excitations in a superfluid stream passing small impurities," *Physical Review A*, vol. 89, no. 5, p. 053605, 2014.

[162] G. Stagg, A. Allen, C. Barenghi, and N. Parker, "Classical-like wakes past elliptical obstacles in atomic Bose-Einstein condensates," in *Journal of Physics: Conference Series*, vol. 594, p. 012044, Newcastle University, 2015.

[163] D. J. Van Harlingen, "Phase-sensitive tests of the symmetry of the pairing state in the high-temperature superconductors—evidence for $d_{x^2-y^2}$ symmetry," *Reviews of Modern Physics*, vol. 67, no. 2, p. 515, 1995.

[164] C. Tsuei and J. Kirtley, "Pairing symmetry in cuprate superconductors," *Reviews of Modern Physics*, vol. 72, no. 4, p. 969, 2000.

[165] Y. Sekino, H. Tajima, and S. Uchino, "Mesoscopic spin transport between strongly interacting Fermi gases," *Physical Review Research*, vol. 2, no. 2, p. 023152, 2020.

[166] G. Bertaina and S. Giorgini, "BCS-BEC crossover in a two-dimensional Fermi gas," *Physical Review Letters*, vol. 106, no. 11, p. 110403, 2011.

[167] M. Ries, A. Wenz, G. Zürn, L. Bayha, I. Boettcher, D. Kedar, P. Murthy, M. Neidig, T. Lompe, and S. Jochim, "Observation of pair condensation in the quasi-2D BEC-BCS crossover," *Physical Review Letters*, vol. 114, no. 23, p. 230401, 2015.

[168] K. Fenech, P. Dyke, T. Peppler, M. Lingham, S. Hoinka, H. Hu, and C. Vale, "Thermodynamics of an attractive 2D Fermi gas," *Physical Review Letters*, vol. 116, no. 4, p. 045302, 2016.

[169] L. Sobirey, N. Luick, M. Bohlen, H. Biss, H. Moritz, and T. Lompe, "Observation of superfluidity in a strongly correlated two-dimensional Fermi gas," *arXiv preprint arXiv:2005.07607*, 2020.

[170] V. Berezinskii, "Destruction of long-range order in one-dimensional and two-dimensional systems having a continuous symmetry group I. Classical systems," *Sov. Phys. JETP*, vol. 32, no. 3, pp. 493–500, 1971.

[171] J. M. Kosterlitz and D. J. Thouless, “Ordering, metastability and phase transitions in two-dimensional systems,” *Journal of Physics C: Solid State Physics*, vol. 6, no. 7, p. 1181, 1973.

[172] B. Keimer, S. A. Kivelson, M. R. Norman, S. Uchida, and J. Zaanen, “From quantum matter to high-temperature superconductivity in copper oxides,” *Nature*, vol. 518, no. 7538, pp. 179–186, 2015.

[173] W. Morong and B. DeMarco, “Simulation of Anderson localization in two-dimensional ultracold gases for pointlike disorder,” *Physical Review A*, vol. 92, no. 2, p. 023625, 2015.

[174] J.-y. Choi, S. Hild, J. Zeiher, P. Schauß, A. Rubio-Abadal, T. Yefsah, V. Khemani, D. A. Huse, I. Bloch, and C. Gross, “Exploring the many-body localization transition in two dimensions,” *Science*, vol. 352, no. 6293, pp. 1547–1552, 2016.

[175] Y. Liu and A. Goldman, “Superconductor-insulator transitions in two dimensions,” *Modern Physics Letters B*, vol. 8, no. 05, pp. 277–300, 1994.